



McGill
UNIVERSITY

**Sensitive, Quantitative ELISA Enabled by a 3D-Printed
Microfluidic Chain Reaction Capillaric Circuit**

Author: Azim Parandakh

Supervisor: David Juncker

Biological and Biomedical Engineering Program

Department of Biomedical Engineering

McGill University, Montreal, Quebec, Canada

A thesis submitted in fulfillment of the requirements for the degree of Master of
Engineering

©Azim Parandakh

August 2022

Table of the contents

1. ABSTRACT	1
1.1. English version	1
1.2. French version.....	2
2. ACKNOWLEDGEMENTS	4
3. CONTRIBUTION OF AUTHORS	5
4. INTRODUCTION	6
4.1. Motivation.....	6
4.2. Project aims	8
4.3. Declaration of novelty.....	8
5. COMPREHENSIVE REVIEW OF RELEVANT LITERATURE	9
5.1. Capillary flow in microchannels and capillarie circuits	9
5.1.1. Introduction	9
5.1.2. The 3 waves of developments in capillary microfluidics	11
5.1.2.1. 1 st wave: mechanical micromachining and lamination.....	12
5.1.2.2. 2 nd wave: Cleanroom fabrication	13
5.1.2.3. 3 rd wave: Rapid prototyping.....	14
5.1.3. Fundamental parameters and equations	14
5.1.3.1. Wettability and contact angle.....	14
5.1.3.2. Capillary pressure.....	15
5.1.3.3. Flow rate and flow resistance	16
5.1.4. Foundations of capillarie circuits	17
5.1.5. Materials and surface chemistry.....	18
5.1.6. Capillarie elements.....	19
5.1.6.1. Vent.....	19
5.1.6.2. Inlet	20
5.1.6.3. Reservoir	21
5.1.6.4. Reaction chamber	21
5.1.6.5. Flow resistor.....	22
5.1.6.6. Capillary pump	23
5.1.6.7. Filling front guides.....	25
5.1.6.8. Capillary trigger valve.....	29
5.1.6.9. Temperature-controlled valves.....	30
5.1.6.10. Capillary soft valves.....	31
5.1.6.11. Capillary retention valves.....	32

5.1.6.12.	Retention burst valves	33
5.1.6.13.	Capillary domino valves	34
5.1.6.14.	Delay valves.....	35
5.1.6.15.	Transistor valve	36
5.1.7.	Capillarc circuits for sequential delivery	37
5.1.7.1.	Sequential delivery via retention valves	37
5.1.7.2.	Sequential delivery via trigger valves and retention burst valves	38
5.1.7.3.	Sequential delivery via conditional vents and capillary valves	39
5.1.7.4.	Sequential delivery via delay valves.....	40
5.1.7.5.	Sequential delivery via capillary domino valves	41
5.1.8.	Applications of capillarc circuits.....	42
5.1.8.1.	Immunoassays.....	42
5.1.8.2.	Capillarc circuits for DNA analysis.....	50
5.1.9.	Capillarc circuits for monitoring medical adherence.....	54
5.1.10.	Capillary-assisted microfluidic devices	55
5.1.11.	Rapid prototyping of capillarc circuits	57
5.1.11.1.	Xurography (razor writing).....	57
5.1.11.2.	Laser cutting.....	58
5.1.11.3.	3D printing	58
5.1.12.	Conclusions and future outlook.....	60
5.2.	SARS-CoV-2 and COVID-19 diagnostics.....	61
5.2.1.	Introduction	61
5.2.2.	COVID-19 etiology.....	61
5.2.3.	Nucleic acid amplification tests	62
5.2.3.1.	COVID-19 RT-PCR test	62
5.2.3.2.	Digital PCR-based SARS-CoV-2 detection.....	64
5.2.3.3.	COVID-19 NAATs based on isothermal amplification	65
5.2.3.3.1.	Loop-mediated isothermal amplification.....	65
5.2.3.3.2.	Nicking endonuclease amplification reaction.....	66
5.2.4.	CRISPR-based detection.....	69
5.2.5.	Immunoassays.....	70
5.2.6.	Fundamentals of immunoassays: Diffusion, convection, and reaction in surface-based biosensors	71
5.2.7.	ELISA: Development, optimization, and assay performance	73
5.2.7.1.	Sandwich ELISA protocol.....	75

5.2.7.2.	Plates.....	76
5.2.7.3.	Antibody Affinity.....	78
5.2.7.4.	Antibody clonality.....	78
5.2.7.5.	Reagent concentration.....	79
5.2.7.6.	Signal development.....	79
5.2.7.7.	Assay performance and the calibration curve.....	80
5.2.8.	COVID-19 immunoassays.....	83
5.2.8.1.	Serologic tests.....	83
5.2.8.2.	Virus neutralization test.....	86
5.2.8.3.	Antigen detection assay.....	88
5.2.9.	Different sample specimens for COVID-19 diagnosis.....	92
5.2.10.	Conclusions and future outlook.....	96
6.	BODY OF THE THESIS (METHODOLOGY AND RESEARCH FINDINGS)	97
6.1.	Quantitative, sensitive ELISA enabled by a 3D-printed microfluidic chain reaction capillaric circuit....	97
6.1.1.	Abstract.....	97
6.1.2.	Introduction.....	99
6.1.3.	Results and discussion.....	103
6.1.3.1.	ELISA chip fabrication and preparation.....	103
6.1.3.2.	ELISA chip design, operational mechanism, and workflow.....	103
6.1.3.2.1.	ELISA chip workflow: Aliquoting session.....	106
6.1.3.2.2.	ELISA chip workflow: Metering session.....	109
6.1.3.2.3.	ELISA chip workflow: Sequential delivery session.....	114
6.1.3.3.	COVID-19 antigen assay.....	116
6.1.4.	Conclusions and future works.....	119
6.1.5.	Experimental.....	121
6.1.5.1.	ELISA chip fabrication and preparation.....	121
6.1.5.2.	COVID-19 antigen assay.....	122
6.1.5.3.	Nitrocellulose membrane image analysis and LOD calculation.....	123
6.1.5.4.	ELISA chip video recording and image capturing.....	124
6.1.6.	Acknowledgments.....	124
6.1.7.	Supplementary figures.....	125
7.	COMPREHENSIVE SCHOLARLY DISCUSSION OF ALL THE FINDINGS	126
8.	FINAL CONCLUSION AND SUMMARY	130
9.	REFERENCES	131

1. ABSTRACT

1.1. English version

Sandwich immunoassays such as enzyme-linked immunosorbent assay (ELISA) have been miniaturized and performed in a lab-on-a-chip format, but either depend on a computer or complex peripherals to implement the multiple assays steps of conventional ELISA, or operate on simplified protocols without rinsing and with reduced performance as in the case of paper microfluidics and lateral flow assays. With the recent introduction of microfluidic chain reaction (MCR), complex fluidic operations can be structurally programmed in 3D printed capillarie circuits powered by capillary action. Here, we introduce the ELISA chip to pre-program the typical steps of an ELISA and execute them via an MCR. The ELISA chip was optimized and used for the quantification of the SARS-CoV-2 nucleocapsid protein in 4X-diluted saliva without the need for precise pipetting. Sample, reagents, and buffer were loaded into distinct inlets of the ELISA chip using disposable pipettes. Next, the ELISA chip generated 4 buffer aliquots (40, 60, 40, and 30 μL , respectively), and precisely metered the volumes of the sample (210 μL), detection antibody (70 μL), enzyme conjugate (50 μL), and substrate (80 μL), all stored in reservoirs. The user then click-connects a nitrocellulose strip integrated into a capillary-pump module to the reagent module, and the timed flow of the 8 solutions was executed step-by-step according to the progression of the MCR. A colored precipitate forming a line on a nitrocellulose strip served as an assay readout, and upon digitization, produced a calibration curve with a limit of detection of 54 and 91 pg/mL for buffer and diluted saliva, respectively. The ELISA chip is 3D-printed, modular, adaptable to

other targets and assays, and could be used in the lab to automate ELISA, or at the point of care for diagnostic tests with both the performance of central laboratory ELISA and the convenience and form factor of rapid tests.

Keywords: ELISA; immunoassays; microfluidic chain reaction; capillarity circuits; capillary flow

1.2. French version

Les immuno-essais sandwichs tels que l'essai immuno-enzymatique (ELISA) ont été miniaturisés et réalisés dans un format de laboratoire sur puce, mais soit ils dépendent d'un ordinateur ou de périphériques complexes pour mettre en œuvre les multiples étapes de l'ELISA conventionnel, soit ils fonctionnent selon des protocoles simplifiés sans rinçage et avec des performances réduites comme dans le cas de la microfluidique papier et des essais à flux latéral. Avec l'introduction récente de la réaction en chaîne microfluidique (MCR), des opérations fluidiques complexes peuvent être programmées structurellement dans des circuits capillaires imprimés en 3D et alimentés par l'action capillaire. Ici, nous introduisons la puce ELISA pour préprogrammer les étapes typiques d'un ELISA et les exécuter via une MCR. La puce ELISA a été optimisée et utilisée pour la quantification de la protéine de la nucléocapside du SRAS-CoV-2 dans de la salive diluée 4X sans avoir besoin d'un pipetage précis. L'échantillon, les réactifs et le tampon ont été chargés dans des entrées distinctes de la puce ELISA à l'aide de pipettes jetables. Ensuite, la puce ELISA a généré 4 aliquotes de tampon (40, 60, 40 et 30 μL , respectivement) et a dosé avec précision les volumes de l'échantillon (210 μL), de l'anticorps de détection (70 μL), du conjugué enzymatique (50 μL) et du substrat (80 μL), tous stockés dans des réservoirs. L'utilisateur connecte ensuite par clic une bande de nitrocellulose intégrée dans un module de pompe capillaire au module de

réactif, et le flux minuté des 8 solutions a été exécuté pas à pas selon la progression du MCR. Un précipité coloré formant une ligne sur une bande de nitrocellulose a servi de lecture du test et, après numérisation, a produit une courbe d'étalonnage avec une limite de détection de 54 et 91 pg/mL pour le tampon et la salive diluée, respectivement. La puce ELISA est imprimée en 3D, modulaire, adaptable à d'autres cibles et dosages, et pourrait être utilisée en laboratoire pour automatiser l'ELISA, ou sur le lieu de soins pour des tests de diagnostic offrant à la fois les performances de l'ELISA de laboratoire central et la commodité et le facteur de forme des tests rapides.

Mots-clés : ELISA ; immunoessais ; réaction en chaîne microfluidique ; circuits capillaires ; flux capillaire

2. ACKNOWLEDGEMENTS

I would like to thank everyone who has contributed to this thesis. Particularly, I would like to thank my supervisor, Prof. David Juncker, for giving me the opportunity of joining his group, for supporting me financially for 3 years, and more importantly for believing in me and helping me with my adventurous scientific journey.

Next, I would like to thank my dear colleagues Will Jorgia and Johan Renault, and Geunyoung Kim for helping me with the biological aspect of my project.

I would like to thank our previous postdoctoral fellows, Oriol Yembren and Mohamed Yafia, for training me in the design and fabrication of microfluidic chips.

I would like to thank Molly Shen and Rosalie Martel for training me in working with inkjet spotter equipment.

I would like to thank our research associate Andy NG for his thoughtful comments and constructive feedback during the whole project.

I would like to thank the Department of Biomedical Engineering for the generous financial support in the form of the BBME/BME Excellence Award.

3. CONTRIBUTION OF AUTHORS

The presented thesis was written by Azim Parandakh with revision help from Prof. David Juncker. The French version of the thesis abstract was edited by Felix Lussier. The manuscript was written by Azim Parandakh with revision help from Prof. Juncker and Dr. Andy Ng. The experiments for optimization of the COVID-19 antigen test and obtaining on-chip standard curves were carried out by Azim Parandakh with the help of Will Gogia, Johan Renault, and Geunyoung Kim. Azim Parandakh developed the microfluidic chip for the COVID-19 antigen test. Data analysis and figure preparation were performed by Azim Parandakh.

4. INTRODUCTION

4.1. Motivation

Polymerase chain reaction (PCR) is the gold standard method for the detection of severe acute respiratory coronavirus 2 (SARS-CoV-2). PCR offers excellent sensitivity, but high turnaround time, dependence on the instrumentation, such as a heater, and the need for trained healthcare professionals limit the application of PCR for point-of-care (POC) testing. ELISA is a well-established immunological assay to detect the presence of an analyte of interest in biological samples. Laboratory ELISA benefits from enzymatic amplification and achieves high sensitivity. However, laboratory ELISA requires instrumentation and is a lengthy process with several manual user interventions such as timed addition and removal of reagents and manual rinsing steps¹. These limitations make ELISA an inappropriate choice for resource-limited settings. Lateral flow assays (LFAs) have been developed to address some of the limitations of ELISA. LFAs are simple and fast with minimal user intervention as they are typically carried out in one step, i.e. sample loading. However, LFAs are typically qualitative or semiquantitative with limited sensitivity compared to sophisticated laboratory-based assays, cannot implement enzymatic amplification or rinsing steps, and signal readout needs to be performed within a short time frame (~15-30 min)^{2,3}, thereby limiting their use for many modern clinical applications. To address the abovementioned limitations, there is a need for a device capable of automating ELISA manual steps, reducing its total operational time, and making it compatible with minimal laboratory equipment without compromising sensitivity.

Saliva samples are a potential sample source for COVID-19 diagnostics. Saliva sampling is patient-friendly and can be done by the patient to minimize the contact between the patient and the healthcare professional. Furthermore, saliva can be an appropriate sample source for patients who have limitations in utilizing nasopharyngeal swabs (the primary sample specimen for COVID-19 diagnostics) or nasal swabs such as toddlers, babies, and young children⁴⁻⁹. However, a COVID-19 test working with saliva requires high sensitivity to yield reliable results¹⁰. The majority of the commercially available antigen tests in the market use nasal or oral swab sample specimens, and the number of saliva-based antigen tests is limited. As an example, a saliva-based rapid antigen test was developed by Sona Nanotech Inc. for the detection of the spike protein of SARS-CoV-2 within 20 min. However, the developed kit offers only qualitative results which are dependent on the user interpretation and prone to occasional failure. Quantitative saliva-based antigen tests also exist such as the Lumipulse® G SARS-CoV-2 Ag. Lumipulse® G SARS-CoV-2 Ag works based on the chemiluminescent immunoassay and can detect nucleocapsid protein of SARS-CoV-2 with high sensitivity (98.5% concordance with reverse transcriptase PCR)¹¹. However, the signal readout should be performed via a special instrument in a short time frame after the test due to the temporary nature of the chemiluminescent signal, and such requirements may be difficult to be satisfied in resource- and staff-limited settings. To this end, there is a need for saliva-based COVID-19 diagnostic tests that can generate a permanent signal quantifiable with common and accessible instruments, e.g. cell phone or scanner, while having high sensitivity.

4.2. Project aims

The aims of the presented work are as follows:

Aim #1: Developing a capillary-driven microfluidic chip for automating liquid handling tasks required for laboratory ELISA mainly including aliquoting, metering, and sequential delivery

Aim #2: Optimizing an off-chip COVID-19 antigen test for nucleocapsid protein of SARS-CoV-2 spiked in buffer and human saliva

Aim #3: Implementing the COVID-19 assay developed in Aim #2 into the capillary driven-microfluidic chip developed in Aim #1 to obtain an on-chip standard curve

4.3. Declaration of novelty

The most recent capillary-driven microfluidic chip that enabled full implementation of liquid handling tasks required for laboratory ELISA, including reagents addition, incubation, and removal as well as intermediate washing steps, has been developed by Yafia et al¹². However, the chip required the addition of precise volumes of reagent and samples via a laboratory micropipette, which although possible, requires a trained user and detailed attention, and is prone to occasional failure. In addition, the chip was only able to work with a solution containing a maximum Tween20 concentration of 0.0125%. Tween20 is an essential constituent of the ELISA wash buffer that assists in reducing unspecific binding and background noise¹³. But, this level of Tween20 concentration is far below the one that is used in ELISA kits (i.e., 0.05%)¹³. Our capillary-driven microfluidic chip is equipped with aliquoting and metering features which obviate the need for precise addition of samples, reagents, and washing buffer and make the chip compatible with disposable pipettes. Furthermore, it can

operate under high surface tension solutions, i.e., Tween20 concentration of 0.05%, without any fluidic malfunctions.

Regarding the COVID-19 diagnostics, the commercially-available saliva-based antigen tests to date provide either qualitative results or in the case of quantitative results, need a special instrument for signal readout at a limited time frame after the test¹¹. Our saliva-based COVID-19 antigen assay offers a novel tool due to the following reasons: (i) It generates a colorimetric signal which can be either interpreted by the naked eye as an immediate readout or captured by a regular scanner to be quantified; (ii) the colorimetric signal is time-insensitive which obviates the need for signal readout at a specific time-frame and also provides the possibility of results archival; and (iii) it works with a small dilution factor (i.e., 4) of human saliva and can detect nucleocapsid protein of SARS-CoV with high sensitivity (i.e., 94 pg/mL).

5. COMPREHENSIVE REVIEW OF RELEVANT LITERATURE

5.1. Capillary flow in microchannels and capillary circuits

5.1.1. Introduction

Microfluidic devices are miniaturized liquid handling systems with the potential to be employed for biomedical applications due to ease of automation, small sample and reagent volume, efficient mass transport to the functionalized surfaces, cost-efficiency, and disposability¹⁴. Although microfluidic devices are small, their operation often needs peripheral equipment and lab facilities, which instead of standing as “lab-on-a-chip” devices, mostly resemble the notion of “lab-around-a-chip” devices, thereby limiting their applications at the point-of-need¹⁵. Capillary-driven microfluidic devices leverage from capillary effect to

power liquid flow. Capillary effects stem from the interplay between the liquid surface tension with the geometry and surface chemistry of the channel wherein the liquid is flowing¹⁶. They are called passive as they do not provide real-time control of the flow as opposed to active microfluidic devices that have external peripheral equipment for flow control. The terms such as self-powered, autonomous, integrated, and advanced have been associated with capillary microfluidics to reflect their capacity to operate with minimal (or no) instrumentation and to be used at the point-of-care settings¹⁷.

Capillary forces can be employed in various approaches to regulating flow in a microfluidic system. One of the simplest forms in this regard can be the positive pressure generated by droplets introduced at the inlets and outlets to regulate flow^{18,19}. Capillary forces are inevitable at small scales and can significantly affect flow even in the presence of other active flow-inducing devices^{16,20}. The capillary phenomenon can be combined with electrochemical and electrostatic concepts to further regulate flow²¹⁻²³. In addition, the capillary concept can be employed for liquid handling purposes, e.g. valving, when active forces such as centrifugal or pneumatic forces are the primary means to drive fluid flow²⁴⁻²⁶. For instance, the capillary concept was used in a wearable microfluidic device to regulate the sequential flow of liquids, with the device primarily powered by pressure generated via sweat glands and centrifugal forces²⁷.

This review is focused on self-filling capillary microfluidics which generates negative pressure to drive flow. Such capillary microfluidic devices can be designed by systematically combining different fluidic compartments from a library of “capillanic elements”. Fluidic systems assembled in such a manner were termed “capillanic circuits” (CCs) by Safavieh et al, which

conveys the notion of a circuit assembled from basic capillarity elements²⁸. Here, we first start with a brief historical perspective that describes the development of CCs over time. Next, we describe the physical properties governing microchannel-based capillary flow and continue by explaining various capillary elements and their principles of operations. Then we describe the integration of capillary elements into self-regulated CCs for performing liquid handling operations, notably sequential delivery. We next point to the main applications of CCs in diagnostics and the recent progress in rapid prototyping of CCs.

5.1.2. The 3 waves of developments in capillary microfluidics

Microfluidic CCs have a history that goes back to 30 years ago. As illustrated in Fig. 1, there exist 2 established waves of development that can be classified according to the manufacturing technology: (i) classical mechanical micromachining and (ii) photolithography-based chemical micromachining. More recently, the 3rd wave of manufacturing technology rendered by additive manufacturing and rapid prototyping is emerging.

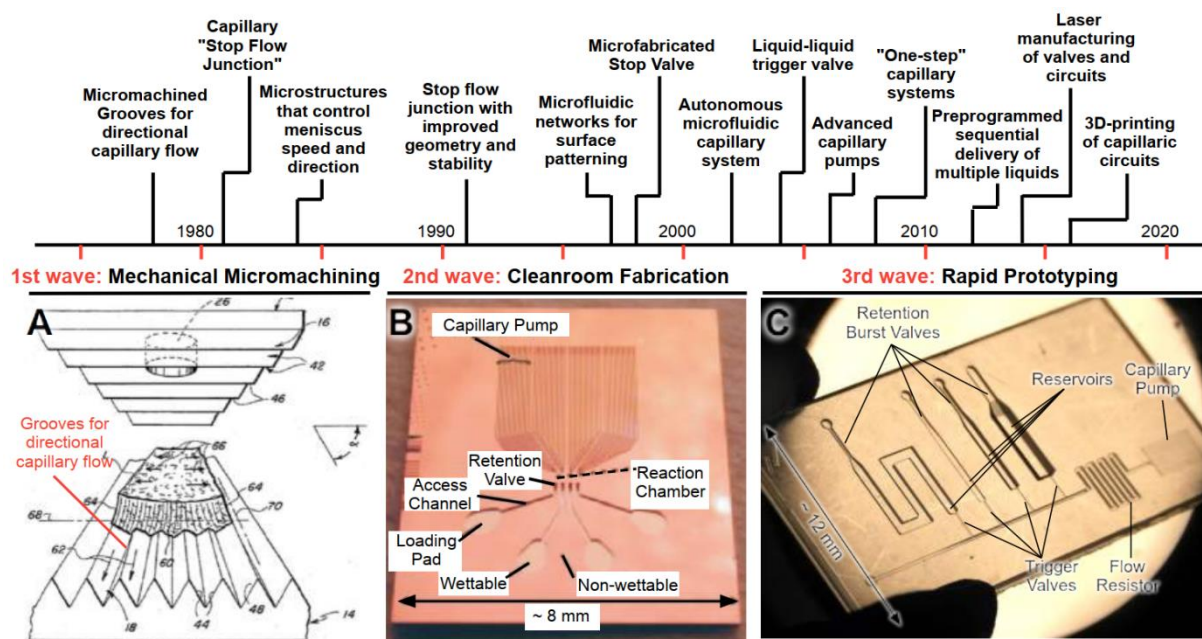


Figure 1. **3 stages of development in microchannel-based capillary microfluidics. The main developments are indicated in the figure.** (A) The 1st wave was mainly developed in industrial labs. (B) The 2nd wave was developed following the emergence of micro-total analysis systems (μ TAS) and the usage of photolithography, micromachining, and soft lithography in microfluidics. (C) The 3rd wave is associated with the emergence of rapid prototyping technology, such as laser cutting and 3d printing, enabling rapid design and optimization processes. (A - C) Ref.¹⁷

5.1.2.1. 1st wave: mechanical micromachining and lamination

The 1st wave of CCs is associated mostly with the development of capillary-driven liquid handling devices in the industrial, rather than academic, research labs. Micromachined grooves to guide directional capillary-driven transport²⁹, and abrupt geometrical changes to stop flow^{30,31} were among the first capillary-driven microfluidic devices in the literature. As an example, Fig. 2A indicates how microstructures were utilized to guide liquid filling front without bubble entrapment³². Other developments in this wave include: (i) Capillary stop-valves to halt fluid flow at an abrupt geometrical enlargement³⁰ (Fig. 2B), (ii) autonomous dilution devices powered by capillarity and gravity³³ (Fig. 2C), (iii) matrix plugs for the delay

and sequential draining³⁴ (Fig. 2D), and (iv) capillary pumps implemented with gaps to avoid back flow³⁵ (Fig. 2E).

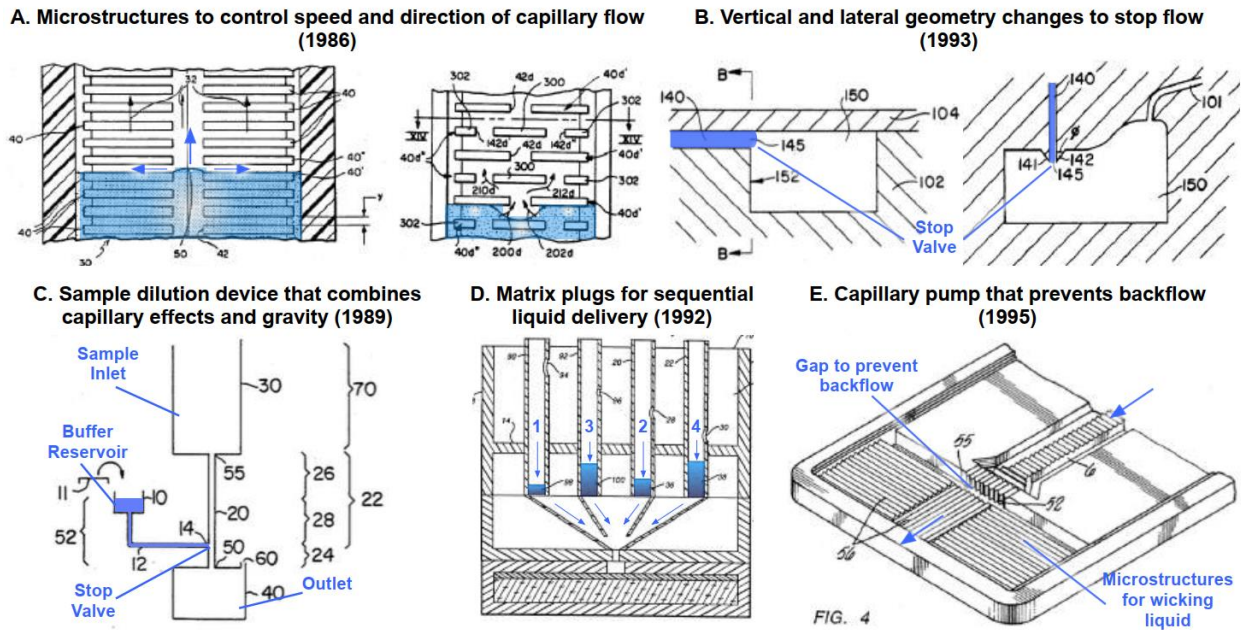


Figure 2. **Examples of micromachined devices in the 1st wave of development.** (A) 2 examples of microstructures that regulate speed and direction of flow with bubble entrapment. (B) Examples of capillary stop valves to halt the flow. (C) A porous matrix plugs for dilution and mixing of liquid samples. (D) Matrix plugs for the delay and sequential draining (E) Capillary pumps with microstructure to enable directional filling and avoid backflow. (A – E) Ref.¹⁷

5.1.2.2. 2nd wave: Cleanroom fabrication

The 2nd wave of development is related to the adaptation of photolithography and cleanroom processes for micro total analysis systems (μ TAS) applications³⁶. Delamarche and colleagues first utilized capillary-driven microfluidic devices for chemical and biological applications^{37,38}. More advanced microfluidic systems were developed for self-powered and controlled liquid delivery sequentially applied to an inlet³⁹. Subsequently, fully autonomous, pre-programmed sequential delivery of reagents to render an immunoassay was developed^{40–43}, and the concept of CCs was introduced²⁸. Silicon (Si) substrates are among the early materials

employed for CC fabrication due to the available technologies and accessibility to the microfabrication tools^{37,43–45}. In a relatively less labor-intensive process, CCs were fabricated via soft lithography which obviated the need for repetitive usage of the cleanroom facility^{28,46}. CCs were also fabricated via mass-producible means such as injection molding of thermoplastics such as cycloolefin-copolymer (COC)⁴⁷. A more detailed explanation of this subject is provided in the next sections.

5.1.2.3. 3rd wave: Rapid prototyping

Rapid prototyping techniques such as laser cutting and 3D printing have shown promising potential for rapid and cost-effective fabrication of CCs^{48–51}. CO₂ laser cutting has been used for manufacturing capillary elements^{48,50} and stereolithography 3D printing was employed to fabricate molds that can be replicated into PDMS^{49,52,53}. One limitation of rapidly prototyped devices is their limited resolution as laser cutting technique cannot generally achieve a feature size of less than $< 200 \mu\text{m}$ and commercially available 3D printers are limited to the feature size of $100 \mu\text{m}$ in the horizontal plane and $20 \mu\text{m}$ in the vertical direction⁵⁴.

5.1.3. Fundamental parameters and equations

Before explaining the working principles of various capillary elements, it is important to summarize the fundamental parameters and equations that govern their operations.

5.1.3.1. Wettability and contact angle

A surface is wettable if the contact of water on the surface is less than 90° . Microfluidic channels with a wettable surface create negative capillary pressure with a concave liquid-air interface that drives liquid flow within the microchannel.

5.1.3.2. Capillary pressure

Flow in a capillary microchannel is due to capillary pressure. This is the reason that liquids advance vertically in capillary tubes to a higher height which is dependent on the surface tension of the liquid and the geometry of the microchannel⁵⁵. In capillary microchannels, capillary pressure at the liquid-air interface increases due to the surface tension of the liquid and the curvature created by the fixed contact angles, which will generate negative sucking pressure. Most microfabricated channels in capillary-driven microfluidics possess rectangular cross-sections due to the use of planar photolithography and rapid prototyping fabrication techniques. For a rectangular microchannel, the Young-Laplace equation that explains the relation between microchannel geometry, contact angle, and capillary pressure⁵⁶ is expressed as follows⁵⁷:

$$P = -\gamma \left[\frac{\cos\theta_t + \cos\theta_b}{h} + \frac{\cos\theta_l + \cos\theta_r}{w} \right] \quad (1)$$

Where P is the capillary pressure, γ is the liquid surface tension, h and w are the height and width of the microchannel respectively, and θ_t , θ_b , θ_l , θ_r are the contact of the liquid with the top, bottom, left, and right side of the microchannel respectively.

For very wettable surfaces, corner flow - a phenomenon that arises at the intersection of two wettable surfaces with a contact angle of less than 45° - is an important effect that can yield in deviation from the behavior explained by the eq. 1⁵⁸. The effect of corner flow is especially pronounced when the walls of a microchannel have different contact angles or when the microchannel has a very high (or low) height-to-width ratio.

5.1.3.3. Flow rate and flow resistance

As stated before, most microfabricated channels have a rectangular cross-section. An expression for the flow rate of liquid in a microchannel is obtained from Navier-Stokes equations. For laminar flow in microchannels with the assumption of steady-state flow in the absence of gravitational forces, a simplified analytical expression for the flow rate of liquid in a rectangular microchannel can be obtained. The expression can further be simplified for a flat and very wide microchannel, i.e. $\frac{h}{w} \rightarrow 0$, as follows⁵⁹:

$$Q \approx \frac{h^3 w \Delta P}{12 \eta L} \left(1 - 0.630 \frac{h}{w}\right) \quad (2)$$

Where Q is the flow rate, h and w are the height and width of the microchannel respectively, L is the length of the microchannel, ΔP is the difference in capillary pressure across the length of the microchannel, and η is the viscosity of the liquid.

The worst-case scenario for the assumption of a very flat and wide microchannel is when $h = w$. In this case, the approximation differs for the exact analytical value by 13%, but it will decrease to 0.2% when $h = \frac{w}{2}$ ¹⁷.

Based on electrical analogies, the relation between flow rate and capillary pressure can be written as follows:

$$Q = \frac{\Delta P}{R} \quad (3)$$

Where R is called the resistance of the microchannel. Thereby, it can be expressed as follows¹⁷:

$$R = \frac{\Delta P}{Q} = \frac{12 \eta L}{h^3 w} \left(1 - \frac{0.630 h}{w}\right)^{-1} \quad (4)$$

Instantaneous flow resistance and capillary pressure determine the filling behavior of microchannels and are employed to derive scaling laws that help in designing capillary-driven microfluidic chips. It is important to note that, unlike the electronic circuits that are preloaded with electrons, the relationship between flow rate and flow resistance changes as the liquid progresses within the microchannel. The capillary pressure difference, i.e. ΔP , is the instantaneous pressure at the liquid-air interface which can undergo large variations upon considerable changes in the geometry of the microchannel¹⁷.

5.1.4. Foundations of capillaric circuits

Currently, the most common technique for the fabrication of CCs is photolithography in the cleanroom. In this regard, one of the most common methods for fabricating the CCs is direct patterning of Si wafers achieved by deep reactive ion etching which creates geometrical features with an aspect ratio of up to 20:1^{39,57}. However, this technique requires an expensive cleanroom facility and suffers from slow design-to-device time as well as the complexity of the fabrication process¹⁷.

A simpler and more cost-effective alternative is the soft lithography technique. A negative version of the CC is created by patterning the design as ridges on a Si wafer, followed by replicating the design into a soft and transparent PDMS. Upon fabricating a single Si wafer with a positive pattern, multiple PDMS replicates can be prepared using common consumables and an oven⁶⁰. Although PDMS replication is relatively fast for academic purposes, it is too slow (~hours) and rather expensive for mass production as compared to hot embossing (~minutes) and injection molding (~seconds)¹⁷. This can be circumvented by using the PDMS replicate as a mold and replicating it into polymers that can be UV-cured

within seconds⁶¹. Even though hundreds of PDMS replicates can be made from a single Si mold, still there exists the need for familiarity with the mold design and the use of cleanroom facilities¹⁷.

5.1.5. Materials and surface chemistry

Various materials, such as glass, silicon, and polymers, have been utilized for the fabrication of CCs. The wettability of the material is of great importance in inducing capillary-driven flow within the CCs. Even though glass and silicon are hydrophilic with the contact angle of 25° and 52° respectively, many polymers such as poly(methyl methacrylate) (PMMA) and PDMS are hydrophobic with the contact angle of 71° and 107° respectively. Therefore, surface treatment is required to obtain sufficient hydrophilicity and generation of capillary pressure for the fully autonomous operation of capillaric elements¹⁷.

One of the most common techniques for surface treatment is the usage of gas-phase treatment which subjects the surface of the substrate to plasma, ozone, or UV light. In this technique, oxygen radicals with high energy are generated and bombarded to the surface of the substrate to oxidize the surface and render it hydrophilic. The gas-phase treatment technique is relatively fast and can render a surface hydrophilic within seconds¹⁷. Another surface treatment technique for hydrophilicity is vacuum-based or solution-based surface grafting of silanes with hydrophilic end groups, e.g., polyethylene glycerol (PEG), with anti-folding properties⁶². PEG surface treatment yields in contact angle of 30 – 60° which is suitable for the proper function of most capillaric elements¹⁷.

One important consideration regarding the technique for surface treatment is the stability and longevity of the surface treatment. Silicon, glass, and many polymers remain hydrophilic

after treatment with plasma or silane. However, PDMS reverts to its hydrophobic state after plasma or silane treatment⁶³. UV-curable polymers such as Norland Optical Adhesive with the ability to retain stable hydrophilic surface could be used as an alternative to PDMS for academic laboratory usages⁴⁶.

5.1.6. Capillarity elements

A typical CC is illustrated in Fig. 3 using symbolic representation adapted from electronic schematics²⁸. Conceptually, CCs can be designed by combining different capillary elements to form fully autonomous microfluidic devices for self-regulated and self-powered liquid handling. Flow in a CC is generated via the self-filling property of the microchannel and retained by capillary pumps after filling of the microchannel. Capillary elements functionality is realized when the liquid-air interface reaches a specific element during filling (or draining). After filling, capillary elements act simply as a flow resistor. Therefore, as described previously, the flow resistance increases as a CC is being filled and decreases as the liquid is being drained from the CC. In what follows, the conceptual working principles, design, limitations, and capabilities of different capillary elements, in theory, and practical implementation, on the regulation of flow within a CC will be discussed.

5.1.6.1. Vent

An air vent is a capillary element to ensure that the liquid is able to fill microchannel(s) within the CC without air bubble formation. Vents can be created simply by partially covering CC and leaving the rest exposed to air, or by punching the access hole(s) in the cover or the CC. Vents could be rendered hydrophobic to ensure flow stoppage. Filling of vents with liquid is also

feasible, but they should stop the liquid in a pre-programmed manner once filled. Vents are simple, but the essential element in a CC to ensure proper fluid flow¹⁷.

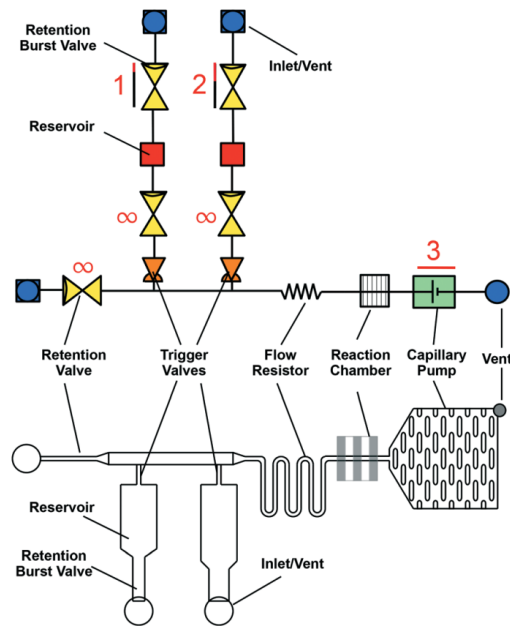


Figure 3. **Symbolic representation of a capillary circuit.** Symbolic (top) and schematic (below) representation of a typical capillary circuit comprised of various capillary elements as illustrated in the figure. Ref.¹⁷

5.1.6.2. Inlet

Inlets are the entry section of liquid(s) to the CC and serve as the user interface. In laboratory prototyped CCs, inlets are often designed as a shallow and wide structure that is left open after sealing of the microchannel⁵¹. Such inlets are easy to fill in the laboratory by pipette. However, for point of care purposes, inlets should be designed so that they can be easily filled by an untrained person, e.g. by applying a sample from a finger prick directly into the inlet. If necessary, blood plasma filters can be implemented into the inlets to ensure the filtering of blood cells and allow only entry of plasma to the CC⁶⁴.

Some practical challenges are to be considered while designing a CC. There exists the possibility of cross-contamination or mixing of liquids from different inlets if the inlets are too

close to one another or the CC is too hydrophilic. To prevent this, the neighborhood of the inlet can be rendered hydrophobic while keeping the inlet and the microchannel hydrophilic to ensure that the liquid only enters the designated inlet without overflowing to another inlet⁶⁵. Another practical consideration is that due to the high capillary pressure of the microchannel which tends to retain liquid, the back flow of the liquid from the microchannel to the inlet might happen upon evaporation¹⁷. To avoid the effect of corner flow in the inlets, they can be literally removed, and the liquid can directly be applied to the narrow conduit which protrudes from the edge of the CC and is exposed to air⁵¹. Inlets are simple, but yet an essential element of CCs and required to be designed in a user-friendly manner without interfering with subsequent fluidic operations.

5.1.6.3. Reservoir

The reservoir is a common element in CCs. It is basically a microchannel or a serpentine to hold and subsequently drain a precise volume of liquid in a pre-programmed fashion. Reservoirs guide the fluid flow from the inlet towards the other capillaric elements within a CC. Their capacity can vary from picoliters³⁹ range to hundreds of microliters⁵¹. Reservoirs need to have relatively low flow resistance and low capillary pressure to ensure easy filling and draining and to avoid bubble formation due to the corner flow effect. One practical consideration is to minimize the surface that is exposed to air to lessen the effect of evaporation and unwanted exposure of sample or reagents, such as whole blood, to the user¹⁷.

5.1.6.4. Reaction chamber

Reaction chambers are the area in the CC where (bio)chemical reactions are performed. Like those of active microfluidics, reaction chambers in CCs need to be designed to ensure desired

mass transport and effective analyte capture. A common reaction chamber in CCs is simply a microchannel with patterned reagents on the PDMS cover^{37,39}. The self-sealing characteristic of PDMS together with the negative pressure present in a CC ensures leakage-free sealing even in the presence of adsorbed protein on the surface of the PDMS. Reaction chambers can have a spiral or zigzagged geometry to provide sufficient incubation time for the (bio)chemical reactions^{43,66}. Functionalized microbeads could be utilized in reaction chambers to increase surface area and facilitate mass transport within the CCs⁵¹. CCs need to be designed by considering the concentration of the analyte of interests, liquid operations within the CCs, and user-friendliness of the CC.

5.1.6.5. Flow resistor

Flow resistance is commonly generated by the viscous flow resistance of liquid flowing in a microchannel. Flow resistance in a flow resistor can be modulated by changing the geometry and length to achieve desired filling or draining flow rate⁶⁷. It should be noted that changing the microchannel dimensions can affect both flow resistance and capillary pressure. For instance, for a microchannel with a height significantly greater than the width ($h \ll w$), the capillary pressure is proportional to $1/h$ and the flow resistance is proportional to $\frac{1}{h^3}$. Therefore, decreasing the height of a microchannel increases flow resistance to a greater extent as compared to the capillary pressure, which yields in the overall reduction of flow rate by $\frac{1}{h^2}$ and flow speed by $\frac{1}{h}$ ¹⁷.

One approach to reducing flow resistance while keeping the capillary pressure the same is to use multiple parallel microchannels. Flow resistance, in this case, can be systematically altered to investigate the effect of incubation time on the assay performance, i.e. the level of

signal detected⁶⁸. Flow resistors can also be used as a mixer module as they provide a long residence time to allow for diffusive mixing^{66,68}. Systematic changes of flow resistance in parallel microchannels were utilized as reagent integrators for efficient rehydration of dried reagents. Flow resistors can also be used to provide capillary pressure drop, in analogy to electric drop across an electric resistor, to modulate capillary pressure in a CC and subsequent fluidic operations⁵¹.

5.1.6.6. Capillary pump

Capillary pumps are essential in CCs (Fig. 4). They drain liquids from the CCs to allow for the desired reaction(s) to happen while simultaneously acting as a waste reservoir. Capillary pumps need to provide a steady flow rate, by generating constant capillary pressure, regardless of filling level, meaning that the pump should not significantly increase the overall flow resistance of the whole CC. The first designs of the pumps included arborescent structures by having multiple parallel channels to minimize the flow resistance of the pump⁶⁹ (Fig. 5). Various geometrical features of pump microstructure have been investigated so far⁴⁴ (Fig. 6).

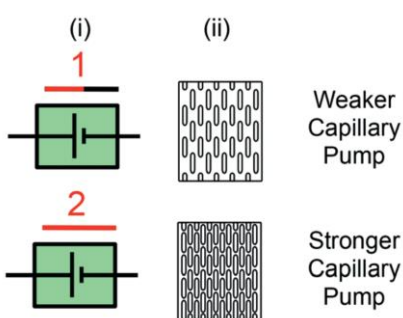


Figure 4. **Capillary pump**. Schematic (i) and symbolic (ii) representation of capillary pump. The spacing between the microstructures is related to the capillary pressure of the pump, with stronger pumps having less space as compared to the weaker ones. Ref.¹⁷.

Another task of capillary pumps is to meter the precise volume of liquids within a CC. However, capillary pumps need to have small features to generate high capillary pressure for draining the liquids from a CC. The geometrical features of the pumps should be proportional as microstructure with relatively large width and shallow depth might not work as expected due to bubble generation in the center of the pump structure. This is due to the fact that in wider microchannels, liquid preferably advances from the edge which can result in reaching the outlet before filling the center of the microchannel at the upstream and thus creating air bubbles¹⁷. Another important consideration is that the pump needs to be covered to minimize the effect of evaporation⁷⁰.

Arborescent capillary pumps are filled effectively without bubble formation, but the pump resistance increases monolithically by the capacity of the pump. Furthermore, at the branching points, the gaps are wider which results in reducing the capillary pressure. Advanced capillary pumps with microfabricated structures were designed to address this issue at the branching areas. The micro-posts also possess a greater open or void ratio which allows them to retain a greater volume of liquid within the same device footprint¹⁷.

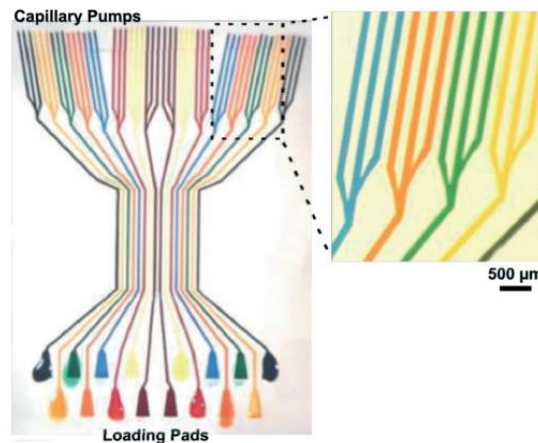


Figure 5. **Capillarc circuit with tree line capillary pumps.** 16 CCs each having a capillary pump comprising 3 branches. The inset illustrates the capillary pump. Ref.¹⁷

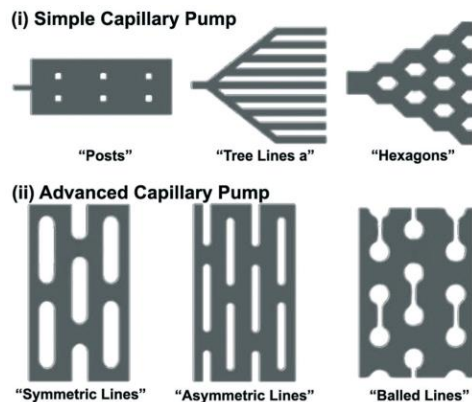


Figure 6. **Microstructures for capillary pumping.** Capillary pumps with differing geometrical features. Ref.¹⁷

One way to increase the capacity of capillary pumps is by mimicking nature by combining capillarity and evaporation⁷¹. Porous materials can also be connected to a capillary pump to increase the capillary pump capacity⁷². Paper pumps can also act as capillary pumps which in this case the capillary pressure in the paper pump determines the speed of fluid drainage from the CC. One practical consideration is to ensure proper connection of the paper pump to the CC to avoid the creation of air gaps which can result in a reduction in flow rate. Prewetting the paper pump before connection to the CC can address this issue⁵¹. Synthetic polymer paper pumps including arrays of interlocked micropillars indicated improved control of fluid flow as compared to the convention porous materials⁷³. Hydrogels⁷⁴ and superabsorbent polymers⁷⁵ were also employed as capillary pumps.

5.1.6.7. Filling front guides

Filling front guides essentially control the path of the liquid front (and sometimes liquid bulk) through a preprogrammed path in a CC. Generally, liquids prefer to fill smaller channels with

higher capillary pressure first as compared to bigger channels with lower capillary pressure. This is driven by filling front guides which guarantees bubble-free filling of microchannels in a CC. The first liquid front guides with the use of capillary phenomenon were developed on glass via silane chemistry, forming invisible liquid guides which were filled by positive as well as negative pressure⁷⁶. Another study used a Si wafer with a hydrophilic microchannel sealed with a hydrophobic glass slide with the ability to support continuous filling while guiding the liquid to the microchannel⁷⁷.

More recently, filling front guides have been exploited to ensure proper filling of capillary pumps. For instance, a previous study developed a multicompartiment capillary pump by placing a large 60 μm channel at the center connected to components of smaller size (30 μm). Filling of the unit downstream can only be realized when the previous one has been filled completely⁷⁸ (Fig. 7). A pump with such a structure possesses relatively low flow resistance as the flow advances through a wide central channel to the downstream compartments. Precise control and spacing of microstructures in a capillary pump can be achieved by deterministic control of the liquid filling front. By precisely arranging the filling front guides, capillary pumps with different embodiments, i.e. serpentine (Fig. 8) or leading-edge, can be designed⁷⁰.

Phaseguides, which are made from small bumps or dips in microchannels, are another element allowing for the guiding of liquid in a microchannel. Phaseguides with different pressure can allow for liquid flow in a certain path⁷⁹.

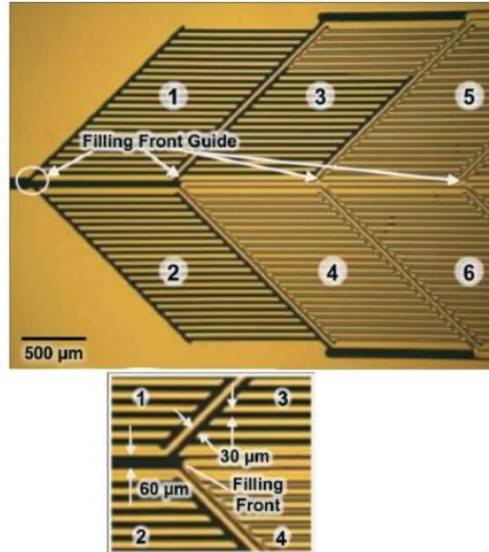


Figure 7. **Capillary filling front guide for liquid distribution into 6 different zones.** The areas filled with liquid appear to be darker. Ref.¹⁷

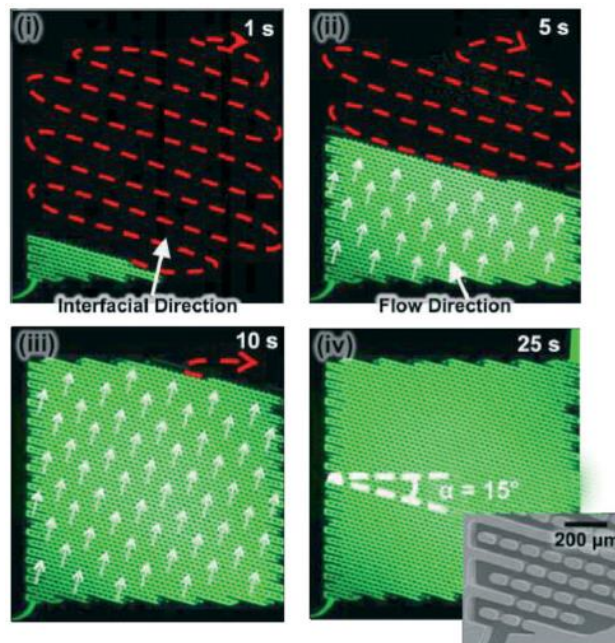


Figure 8. **Serpentine capillary pump for guiding liquid front.** The micro-post arrangement creates areas of high and low capillary pressure, resulting in the movement of liquid filling front in a serpentine manner. Inset in sub-panel (iv) shows the scanning electron microscopy image of the pump. Ref.¹⁷

Stop-valve

Stop valves essentially stop the fluid flow at a specific point in a CC due to an abrupt change in geometry (Fig. 9). Liquids stop when they face an abrupt change in the cross-section of the microchannel where they are flowing^{78,80}. The theoretical principles regarding the operation of stop-valves have been provided elsewhere⁸⁰. The geometrical parameters that influence the pressure barrier by a 2D stop valve are illustrated in Fig 9A. For a 2D stop valve, the pressure barrier is given by⁸⁰:

$$\Delta P = \frac{2\gamma}{h} \left(\frac{\cos\theta - \frac{\alpha \sin\beta}{\sin\alpha}}{\cos\beta + \frac{\sin\beta}{\sin\alpha} \left(\frac{\alpha}{\sin\alpha} - \cos\alpha \right)} \right) \quad (5)$$

Where h is the height of the microchannel, θ is the liquid contact angle, α is the curvature in the liquid meniscus in the lateral direction, and β is the change in the curvature of the liquid meniscus as shown in Fig 9A.

Even though stop valves are simple, reliable, and easy to incorporate in active microfluidic devices, their reliability in passive microfluidics has only been investigated for short durations (e.g. 5 min). Very low contact angles may yield in corner flow which disrupts the functionality of stop valves and depending on the geometry, bubble formation might occur¹⁷.

Two-level stop valves have been developed to improve the functionality of stop valves (Fig. 9B). The performance of two-level stop valves was numerically and empirically investigated as a function of the hydraulic diameter of the microchannel and contact angle⁸¹. 3D stop valves have been used for patterning antibodies in a closed microfluidic chip⁸². The need for an external actuation to resume the flow stopped at the stop valve has limited the use of stop

valves in the CCs⁸⁰. Stop valves can readily be turned into trigger valves by implementing the flow stoppage at an intersection with an orthogonal channel, which allows for the resume of the flow stopped at the stop valve when the second liquid flows in the orthogonal channel and crosses the intersection.

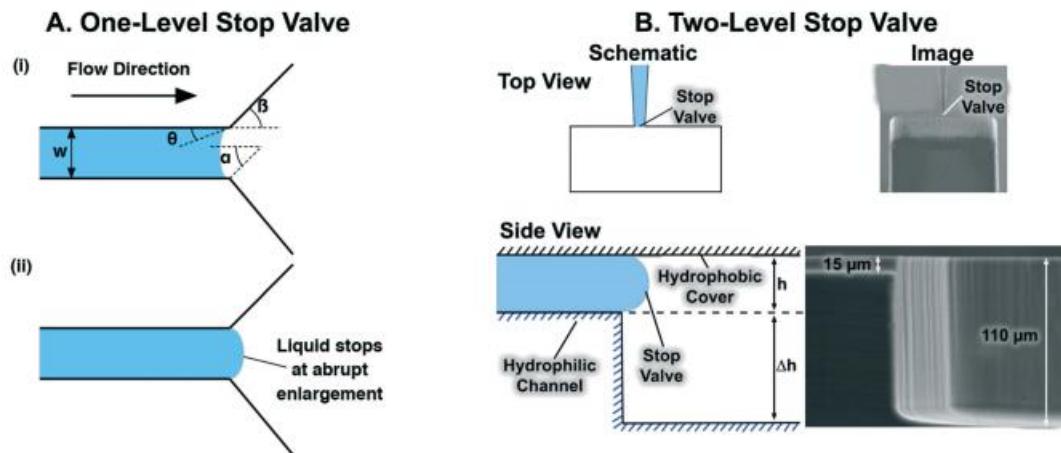


Figure 9. **One-level and two-level stop valves.** (A) (i) Schematic of a one-level stop valve with the key parameters used in eq. 5. (ii) Schematic of a stop valve when the liquid flow is stopped. (B) Schematic and real images of the capillaric elements for stopping or retaining flow. (A, B) Ref.¹⁷

5.1.6.8. Capillary trigger valve

Capillary trigger valves are modifications to the capillary stop valves which enable both stop and resume of fluid flow within a CC. The first trigger valves in the literature included multiple microchannels at a junction and required all microchannels to be filled in a specific order for proper function. These trigger valves were made of Si and required very high aspect ratios (e.g. $\frac{h}{w} = 12.5$) for successful liquid stoppage⁸³. To reduce the fabrication constraint and further improve the reliability of two-level trigger valves, designs with a lower aspect ratio have been proposed²⁸. Instead of narrowing two microchannels into an intersection, two-level trigger valves possess microchannels that meet at an orthogonal intersection (Fig. 10).

Two-level trigger valves are more reliable than one-level stop valves and can successfully hold liquid for up to 30 min^{28,51}. Larger dimensions can also be implemented in two-level stop valves as the microchannel step height can be regulated to provide a sufficient pressure barrier to halt flow¹⁷.

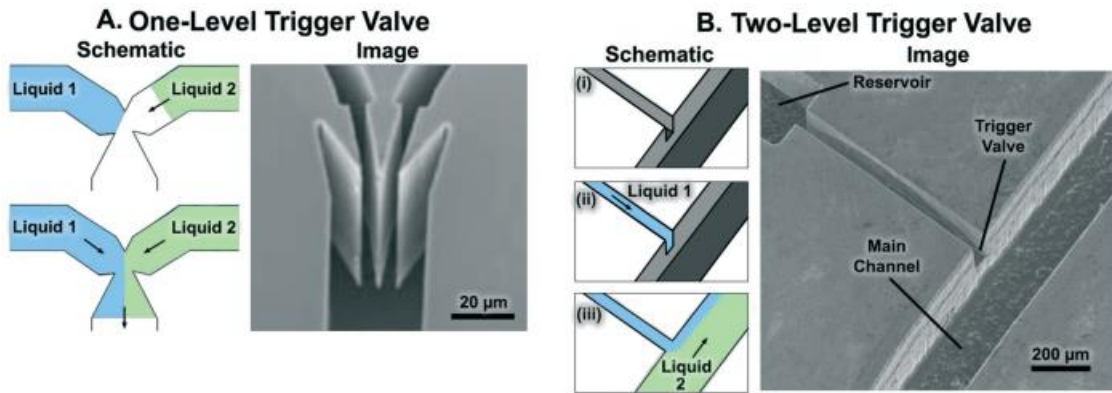


Figure 10. **One-level and two-level trigger valves.** Schematic and scanning electron microscopy (SEM) image of one-level and two-level trigger valves. (A, B) Ref.¹⁷

5.1.6.9. Temperature-controlled valves

Another approach for controlling stop and resume of flow can be realized by temperature-controlled stop valves. To this end, Li et al. grafted poly(N-isopropylacrylamide) (PNIPAm) on the walls of a rectangular microchannel to change the hydrophilicity/hydrophobicity of the walls locally⁸⁴. PNIPAm is hydrophilic at 20 °C but it becomes hydrophobic at 36 °C. Therefore, by raising the temperature to 36 °C, using a heater, the liquid stops and once the temperature goes down to 20 °C, the flow resumes (Fig. 11).

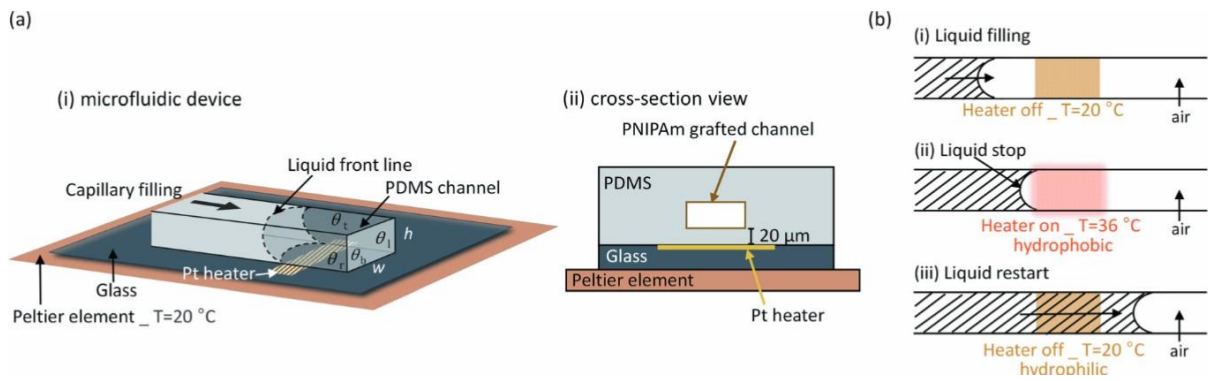


Figure 11. **Layout of the temperature-controlled valving.** (a) The schematic illustration of the temperature-controlled valving. The PNIPAm is grafted locally at the cross-section of a microchannel made from PDMS. A Peltier element is located at the bottom of the device to control the temperature. (b) capillary driven filling at 20°C (i), liquid stoppage at the locally grafted PNIPAm cross-section at 36°C (ii), and flow resume when the heater is off to decrease the temperature to 20°C . Ref.⁸⁴

5.1.6.10. Capillary soft valves

Capillary soft valves use a pressure barrier like a capillary stop (or trigger) valve to stop the liquid flow at a specific point (Fig. 12). Flow is resumed by applying manual pressure on a soft cover that deflects in the microchannel^{85,86}. When the PDMS cover is pushed down, the height of the microchannel is reduced which increases the value of the negative pressure in the neighborhood of the capillary soft valve and subsequently restarts the flow in the microchannel. One drawback of the capillary soft valves is that they require manual intervention to resume flow which can limit their scalability. However, this might be desirable depending on the application as it allows for interactive flow control.

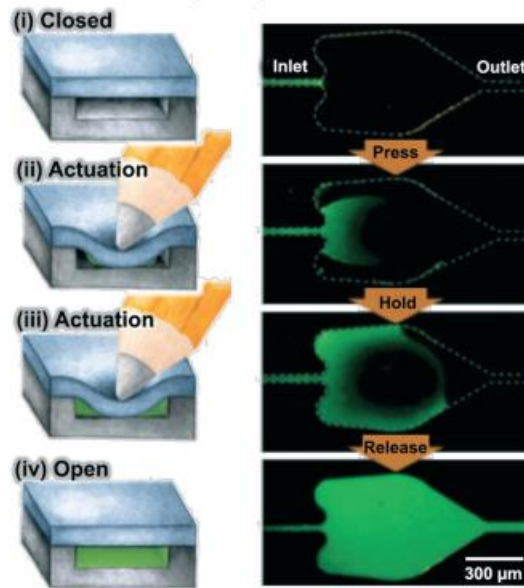


Figure 12. **Capillary soft valve.** The workflow mechanism is shown in the schematic (left) and fluorescent microscopy (right) representation. Ref.¹⁷

5.1.6.11. Capillary retention valves

Capillary retention valves (CRV) play a role when a CC is draining as they retain the liquid in a specific region of a CC by capillary pressure (Fig. 13). By implementing a retention valve at the inlet of a reaction chamber, it is feasible to introduce reagents one after another, as they are being drained from the inlet via the capillary pump, while the CRV prevents complete liquid drainage, air bubble formation, and drying of reaction chamber^{87,88}. CRVs are realized simply by reducing the size of the microchannel to generate a capillary pressure greater than that of other capillary components downstream, such as the capillary pump, guaranteeing that they do not drain during the chip draining session (Fig. 13). This however can create a constraint since it will limit the maximum capillary pressure of the capillary pump.

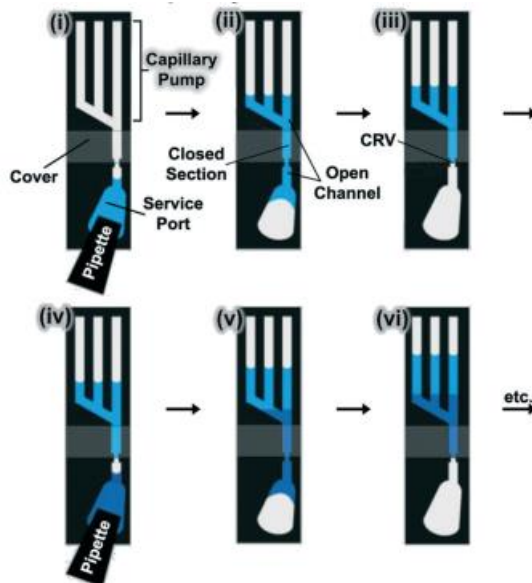


Figure 13. **Capillary retention valve.** Capillary retention valve (CRV) and its working mechanism in schematic representation. CRV in this case allows for sequential loading of various reagents without bubble entrapment. Ref.¹⁷

5.1.6.12. Retention burst valves

Like CRVs, retention burst valves (RBVs) operate during the drainage session (Fig. 14). They allow for preprogrammed drainage of liquid in a reservoir at a predefined bursting pressure encoded by the geometry of the RBV. The sequence of reagent drainage can be preprogrammed by implementing an RBV at the beginning of each reservoir with a specific bursting pressure. Like CRVs, RBVs can also be realized by simply reducing the size of a (micro)channel. The precise burst pressure can be calculated via the Young-Laplace equation and modulated experimentally^{28,49}. The range of the capillary pressure that can be encoded is limited to the capillary pressure of the pump, as the pump pressure needs to be higher than that of the strongest RBV to ensure liquid drainage from all RBVs.

To ensure the successful operation of RBVs, several conditions need to be satisfied. First, the capillary pressure of the RBVs must increase monolithically. Second, the difference between

the capillary pressure of the RBVs should be large enough to ensure the draining of only one RBV at a time. Third, the CC must be designed such that the pressure at each reservoir is below the bursting pressure during the draining session¹⁷.

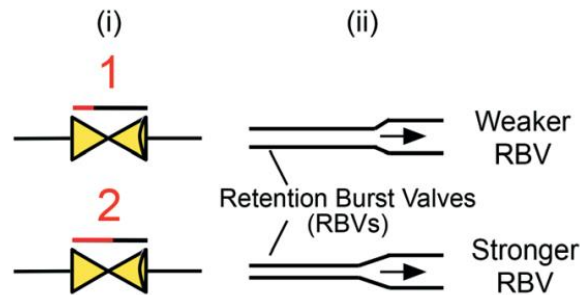


Figure 14. **Retention burst valve.** Symbolic and schematic representation of a retention burst valve. Arrows indicate the flow direction. Ref.¹⁷.

5.1.6.13. Capillary domino valves

Recently, Yafia et al. introduced a new concept called “microfluidic chain reaction (MCR)” to execute autonomous liquid handling algorithms by structurally programming capillary flow events on a CC¹². MCR works on the basis that activation of one event (i.e. event #n) is realized only upon the completion of the precedent event (i.e. event #n-1). This is realized by a particular capillaric element called the capillary domino valve (CDV). Overall, a CDV is comprised of 2 RBVs at the top and bottom that are connected via an air link. Draining of the bottom RBV brings the ongoing capillary flow event to the end and exposes the top RBV to the atmospheric pressure to initiate the next capillary flow event (Fig. 15).

instance, the Biosite's Triage™ chip includes a hydrophobic delay valve to provide sufficient sample incubation time which is subsequently rendered hydrophilic upon the adsorption of the proteins at the liquid front.

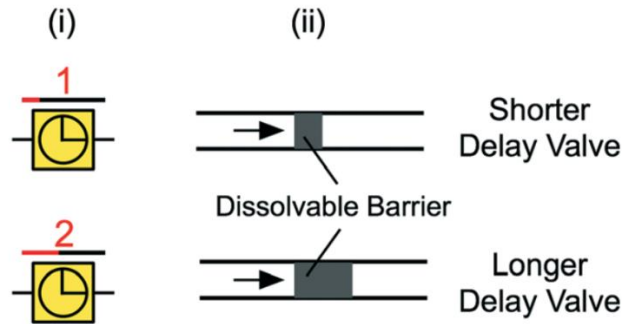


Figure 16. **Delay valve.** Symbolic and schematic representation of a delay valve. Arrows indicate flow direction. Ref.¹⁷.

5.1.6.15. Transistor valve

Meffan et al. reported a new category of capillaric elements to regulate flow upstream by obtaining feedback from the flow downstream⁹¹. In particular, they developed a transistor valve by which air bubbles can be introduced upstream by receiving commands from the downstream flow to execute a fluidic function. Fig. 17A depicts the working principles of the developed transistor valve, and Fig. 15B illustrates the function of the transistor valve as an “off” valve to execute the metering function.

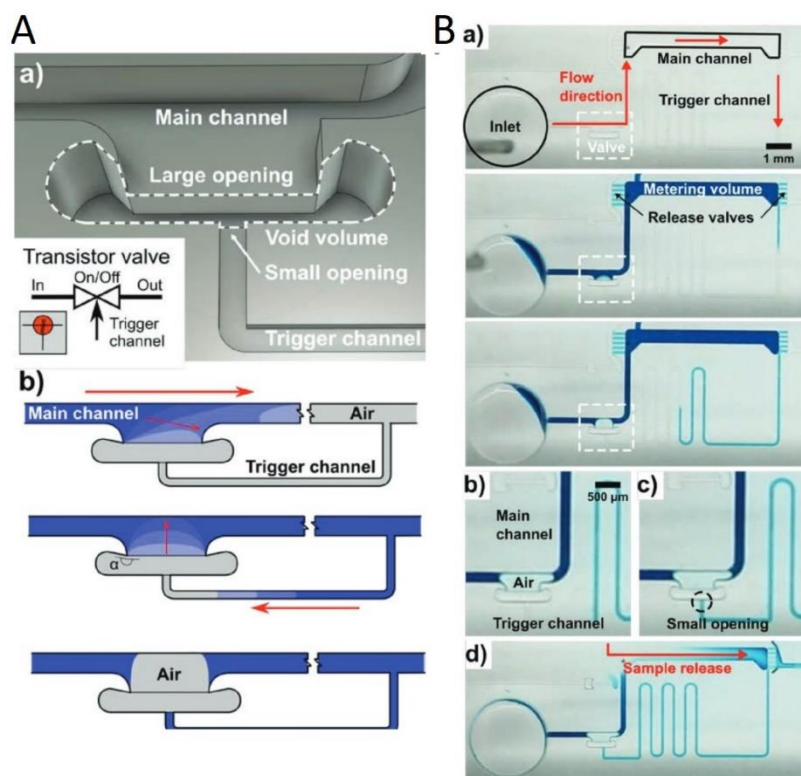


Figure 17. **Layout of the transistor valve and its application as an “off” valve.** (A) design, symbolic representation, and the workflow of the transistor valve. (B) The application of the transistor valve as an “off” valve to realize the metering function. The filling of the trigger channel implemented downstream imposes an air bubble upstream and leaves a metered volume for the sample. Ref.⁹¹

5.1.7. Capillary circuits for sequential delivery

5.1.7.1. Sequential delivery via retention valves

The first implementation of multiple capillary elements including capillary pump, CRVs, vents, and inlets into a single CC was performed by Juncker et al. Liquids in the CC were retained via capillary retention valves at the inlet which enabled sequential loading of multiple reagents. The circuit was used to perform 16 sequential delivery steps to detect C-reactive protein within 25 min³⁹. Similar designs were employed for the automation of micromosaic immunoassays in which multiple lines of capture antibodies were patterned on

a reaction chamber and subjected to an orthogonal flow of different analytes, enabling simultaneous detection of multiple analytes^{65,92}. Fig. 18 illustrates an example of multiple sequential deliveries actuated by retention valves⁹³.

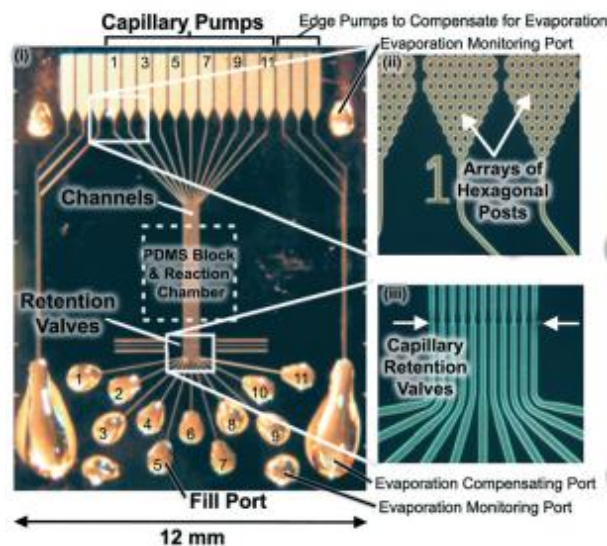


Figure 18. **Manual sequential delivery with retention valves.** 11 parallel CCs for performing a multi-step immunoassay. The capillary retention valve in the CCs prevents drainage of the reaction chamber and bubble entrapment when the next solution is applied to the inlet. Ref.¹⁷

5.1.7.2. Sequential delivery via trigger valves and retention burst valves

In this type of system, the sequential delivery is rendered by having multiple branches wherein each includes reservoirs, RBVs, and trigger valves. The trigger valve connects each branch to the main channel, called releasing channel, which leads to the reaction chamber and capillary pump. The time-lapsed images of sequential delivery powered by a capillary trigger valve and RBV are illustrated in Fig. 19. The reservoirs can be filled arbitrarily. The filling of releasing channel connects the whole circuit to the capillary pump and triggers sequential delivery in the CC wherein the RBV with the smallest capillary pressure drains first. It is important to note that as the circuit drains, the pressure across the CC drops, rendering

the pressure in the CC lower than the burst pressure of the next weakest RBV. When the 1st reservoir is drained, the CRV upstream of the trigger valve halts the flow, leading to an increase in the pressure of the system and bursting of the next weakest RBV. A previous study demonstrated sequential delivery of 8 liquids using such a system⁴⁹.

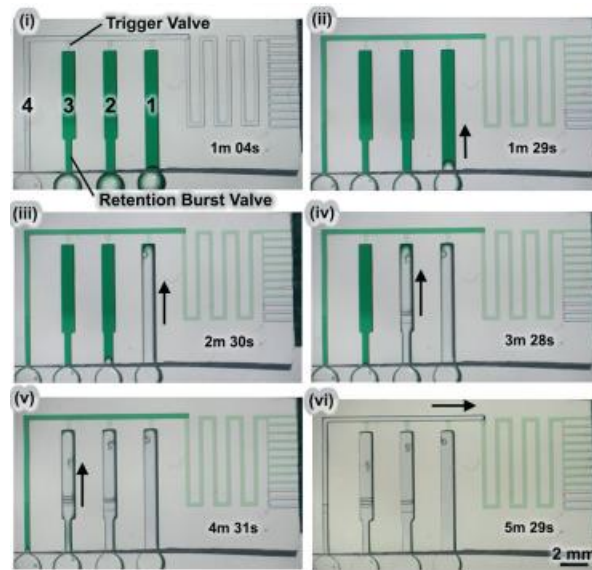


Figure 19. **Sequential delivery actuated by retention burst valves.** Time-lapsed images of sequential delivery in a CC rendered by capillary trigger valves and retention burst valves (RBVs). RBVs drain in the order of capillary pressure in which the weakest RBV (the largest) drains first. Ref.¹⁷

5.1.7.3. Sequential delivery via conditional vents and capillary valves

Another approach for sequential delivery was developed by Conde et al by combining capillary valves and conditional vents. The proposed CC comprised capillary valves connecting multiple inlets to the central channel and conditional vents connecting reservoirs to one another⁴⁰ (Fig. 20). The CC was made of a hydrophobic PDMS and a hydrophilic glass as a covering layer. Therefore, in this case, unlike most CCs that have 3 hydrophilic walls with 1 hydrophobic surface, the hydrophobic property of the microchannels resulted in the spontaneous filling of wider conduits while narrower conduits remained unfilled.

Sequential delivery powered by air bubbles as a spacer was demonstrated by the same group in which the liquids were delivered sequentially based on their distance from the capillary pump⁴². The reliability of air bubble formation as spacers and the sensitivity to user manipulation are the concerns regarding using the proposed chip¹⁷.

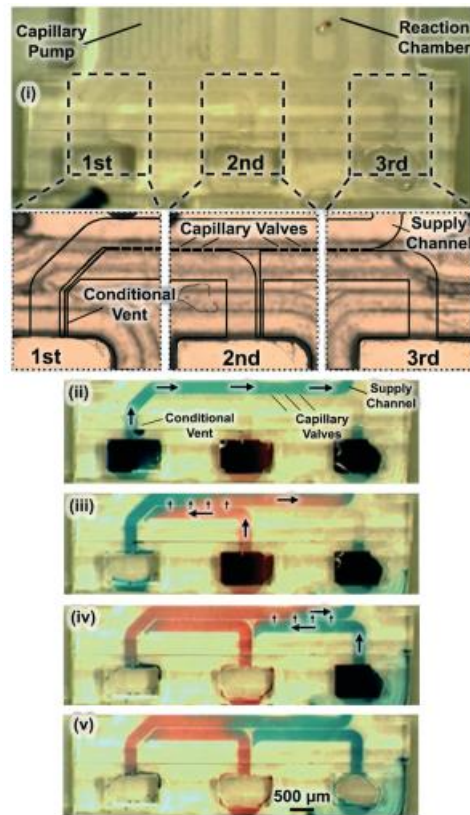


Figure 20. **Sequential delivery with conditional vents and capillary vents.** Sequential delivery enabled via conditional vents and capillary valves. Air vents connected to the microchannel inlet are used to manage sequential delivery. Upon draining of the 1st inlet, the corresponding air vent is opened which allows for the drainage of the 2nd inlet and so on. Ref.¹⁷

5.1.7.4. Sequential delivery via delay valves

Another approach to achieving sequential delivery of liquids is the use of dissolvable films to modulate drainage of multiple reservoirs connected to a single capillary pump. In such a CC, the channel vents needed to be temporarily closed by parafilm to enable the preloading of

the liquids into the parallel reservoirs while simultaneously activating the liquid delivery. After preloading the reservoirs, the user needs to manually remove the parafilm to open the vents and trigger liquid delivery. Sequential delivery of 4 different liquids was achieved using this system and 19 serial valves were used to achieve a delay of up to 11 min (Fig. 21). However, fabrication of delay valves can be tedious as different thin film thicknesses should manually be transferred to the designated locations on the chip to achieve sequential delivery⁹⁰.

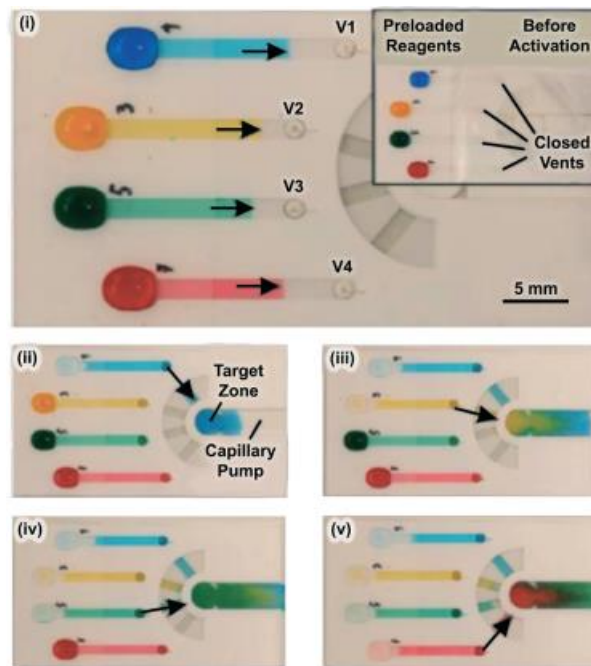


Figure 21. **Sequential delivery actuated via dissolvable barriers.** Dissolvable Polyvinylalcohol (PVA) barriers for sequential delivery. The thickness of the PVA downstream determines the draining of each liquid. Ref.¹⁷

5.1.7.5. Sequential delivery via capillary domino valves

CDVs can be used to realize sequential delivery. To accomplish sequential delivery by CDVs, the MCRs need to be connected serially to one another by CDVs. When the pump is connected, the 1st MCR drains as it has the weakest capillary pressure. Once the 1st MCR is

emptied, the bottom RVB at the 1st CDV drains to expose the air link and the top RBV to the atmospheric pressure and therefore trigger draining of the 2nd MCR and so on (Fig. 22a). Yafia et al. further demonstrated 300 sequential deliveries by chaining 4 CCs and connecting 300 MCRs by 299 CDVs¹² (Fig. 22b).

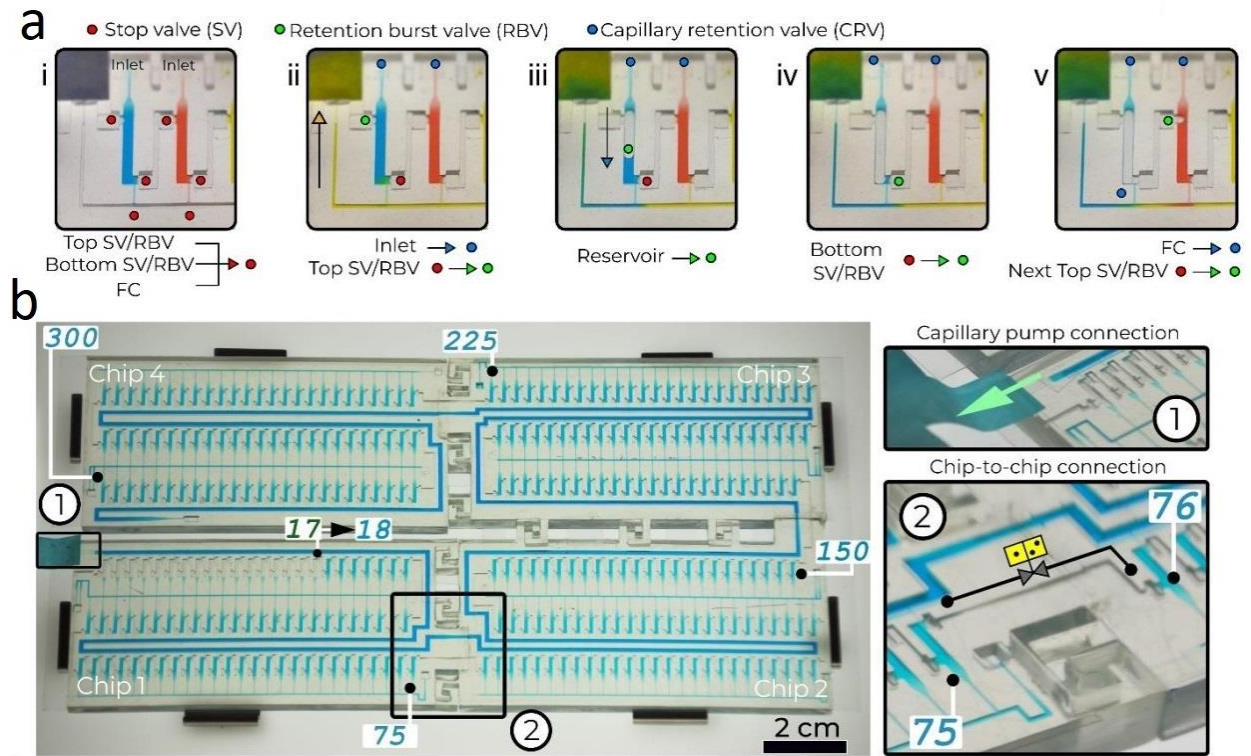


Figure 22. **Sequential delivery by microfluidic chain reaction (MCR) and capillary domino valve (CDV).** (A) No drainage happens when the pump is not connected (i). Once the pump is connected, the 1st MCR starts to drain (ii). When the MCR drains, the bottom RBV at the 1st CDV drains (iv) to open the air link and expose the top RBV to the atmospheric pressure, thereby triggering drainage of the 2nd MCR (v). (b) 300 sequential deliveries by chaining 4 CCs and connecting 300 MCRs with 299 CDVs. Ref.¹²

5.1.8. Applications of capillarc circuits

5.1.8.1. Immunoassays

One of the most common uses of CCs is to automate sandwich immunoassays^{39,43,65,68} (table 1). Table 1 shows representative examples of CCs applications for immunoassay, DNA

hybridization, and DNA amplification. CCs offer several advantages in this regard: (i) Small sample and reagent volume, (ii) precise control over flow, (iii) fully automation and user-friendliness, (iv) compatibility with transparent substrates, which enable fluorescent or chemiluminescent detection and (v) compatibility with micropatterned reaction chambers which enables multiplexing¹⁷.

One-step immunoassays which only require sample addition were first introduced in the form of lateral flow assays, but then, they were also used in microchannel-based microfluidics. Both formats were used widely in the industry and provided successful outcomes. For instance, the Biosite Triage™ chip detects cardiac biomarkers from whole blood samples (Fig. 23)^{64,94}. A blood filter is implemented into the device to extract plasma from the whole blood. The device includes a hydrophobic barrier to control sample incubate time.

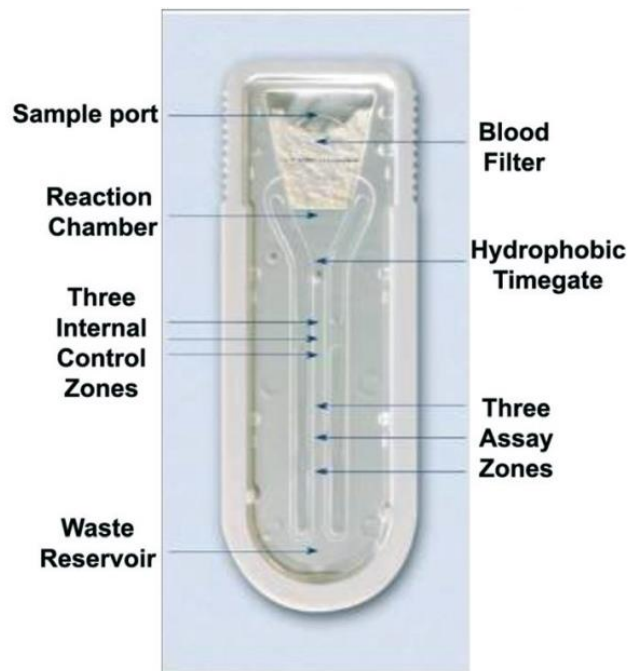


Figure 23. **The Triage™ chip for one-step immunoassay.** The chip uses capillary-driven flow to perform a one-step immunoassay. A blood filter is included to filter whole blood and a hydrophobic time gate is implemented to allow for sample incubation. Ref.¹⁷

In 2008, Delamarche et al developed a microfluidic chip with pre-immobilized reagents to perform a sandwich immunoassay for detection of CRP from 2 μL of plasma in 10 min (Fig. 24). In the next work by the same team, flow mixers were implemented into the CC for effective rehydration of dried reagents which enabled detection of <1 ng/mL of CRP from 5 μL of human serum within 14 min⁹⁵.

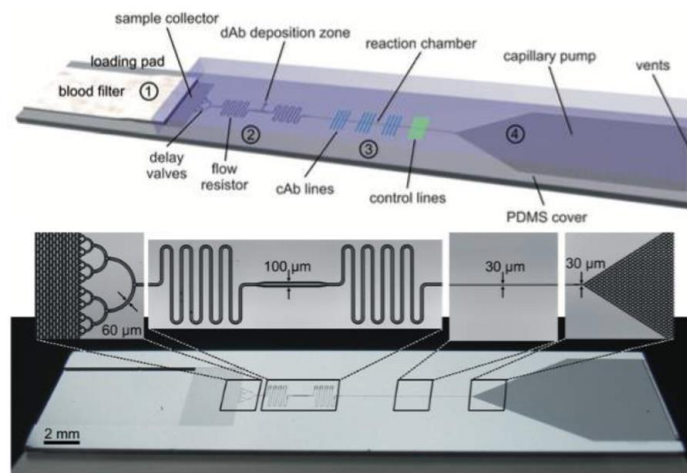


Figure 24. **Microfabricated capillary-driven silicon chip developed by Delamarche et al.⁹⁵ for one-step immunoassay.** The sample introduced to the inlet rehydrates the pre-dried antibodies on its way to the reaction chamber wherein the capture antibodies are patterned. Ref.¹⁷

Recently, the interest in employing CCs to perform multistep liquid delivery has been growing considerably^{17,28}. Such CCs can enable the implementation of additional washing steps or chemical signal amplification steps to improve assay performance^{28,96,97}. Safavieh and Juncker developed a CC with the ability to precisely meter sample and control flow rate which enabled slow flow rate for longer sample incubation time and fast flow rate for rising steps. The proposed CC mainly consisted of multiple trigger valves, a 2nd capillary pump, and 4 RBVs which was able to detect CRP from only 1 μL of the sample within 5 min^{28,96,97}. Olanrewaju et al also developed a CC using the same capillarity elements for urinary tract infection. The CC

enabled 4 sequential delivery steps within 7 min and the assay indicated the limit of detection of 120 CFU/mL⁵¹.

Table 1. Examples of capillary circuit applications for immunoassays, DNA hybridization, and DNA amplification. Selected publications are shown as representative examples.

Application	Target (s)	Sample-to-response time (min)	Multiplexing capability	Automation ability	Ref.
Sandwich immunoassay	C-reactive protein	25	No	Liquid pinning via CRV; sequential delivery; capillary pumping	39
	C-reactive protein	14	No	Sequential delivery; rehydration of reagents; capillary pumping	95
	11 proteins	40	Yes	Sequential delivery; capillary pumping via filter paper	46
	Troponin I	9	No	Sequential delivery; capillary valving; capillary pumping	53
	E. coli	7	No	Sequential delivery; capillary pumping	51
	PfHRP2	Not reported	Yes	Sequential delivery; rehydration of reagents; capillary pumping	98
	Cortisol	20	Yes	Sequential delivery; rehydration of reagents; capillary pumping	99
	S. enteritidis & E. coli		Yes	Capillary burst valves to avoid reagents cross over	100
	Human Chorionic Gonadotropin protein	60	No	Capillary burst valves to avoid reagents cross over	101
	glucose-6-phosphate dehydrogenase & hemoglobin	2	Yes	Uniform reagent reconstitution	102
	SARS-CoV-2 nucleocapsid protein	90	No	Autonomous filling; sequential delivery; capillary pumping	
DNA hybridization	997 bp double-stranded DNA	10	No	Stop and resume of flow via capillary soft valves	86
DNA amplification (RT-PCR)	BNI-1 fragment of SARS cDNA	30	No	Autonomous filling; capillary pumping; autonomous reagent isolation	103

Gosh et al. developed a sandwich immunoassay on a CC, which they call it microchannel capillary flow assay, with integrated lyophilized chemiluminescence reagents for point-of-care detection of malaria. The CC was fabricated from COC by injection molding which made it suitable for mass production purposes. The developed platform could also communicate with a smartphone for data analysis by which the LOD of 8 ng/mL was reported (Fig. 25)⁹⁸.

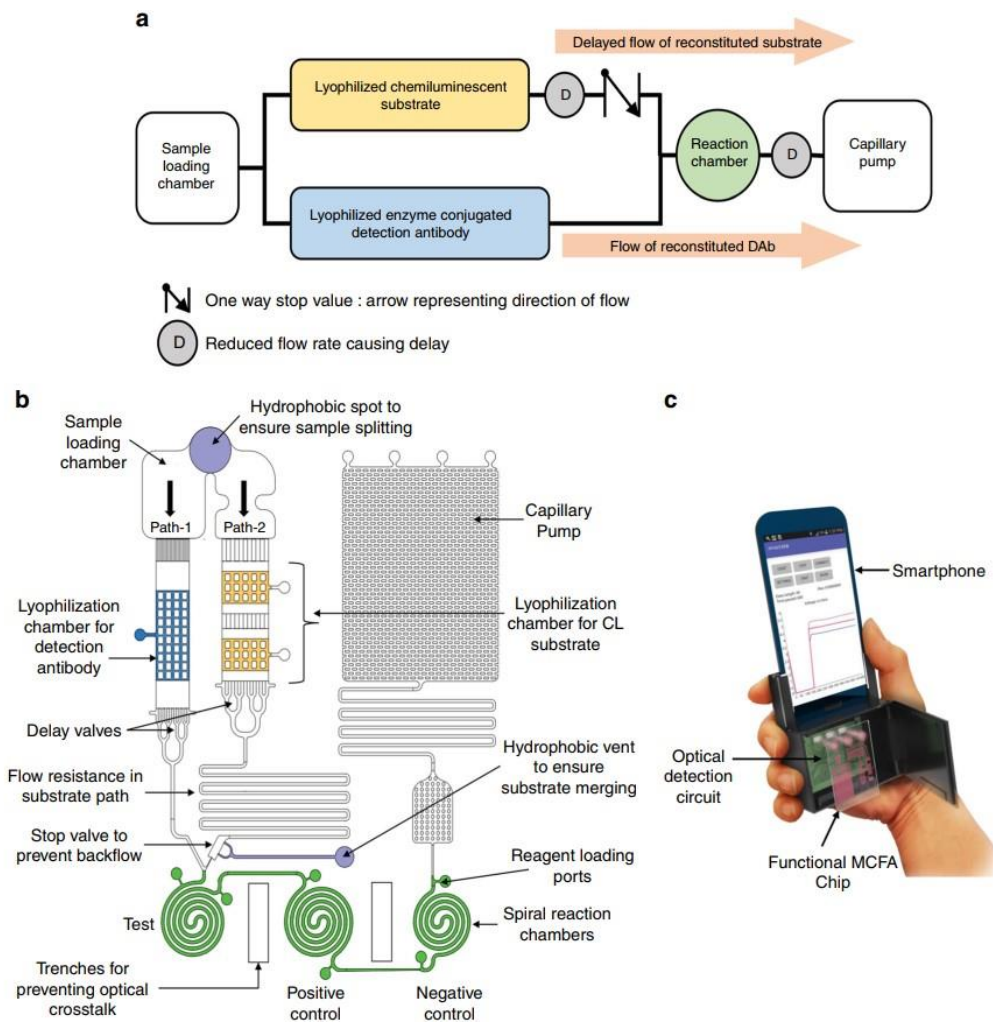


Figure 25. **Layout of the smartphone-based microchannel capillary flow assay developed by Gosh et al⁹⁸.** (a) The working concept of the CC to perform a chemiluminescence sandwich immunoassay. (b) Schematic illustration of the designed CC with implemented capillary elements. (c) Schematic of the developed smartphone-based analyzer. Ref.⁹⁸

In another work, the same group fine-tuned the developed microchannel capillary flow assay for the detection of unbound cortisol in saliva. They developed a fluorescent-based sandwich immunoassay and designed a fluorescent analyzer for quantification by which the assay yielded the dynamic range of 7 pg/mL – 16 ng/mL and a coefficient of variation of ~4% for spiked artificial saliva (Fig. 26)⁹⁹.

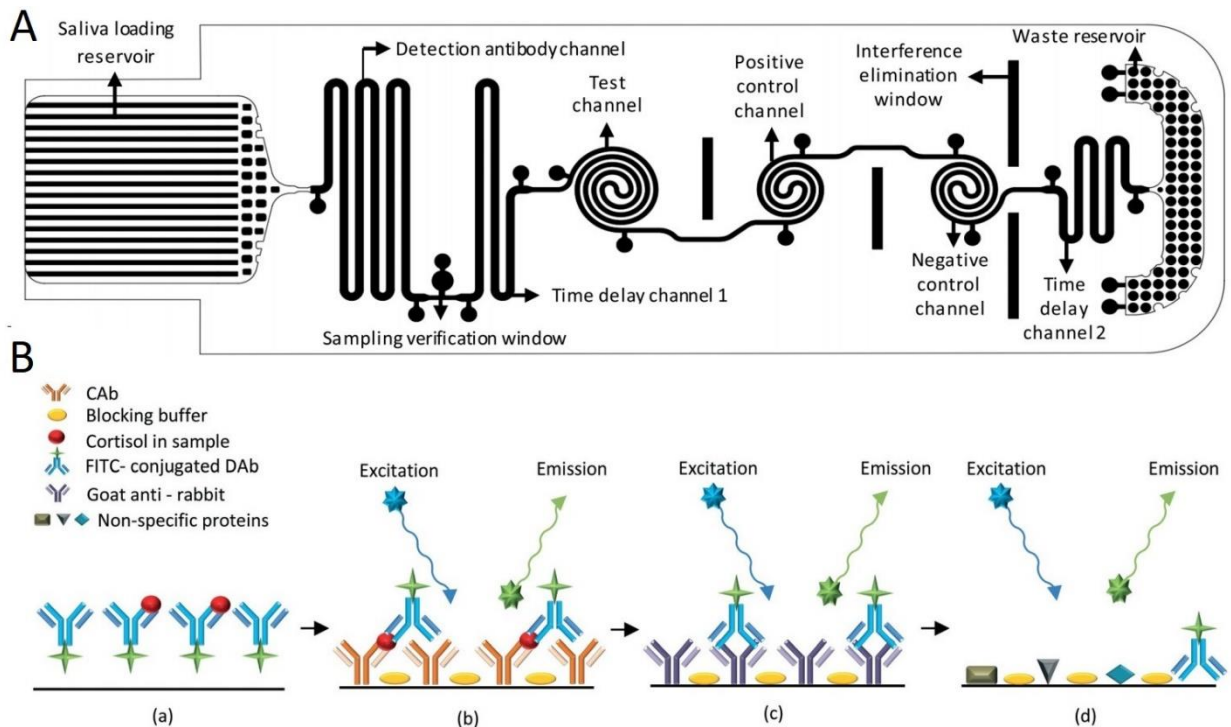


Figure 26. Design of the CC developed by T.U. et al.⁹⁹ and the workflow of the on-chip fluorescent sandwich immunoassay. (A) Schematic illustration of the CC with the implemented capillary elements. (B) Different steps of the on-chip lateral flow immunoassay. a: binding of the target to the reconstituted FITC conjugated detection antibody; b: binding of the target-FITC conjugated detection antibody complex to the capture antibody on the test line; c: binding of the FITC conjugated detection antibody to the goat anti-rabbit antibody on the positive control line, and d: no binding (or non-specific binding) on the negative control line. Ref.⁹⁹

Dogan et al. developed a CC that enabled a fluorescence sandwich immunoassay for the detection of E. coli and S. enteritidis in water (Fig. 27)¹⁰¹. The main capillary elements included the inlet port, outlet port, and capillary burst valves. Sample and reagents needed to be

loaded manually to the chip and the fluorescent measurements were performed by a handheld fluorescent spectrophotometer to render the platform portable and suitable for point-of-care settings. The developed sandwich immunoassay yielded a dynamic range of 101 to 105 CFU/mL for both *S. enteritidis* and *E. coli* and the LOD of 5 and 3 CFU/mL for *S. enteritidis* and *E. coli*, respectively.

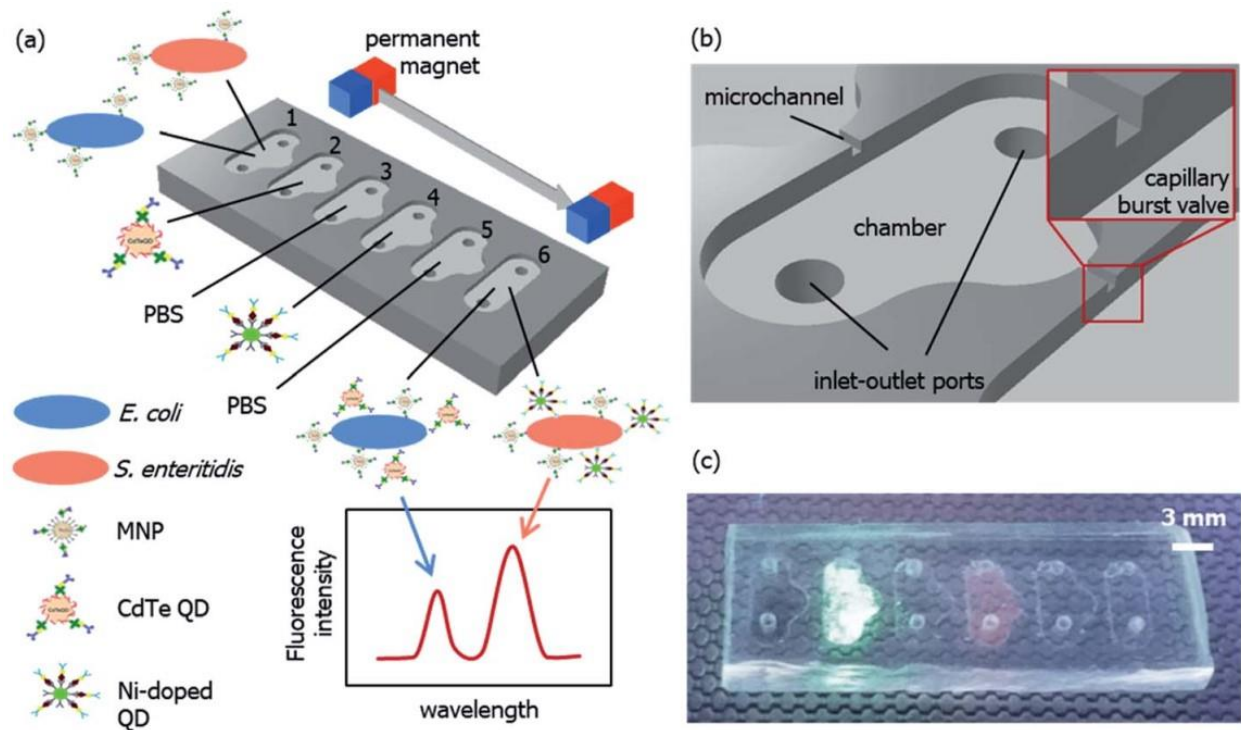


Figure 27. Layout of the CC developed by Dogan et al.¹⁰⁰ for the fluorescence detection of *E. coli* and *S. enteritidis* in water. (a, b) The designed CC and the implemented capillary elements including an inlet port, outlet port, microchannel, and capillary burst valve. (c) The fabricated CC loaded with the sample and reagents. Ref.¹⁰⁰

Ahi et al. developed a CC for the surface-enhanced Raman spectroscopy-based detection of human chorionic gonadotropin (hCG) protein from urine samples (Fig. 28)¹⁰¹. The designed CC included 4 chambers for manual loading of sample and reagents and was implemented

with capillary burst valves to prevent solutions crossover. The developed assay yielded a limit of detection and a limit of quantification of 0.61 and 1.82 IU/L, respectively.

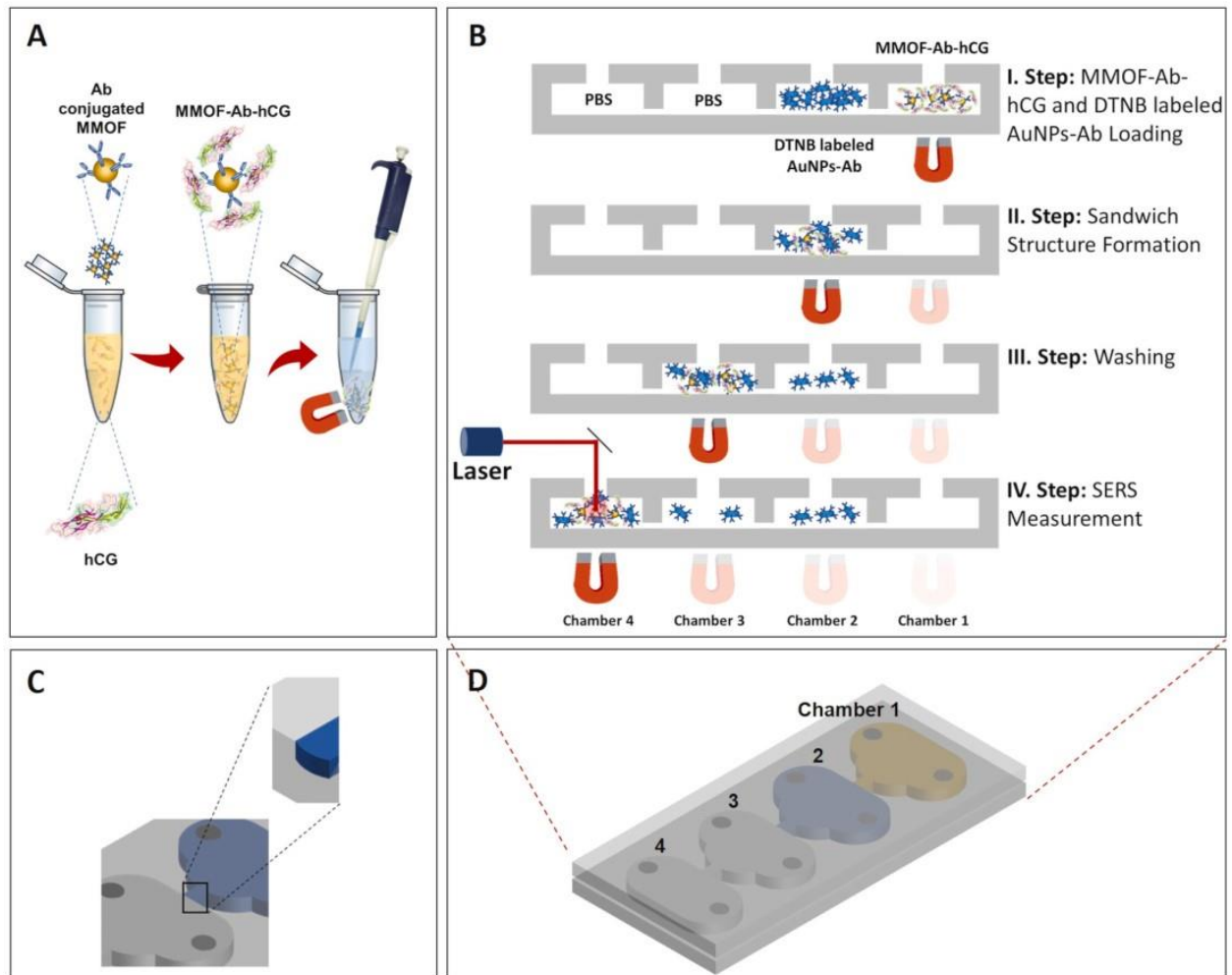


Figure 28. **Microfluidic platform developed by Ahi et al¹⁰¹ for the surface-enhanced Raman spectroscopy-based detection of human chorionic gonadotropin (hCG) protein from a urine sample.** (A) The immune-separation process for extracting hCG from a urine sample. The step-by-step workflow operation of the sandwich immunoassay on the chip. (C) The close-up view of the implemented capillary burst valve for avoiding reagent cross-over and (D) the schematic illustration of the designed chip. Ref.¹⁰¹

Leveraged from the MCR concept, Yafia et al. automated an ELISA protocol on a 3D printed monolithic CC. The CC enabled sequential delivery of sample, reagents, and washing buffer to the reaction chamber without reagents crossover (Fig. 29)¹². The assay generated a light-

insensitive brown precipitate on a nitrocellulose membrane and indicated a limit of detection of 1 ng/mL for SARS-CoV-2 nucleocapsid protein in human saliva.

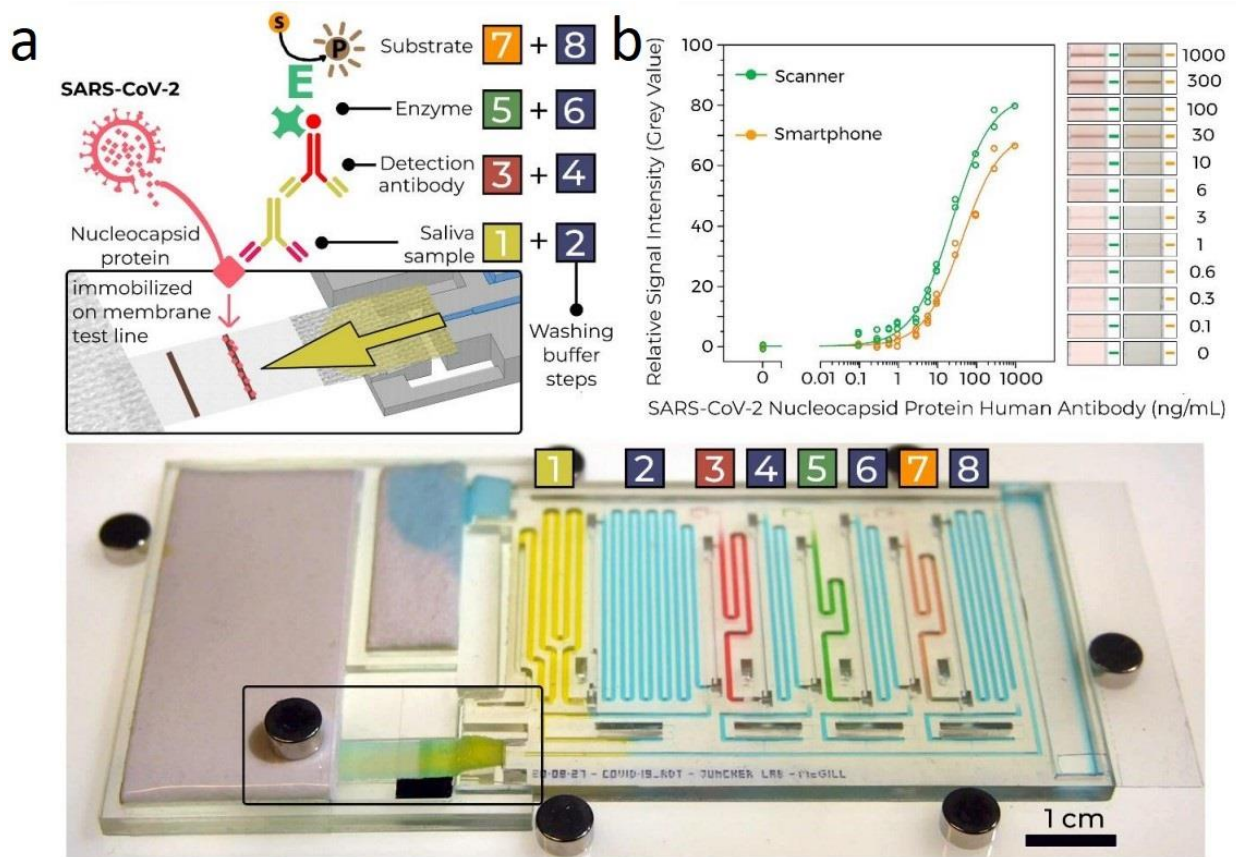


Figure 29. **Automation of ELISA on a capillary circuit (CC) and a COVID-19 antibody test as an application demonstration.** (a) The developed 3D monolithic CC loaded with solution (and colored with food dye). The black rectangle indicated the reaction chamber which consists of a strip of nitrocellulose membrane inkjet spotted with capturing antibody. Following by operation of the CC, a sandwich immunoassay is performed on the reaction chamber. (b) The calibration curve for the nucleocapsid protein spiked in human saliva generated by a scanner as well as a smartphone. Ref.¹²

5.1.8.2. Capillary circuits for DNA analysis

CCs comprising loading pads, reagent deposition regions, patterned reaction chambers, capillary soft valves, and capillary pump were developed to perform DNA hybridization⁸⁶. Reagents were pre-dried in the reagent deposition zones and double-stranded DNA was amplified from the off-chip polymerase chain reaction (PCR) was added to the chip to

reconstitute dried reagents and stop at the capillary soft valve. Next, the DNA was processed, and the capillary soft valve was manually actuated to deliver the solution to the reaction chamber (table 1).

CCs can also be used to perform on-chip DNA amplification by PCR¹⁰³⁻¹⁰⁵. PCR requires 3 heating steps which were carried out either with a Pletier heater underneath the chip or with a thin film heater integrated onto the chip^{103,104}. To date, most CCs for DNA amplifications were fabricated via hydrophobic materials such as PDMS or cyclic olefin copolymer (COC). One alternative to surface treatment is the use of surfactant to lower the liquid surface tension and contact angle, enabling capillary-driven flow in the CC^{103,105} (table 1). Numerical models were developed to investigate the effect of surfactant addition and heating on the fluidic performance of PCR mixture¹⁰⁶ in a chip¹⁰⁴.

CCs for DNA applications were developed to detect 12 DNA sequences indicative of liver cancer¹⁰³. Most of the CC designs for PCR were only limited to a relatively simple microchannel and so far, were not implemented with multiple capillarie elements to perform more advanced liquid handling operations. Regarding PCR-on-chip, the challenges that need to be addressed are mainly bubble formation, change in the contact angle, condensation due to heating, and the cycles of heating and cooling which may result in malfunctioning of the CC¹⁷.

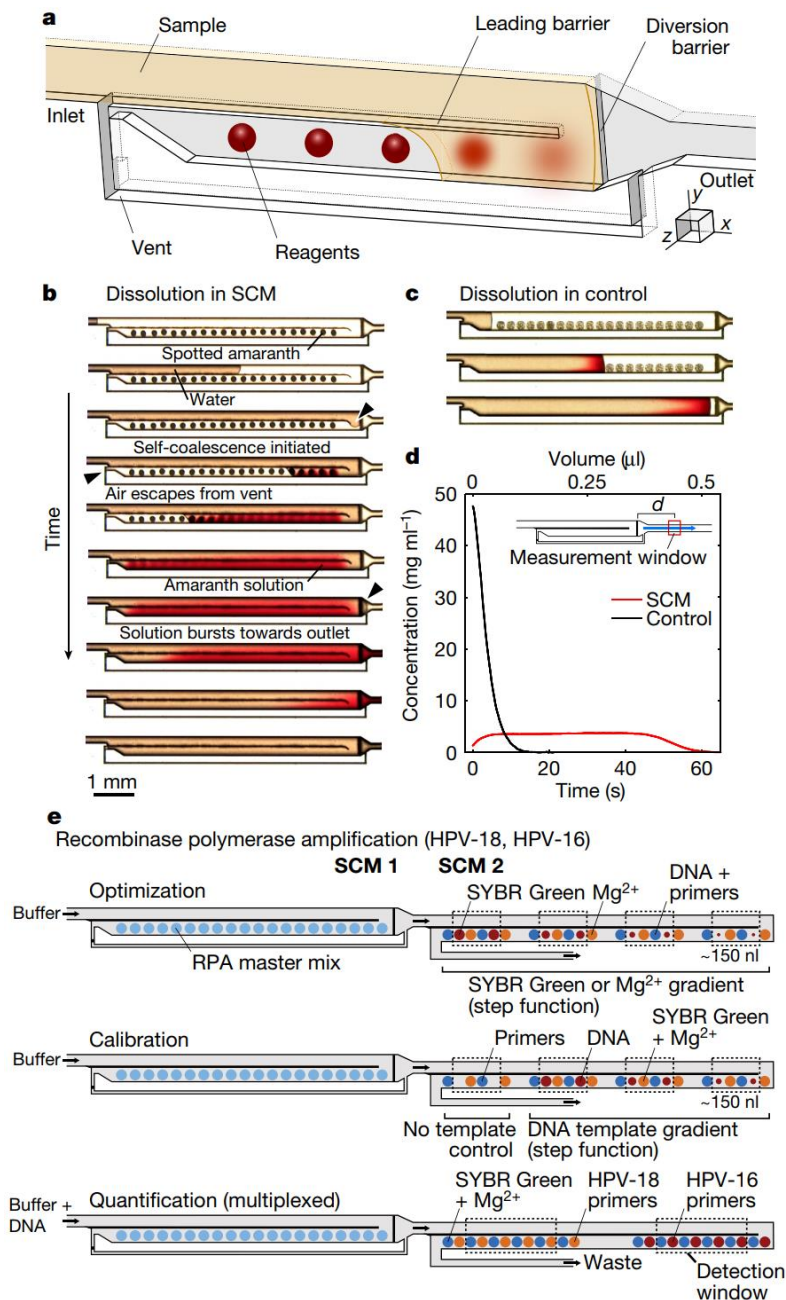


Figure 30. Self-coalescence module (SOM) developed by Gökçe et al¹⁰⁷ for reagent rehydration and recombinase polymerase reaction (RPA) as a demonstration of the application. (a) The schematic illustration of the SOM. (b) The time series bright-field microscope images of SOM during reconstitution of pre-dried amaranth with water over the course of 75 s. (c) Reconstitution of amaranth in a control channel (without SOM). (d) The concentration profiles of amaranth solution at the indicated measurement window (3 mm downstream of the SOM outlet) for a 375-nL SOM and 375-nL control microchannel. (e) Combination of 2 SOMs to perform RPA where the 1st SOM contains RPA mater mix and the 2nd RPA contains rest of the reagents. RPA reaction kinetics can be characterized by measuring fluorecence intensity over the SYBR Green, Mg²⁺ (optimization), and DNA template (calibration) concentration gradients. Depositing primers of different DNA temples in separate regions of 2nd SOM enables multiplex quantification of DNA concentration. Ref.¹⁰⁷.

Like PCR-on-chip, CCs can also be employed to perform recombinase polymerase amplification (RPA). Gökçe et al developed a fully passive CCs mainly comprising a self-coalescence (SOM) module for effective and uniform rehydration of dried reagents within a CC (Fig. 30). As a proof-of-concept, they implemented RPA on a CC with 2 SOMs for drying and subsequent rehydration of the RPA-related reagents to detect DNA sequences of human papilloma virus (HPV) types 16 and 18¹⁰⁷.

In another work by the same group, Rocca et al. fine-tuned the SOM to perform quantitative glucose-6-phosphate dehydrogenase (G6PD) test and hemoglobin measurement in 2 minutes using less than 2 μL of whole blood sample¹⁰². Fig. 31 shows the assay workflow and the developed microfluidic chip.

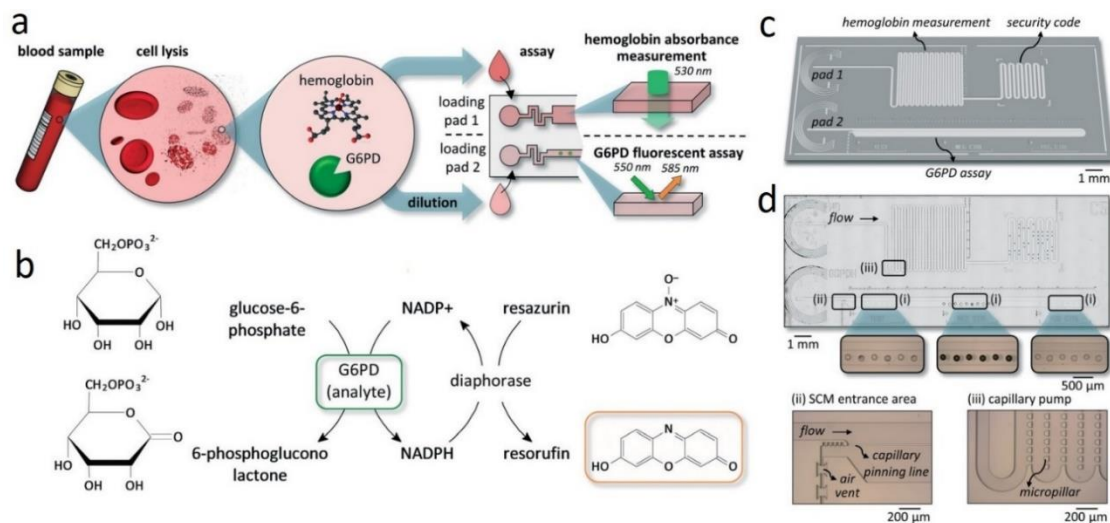


Figure 31. Assay workflow and the capillary-driven microfluidic chip developed by Rocca et al.¹⁰² for determining G6PD activity and hemoglobin concentration from whole blood. (a) Whole blood is lysed to release hemoglobin and G6PD. First, the lysate is loaded to the first loading pad of the circuit to measure the concentration of hemoglobin. The rest of the lysate is then diluted with buffer and loaded into the second loading pad for the fluorescent measurement of G6PD activity. (b) A coupled enzymatic reaction is used for measuring the G6PD activity in which resazurin is reduced to fluorescent product resorufin. (c) 3D render of the developed capillary-driven microfluidic chip. (d) Real images of the chip microfabricated from glass and integrated with dried reagents for the G6PD assay. (i) depicts the area the reagents are spotted. (ii) shows the entrance of the SOM, and (iii)

illustrates the capillary active region occupied by the micropillars for hemoglobin measurement. Ref.¹⁰²

5.1.9. Capillarie circuits for monitoring medical adherence

Medication adherence refers to whether patients take their drugs as directed (e.g., twice daily) and whether they continue to take a medication after it has been given. Medication adherence is a medical and cultural problem across the world, with over half of patients failing to follow their prescriptions¹⁰⁸. World health organization (WHO) reported that adherence to medication could even have more beneficial effects than developing new treatments on the overall population health¹⁰⁹. Capillary microfluidics and capillarie circuits have promising potential in developing rapid, simple, and user-friendly medical adherence kits¹¹⁰. Fig. 32 depicts the overall layout of an ideal capillary-driven medication adherence kit.

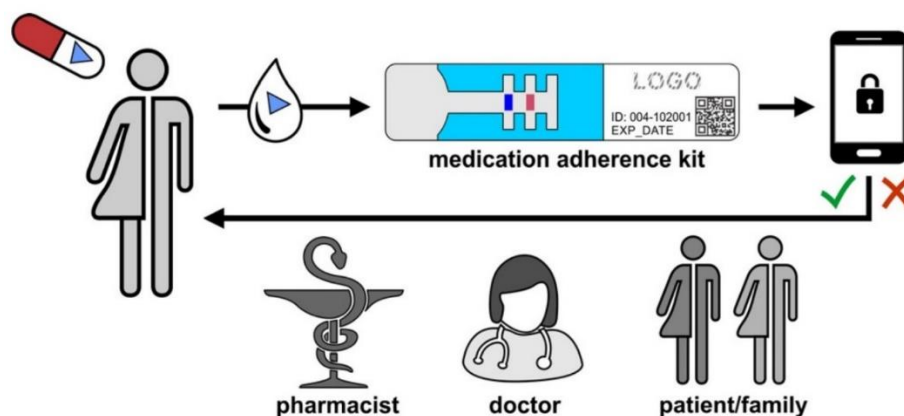


Figure 32. **Capillary microfluidics for improving medication adherence.** A simple, user-friendly capillary-driven medication adherence kit can take body fluid sample, e.g., saliva, urine, etc., to indicate that a certain medication has been taken by the patient and share this information with an appropriate end, e.g., doctor, pharmacist, etc. Ref.¹¹⁰

The field of capillary microfluidics in medication adherence is relatively young and full of potential for progress in the near future. One notable example of this is the Medimate Manilab[®] cartridge developed by Staal et al^{110,111}. The device basically includes a capillary

microchannel implemented with electrodes for electrophoresis to detect lithium, which is an active pharmacological component in a variety of psychiatric medications (Fig. 33).

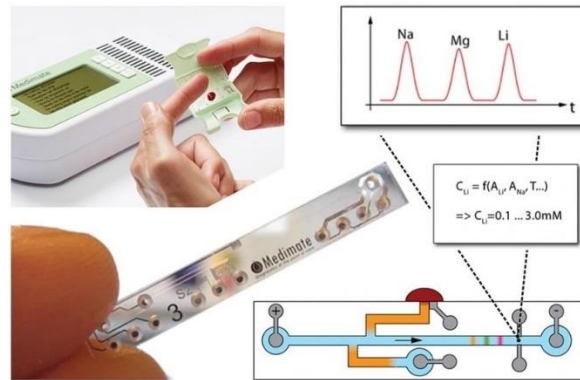


Figure 33. **The Medimate Manilab® cartridge for the detection of lithium from whole blood samples.** The device consists of a capillary microfluidic channel which is implemented with electrodes for electrophoresis and the detection of lithium. Ref.¹¹⁰

5.1.10. Capillary-assisted microfluidic devices

The capillary phenomenon can also be used in conjunction with other sources of flow induction such as gravity or electronics to execute various liquid handling tasks^{112,113}. For instance, Arango et al. implemented electro-actuated valves in a capillary microfluidic device to realize advanced liquid manipulation (e.g. stop and resume flow, sequential flow of multiple liquids, and liquid detection via capacitance measurement) by sending commands from a smartphone (Fig. 34)¹¹³.

Haghighy et al. employed capillary and gravitational forces to develop a microfluidic device integrated with an electrochemical sensor for point-of-care quantification of proteins (Fig. 35)¹¹². As a demonstration of the application, they performed a COVID-19 antigen assay for the detection of nucleocapsid protein SARS-CoV-2 spiked in plasma within 15 min. The assay indicated a dynamic range of 10 – 1000 pg/mL with a limit of detection of 3.1 pg/mL.

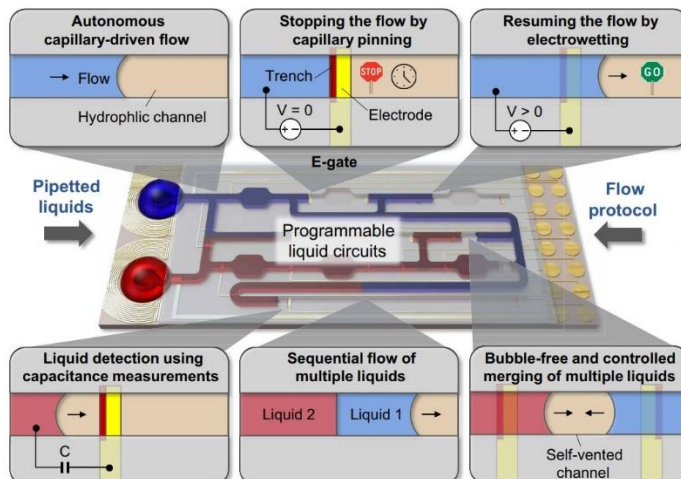


Figure 34. **Electro-actuated valves implemented in a capillary-driven microfluidic chip to execute advanced liquid handling tasks.** Electrically actuated microfluidic gates (called e-gates) are implemented in a capillary-driven microfluidic chip and the commands are sent to the circuit via a smartphone to realize various liquid operations. Using the developed platform, the liquid can be stopped and resumed at an e-gate; liquid detection is possible via capacitance measurement; liquids can be delivered sequentially at any order and combination, and liquids can be merged without bubble creation. Ref.¹¹³

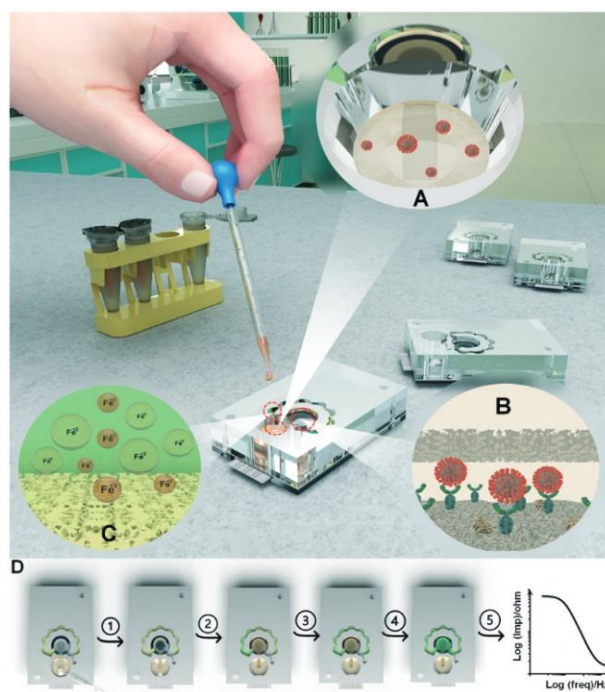


Figure 35. **Different compartments of the capillary- and gravity-assisted microfluidic chip to perform an electrochemical assay developed by Haghayegh et al¹¹².** (A) Inlet of the developed microfluidic chip where the sample is loaded. (B) The target molecule reaching the reaction chamber and interacting with the capture antibody. (C) Diffusion of the Fe^{2+} and Fe^{3+} into the sample for preparing

the redox solution. (D) The workflow of the whole on-chip assay: Sample loading into the chip for capillary- and gravity-assisted delivery of the sample to the working electrode (1); sample covering the reaction chamber and flowing into the redox channel (2); Reconstitution of the redox reagents by the sample (3); diffusion-based delivery of the redox solution to the reaction chamber (4); and signal measurement via electrochemical impedance spectroscopy (5). Ref.¹¹²

5.1.11. Rapid prototyping of capillarc circuits

Rapid prototyping of CCs is another emerging area of research. As mentioned before, fabrication of CCs has mostly been done via photolithography in cleanroom^{39,42,68} partly because it was believed that capillarc elements, such as stop valves and trigger valves, require high resolution ($\sim 10 \mu\text{m}$ feature size) and smooth surfaces (\sim submicron) for proper function. Recently, there have been demonstrations of rapid-prototyped CCs with functionalized capillarc elements^{28,51}. In this section, we briefly describe the main rapid prototyping techniques for the fabrication of CCs, i.e. Xurography, laser cutting, and 3D printing, in the 3rd wave of CCs development.

5.1.11.1. Xurography (razor writing)

Xurography is an inexpensive fabrication technique in which a plotter fit with a knife (or scalpel) is used to create a pattern in polymers. Xurography can reach a resolution of $\sim 10 \mu\text{m}$ ¹¹⁴ and has been used for the fabrication of molds to be replicated by PDMS for capillary-driven flow⁵². Xurography was also employed to cut hydrophilic polymers and spacers which upon implementation with dissolvable polymer films, CCs for preprogrammed liquid delivery were developed⁹⁰. Xurography is inexpensive and accessible, but yet requires a lot of manual operations which has limited its use to fabricate only relatively simple microchannels¹⁷.

5.1.11.2. Laser cutting

Laser cutting has recently been employed to fabricate CCs with various capillaric elements such as capillary pumps, timing channels, and trigger valves⁵³ (Fig. 36A). Using laser cutting, fabrication of CCs from PMMA is feasible within 30 min – 3 h. Two-level trigger valves with different geometries were fabricated using laser cutting and their reliability and functionality were investigated^{115,116}. The minimum feature size achievable via laser cutting is 150 μm with smaller features having a more triangular Gaussian profile due to the shape of the laser beam (Fig. 36B). These limitations can be overcome by using femtosecond lasers and different optics to achieve $\sim 1 \mu\text{m}$ resolution, and beam shaper technology to prevent triangular microchannel shape¹¹⁷.

5.1.11.3. 3D printing

Recently, there has been a growing interest in using 3D printing for fabricating microfluidic devices from polymer resins^{118–120}. The practical minimum feature size via 3D printing is 100 μm and the surface roughness can approach $\sim 10 \mu\text{m}$ which yields in deviation from predicted dynamics of capillary-driven flow in open microchannels¹²¹. With a state-of-the-art stereolithography 3D printer, the surface roughness of $\sim \pm 1 \mu\text{m}$ is feasible^{49,122}.

3D printed capillaric elements are much larger and rougher than those fabricated via cleanroom fabrication techniques (Fig. 36C, D). The functionality of capillaric elements replicated from 3D printed molds (fabricated in < 30 min) has been investigated and trigger valves with a geometry up to 80-fold larger than those of cleanroom-fabricated ones functioned properly⁴⁹. Using 3D printing, fabrication of RBVs with different heights and widths to achieve sequential delivery of up to 8 liquids is achievable⁴⁹. 3D printing also

enables the fabrication of millimeter-scale conduits (e.g. $13 \times 4 \times 2 \text{ m}^3$) with a large capacity ($\sim 100 \mu\text{L}$) which can be useful for the application that needs large volumes for sample processing⁵¹ (Fig. 36D).

Yet concerns regarding the resolution of 3D printed CCs remain. The minimum feature size of $\sim 100 \mu\text{m}$ ⁵⁴ can limit the highest capillary pressure obtained in a 3D printed CC and may limit the usage of 3D printing in applications that typically need $\sim 10 \mu\text{m}$ feature sizes such as cell or microbead trapping.

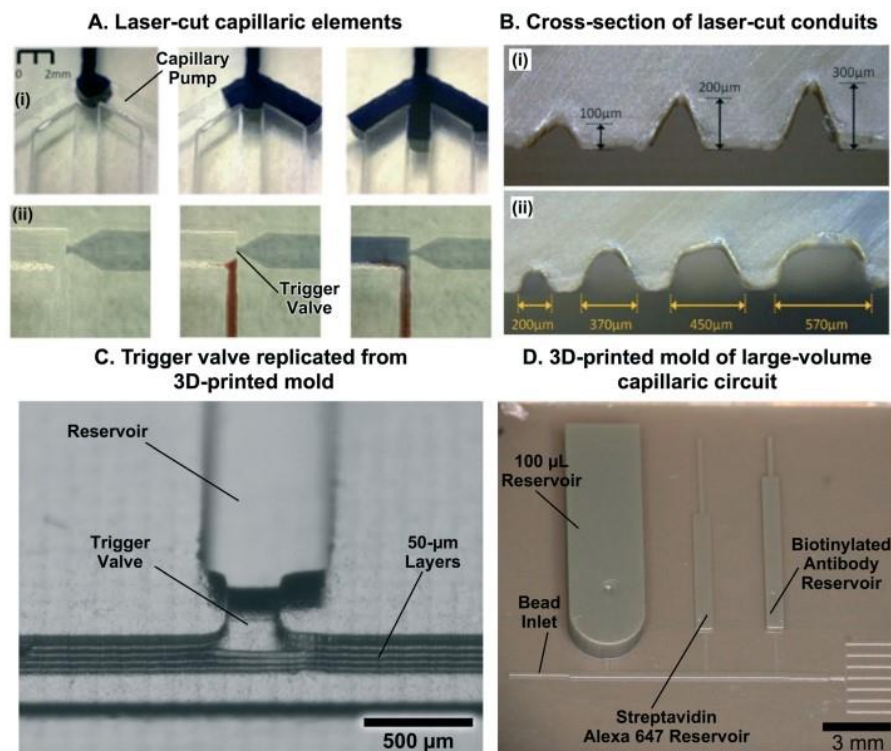


Figure 36. **Rapid prototyping of capillary circuits (CCs) fabricated via CO₂ laser cutting and 3D printing.** (A) Capillary pump and trigger valves fabricated via CO₂ laser cutting. (B) The cross-section of a microchannel fabricated by laser cutting. Smaller microchannels take on a triangular Gaussian profile, due to the repeated scanning of the laser beam, while the microchannels have a more triangular shape. (C) Scanning electron microscopy image of a two-level trigger valve fabricated via 3D printing. (D) 3D printed mold, to be replicated by PDMS, for fabricating a CC with various capillary elements, such as inlets, two-level trigger valves, retention burst valves, and a capillary pump, to detect *E. coli* in synthetic urine samples. (A-D) Ref.¹⁷

5.1.12. Conclusions and future outlook

Herein, we discussed capillary-driven flow in microchannels within the frame of circuits that consist of different capillarie elements. We traced the history of CCs in terms of fabrication techniques and pointed to the 3 main waves of developments in this regard. Then, we discussed the fundamental physical laws that govern capillary-driven flow in microchannels and explained different capillarie elements developed so far to perform various liquid handling tasks. We next highlighted the different strategies for integration of capillarie elements to perform preprogrammed liquid handling operations with minimal user intervention. We then pointed to the notable applications of CCs in diagnostics and medication adherence, integration of CCs with other types of microfluidics as well as recent progress in rapid prototyping of CCs. With the recent growing interests in the use of rapid prototyping, notably 3D printing, it is envisioned that capillary microfluidics is on the edge of the 3rd wave of development that provides better accessibility, affordability, and applicability. 3D printed CCs outperform paper-based microfluidic devices in terms of control overflow, fabrication speed, and cost-efficiency. The digital and standardized “STL” file format of 3D printing would allow easy sharing of files and designs in online databases and it is envisioned that in the future CCs could be designed and customized as readily as electrical circuits¹⁷.

5.2. SARS-CoV-2 and COVID-19 diagnostics

5.2.1. Introduction

The need for diagnostic tests for population management is now clearer than before with the current coronavirus disease 2019 (COVID-19) pandemic. At the beginning of the pandemic, several countries, including South Korea, Germany, and the United States, rapidly validated and utilized diagnostic tests for examining people^{123,124}. An extensive number of such tests rapidly obtained the emergency use authorization (EUA) from US food and drug administration (FDA), and many antibody-based tests, which do not need FDA clearance, became available in the market^{125,126}. However, the performance of diagnostic tests varies considerably, yielding confusing results¹²⁷. In this section, we explain the working principles of major diagnostic tests, i.e. molecular tests and immunoassays, report their analytical performance, explain their potential limitations, and point to their initial performance at the clinical trial. In the end, we provide a comparison regarding different sample specimens for COVID-19 diagnosis.

5.2.2. COVID-19 etiology

COVID-19 is the disease caused by severe acute respiratory syndrome coronavirus 2 (SARS-CoV-2) which belongs to the beta family of coronaviruses. The virus is constructed by a lipid bilayer wherein spike (s) protein, membrane (M) protein and envelop (E) protein can be found. Inside the virus, there exists a ribonucleoprotein (RNP) which is basically a single-stranded RNA (28.9 kb) covered by nucleocapsid (N) protein. SARS-CoV-2 binds to the angiotensin-converting enzyme 2 (ACE2) receptor of lung cells via its S protein (Fig. 37)^{128,129}.

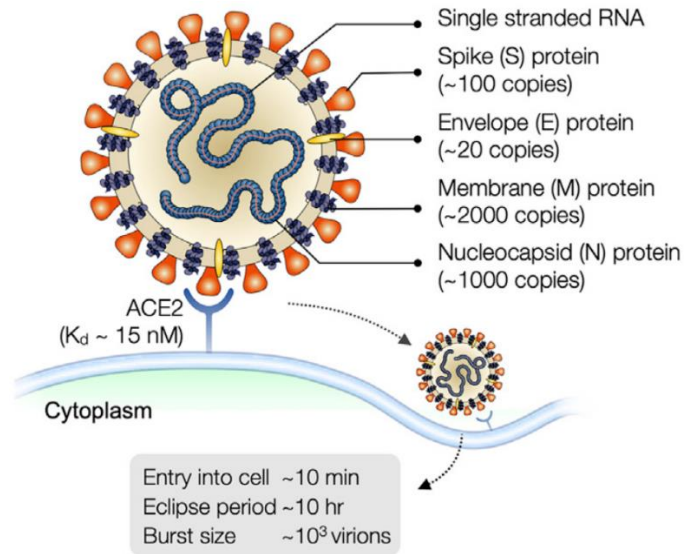


Figure 37. **The structure of SARS-CoV-2.** The virus is enveloped and spherical with a diameter of 120 nm. Membrane (M), envelope (E), and spike (S) proteins are present on the surface of the virus. Inside the virus, there exists a single-stranded RNA covered with nucleocapsid (N) protein. The virus enters host cells through angiotensin-converting enzyme 2 (ACE2) on the cell surface. It is important to note that a recent study investigated the structure and distribution of S proteins on intact SARS-CoV-2 virions and reported the number of S proteins to be ~ 25 per virion¹³⁰ (instead of 100 which is shown in the figure). Ref.¹²⁹.

5.2.3. Nucleic acid amplification tests

Nucleic acid amplification tests (NAATs) for diagnosis of COVID-19 detect the RNA viral sequences of N, E, S, or RNA-dependent RNA polymerase (RdRp) genes. The NAATs offer high accuracy and after transporting the samples to the laboratory, the results can be obtained within hours with the LOD of down to $0.02 \text{ copy}/\mu\text{L}$ ¹³¹. Various NAATs are available for COVID-19 diagnosis.

5.2.3.1. COVID-19 RT-PCR test

RT-PCR is the current gold standard method for COVID-19 diagnosis. In RT-PCR, first, the RNA from the clinical sample needs to be extracted. The extracted RNA is then mixed with reagents, i.e. target gene primer, probes, and RT-PCR master mix, and amplified. Depending

on the design of the probe, the product of PCR can be detected during or after the amplification process¹³².

The analytical performance of RT-PCR is highly dependent on the primer design. Since there exists a high similarity between different species of coronavirus, especially between SARS-CoV and SAR-CoV-2, identification of unique gene sequences is essential to eliminate cross reactivity¹²⁹. RT-PCR provides high accuracy (LOD: ~0.14 copy/mL) and throughput as multiple assays can be performed in parallel^{129,133}. RT-PCR tests are typically carried out in centralized laboratories due to the need for special equipment, trained personnel, and strict contamination control. Proper sample transfer and securing reagents are important in minimizing assay turnaround time, and proper sample processing is also a key factor in reducing false-negative results^{134,135}.

PCR tests have also been adapted to be used at the point of need. One example of this is the lab-free, point-of-care test for SARS-CoV-2 (COVIDNudge) developed by Gibani et al. As illustrated in Fig. 38, the device mainly comprised a cartridge in which the reagents and samples (nasopharyngeal swabs (NPS)) are loaded into, and a processing unit called NudgeBox for performing the PCR. In a clinical trial with patient samples, the test indicated overall sensitivity of 94% and specificity of 100% (compared to conventional PCR) with a run-time of ~60 – 90 min ¹³⁶.

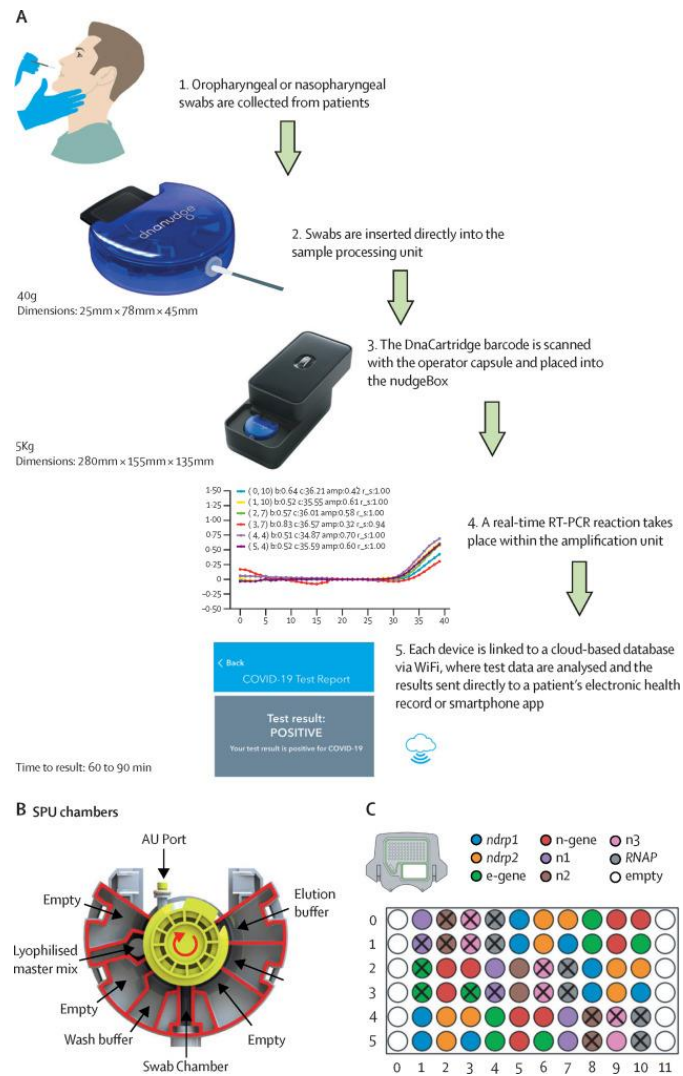


Figure 38. **Point-of-care COVID-19 diagnostic device developed by Gibani et al¹³⁶.** (A) The oropharyngeal or nasopharyngeal swab is collected from a patient and inserted into the DnaCartridge, followed by insertion of the cartridge into the NudgeBox to perform RT-PCR. The device can send the data to the patient's electronic health record or cell phone app. (B) and (C). The schematic of the components of DnaCartridge: Sample preparation unit (SPU) and amplification unit (AU). Ref.¹³⁶.

5.2.3.2. Digital PCR-based SARS-CoV-2 detection

With digital PCR, absolute quantification of the target nucleic acid is possible. In this technique, samples are partitioned into a large number of small reaction volumes to ensure that each partition contains a few or no sequence¹³⁷. Among various methods of partitioning, e.g. microwell plates, capillaries, oil emulsion, and miniaturized chambers, digital droplet PCR

(ddPCR) is the most common one¹³⁸. ddPCR offers higher analytical sensitivity (LOD: $\sim 10^{-2}$ copy/ μ L) compared to conventional PCR, thereby enabling it to detect very low viral loads¹²⁹.

5.2.3.3. COVID-19 NAATs based on isothermal amplification

Isothermal amplifications enabled the implantation of COVID-19 NAATs at the point-of-need, providing fast results without the need for laboratory equipment^{139,140}. Such an amplification method uses specific DNA polymerases, which enables the amplification to happen at a fixed temperature. Isothermal amplification methods offer comparable analytical performance to that of conventional PCR with a shorter assay time (less than 1 h)¹²⁹.

5.2.3.3.1. Loop-mediated isothermal amplification

Loop-mediated isothermal amplification (LAMP) utilizes 4-6 primers for recognizing 4-6 distinct regions of the genome for a highly specific amplification test. During the reaction, the pairs of primers create a dumbbell-like DNA structure, subsequently acting as the LAMP initiator (Fig. 39A)¹⁴¹. A key challenge in developing LAMP assays for COVID-19 diagnosis is designing the primer set as multiple pairs of primers need to be selected for a target DNA and the working temperature of these primers should match the optimum working temperature of DNA polymerase¹⁴². Several studies designed primer sets for targeting mainly N¹⁴³ and open reading frame 1 (ORF1)¹⁴⁰ genes with the typical assay time of ~ 1 hr and LOD of ~ 10 copy/mL (Fig. 39B).

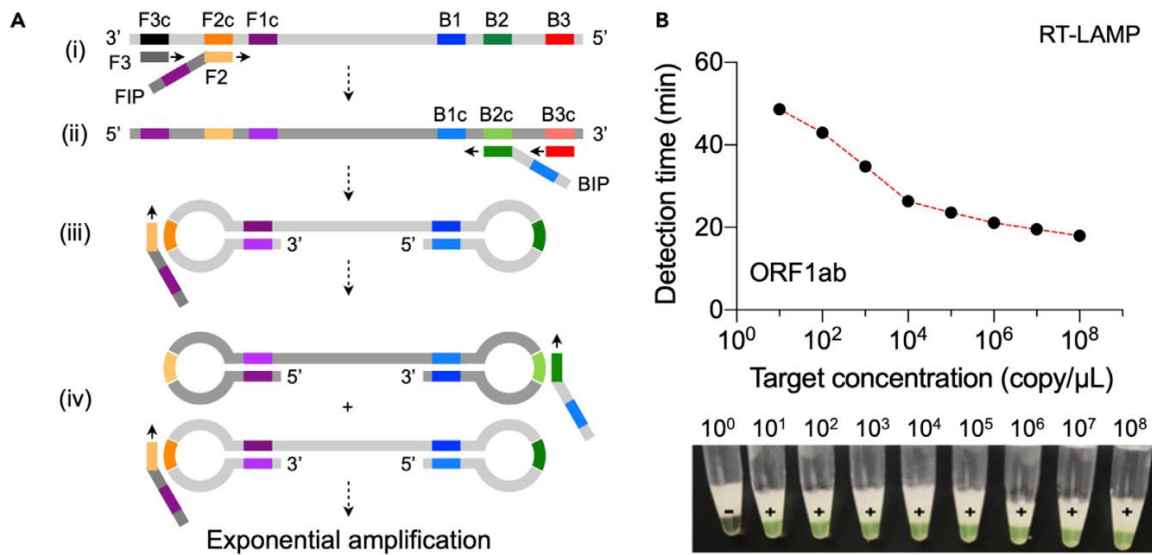


Figure 39. **An example of a LAMP-based covid-19 test.** (A) LAMP mechanism. LAMP uses 4-6 (6 in this example) primers recognizing 4-6 regions of the target genome. A strand-displacing DNA polymerase initiates the synthesis process and 2 of the primers form a loop structure to facilitate subsequent rounds of amplification via an extension on the loop and additional annealing of the primers. (B) RT-LAMP for detection of ORF1ab gene. The amplification process was monitored via turbidimeter readings or visual observation of calcein-mediated color change from orange to green. The target concentration is inversely related to the detection time as well as the color change. Ref.¹²⁹

5.2.3.3.2. Nicking endonuclease amplification reaction

Nicking endonuclease amplification reaction (NEAR) is an isothermal amplification method, especially for short oligonucleotides, that are directly generated from the target nucleic acid¹⁴⁴. In this technique, a set of target primers called nicking endonuclease and strand-displacement DNA polymerase are utilized for isothermal unwinding and subsequent amplification of the target fragment¹⁴⁵. The workflow mechanism of the NEAR technique is shown in Fig. 40A. One drawback of the NEAR technique is the generation of a large number of non-specific products which can limit the detection sensitivity. Optimizing the reaction condition can assist in mitigating this issue¹⁴⁴.

Abbot developed a compact, integrated COVID-19 diagnostic test based on the NEAR technique called ID NOW (FDA-EUA approved) (Fig. 40B). The system includes a user-friendly

sample processing cartridge with a total hands-on time of 2 min and a total assay time of <15 min. The assay targets the RdRp region of the SARS-CoV-2 genome (LOD of 0.125 copy/ μ L).

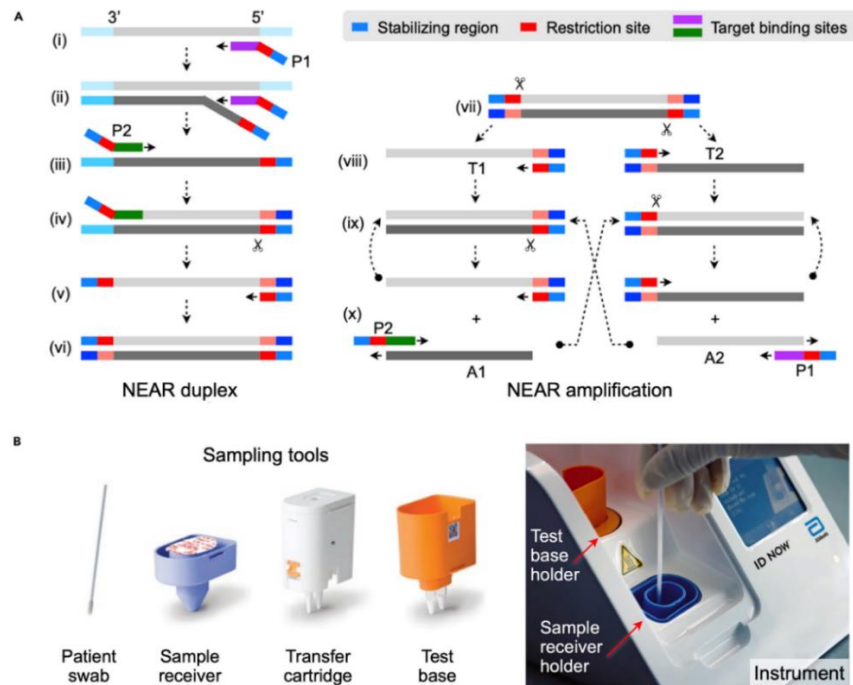


Figure 40. **An example of NEAR-based COVID-19 test.** (A) NEAR duplex formation (right) and amplification (left). (i) the reverse primer (P₁) binds to the target and extends, followed by (ii) binding and extending of a 2nd P₁, and subsequently displacing the 1st P₁. (iii) The primer P₂ binds to the released strand and extends to create a double-strand nicking enzyme recognition site wherein (iv) the nicking enzyme (illustrated by a scissor) can bind and nick downstream of the recognition site. (v) Polymerase generates the complementary part of the cleaved section, (vi) the final product having a double-stranded DNA with restriction sites at both ends. (vii) Nicking enzyme generates 2 templates of T₁ and T₂ through binding and nicking the NEAR duplex, (viii) followed by extension of the free parts of the T₁ and T₂ templates. (ix) Repeated nicking and polymerization steps take place. (x) Cleaved complexes are regenerated, and amplified products A₁ and A₂ interact with P₁ and P₂ primers to create duplexes. (B) Abbott ID NOW COVID-19 system. A patient swab (nasal, nasopharyngeal, or throat) is inserted in the sample receiver containing lysis buffer. After mixing for 10 s, the mixture is manually transferred to the test base holder containing lyophilized NEAR reagents. The instrument automatically performs heating and agitation, followed by signal generation via fluorescent detection. The assay targets the SARS-CoV-2 RdRp gene. Ref. ¹²⁹.

5.2.3.3.3. Recombinase polymerase amplification

RPA is an isothermal amplification technique, operating at 37 – 42°, requiring minimal sample preparation, and capable of amplifying as low as 1-10 target copies in less than 20

min¹⁴⁶. The working mechanism of RPA is illustrated in Fig. 41A. RPA has been widely used at the point of need. Compared to the NEAR technique, it requires only a pair of primers and is performed at a lower operating temperature¹⁴⁵. Compared to the LAMP technique, RPA is faster but due to the simpler primer design, it might yield unspecific amplification¹²⁹.

RPA primers for targeting the N genomic region of the SARS-CoV-2 genome have been developed¹⁴⁷. RPA reagents were mixed to enable one-spot RNA reverse transcription, followed by signal generation via fluorescent probe kits with a total assay time of 30 min and LOD of 0.2 copy/ μ L (Fig. 41B).

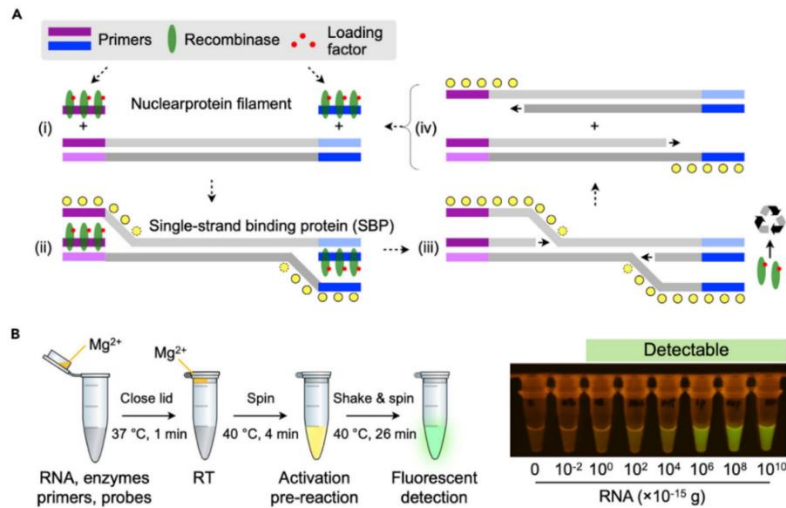


Figure 41. **An example of an RPA-based COVID-19 test.** (A) RPA mechanism. (i) Recombinases form complexes with each primer to scan the target to find complementary sequences. (ii) The complexes then bind to the complementary sequences and form a D loop structure as well as single-strand binding proteins to stabilize the displaced DNA chain. (iii) The recombinase then disassembles to be reused for the subsequent amplification cycle. (iv) DNA polymerase elongates the primers to create parallel strands to form duplexes. Repetition of these cycles results in exponential amplification. (B) RT-RPA assay for COVID-19 diagnosis. The extracted RNA sample is mixed with RPA reagents to perform RT at 37°. The tube is then spun to release the Mg²⁺ from the lid, followed by heating to 40° for 4 min to initiate RPA activation. After shaking and spinning, the reaction needs to proceed for 26 min at 40°. The signal is then generated via green fluorescent. (A, B) Ref.¹²⁹

5.2.4. CRISPR-based detection

Clustered regularly interspaced short palindromic repeats (CRISPR) is a family of DNA sequences found in the genome of prokaryotic organisms, e.g. bacteria, capable of recognizing foreign nucleic acids based on their sequence and subsequently eliminating them via CRISPR-associated (Cas) enzyme¹⁴⁸. CRISPR-Cas systems have been utilized for various applications such as genome editing, bioimaging of nucleic acids, and detection of nucleic acids. CRISPR-based diagnostics offers a unique way of signal amplification with the accuracy down to single-nucleotide variants¹⁴⁹.

Broughton et al. employed the Cas 12a enzyme for COVID-19 diagnosis. The assay was designed to target N and E genes of the SARS-CoV-2 genome and human RNase P as a control. Amplification and signal readout were rendered via RT-LAMP and lateral flow probes respectively, with the assay run-time of 45 min and LOD of 10 copy/uL¹⁵⁰ (Fig. 42A, B).

Several drawbacks still limit the practical usage of such assays. They still require nucleic acid amplification to achieve high sensitivity, multiple manual mixing, and incubation. On the contrary, most isothermal NAATs for COVID-19 diagnostics provide one-step amplification and detection¹²⁹. Joung et al. overcame this challenge by introducing a one-step approach called SHERLOCK Testing in One Pot (STOP) to integrate LAMP amplification with CRISPR-mediated detection (Fig. 42C, D). The signal was detected using a lateral flow readout with the assay run-time of 70 min and LOD of ~2 copy/mL for SARS-CoV-2 genome standards spiked into pooled saliva or NPS. Validation with clinical nasopharyngeal swab samples yielded the correct diagnosis of 12 COVID-19 positive and negative patients with 3 replications¹⁵¹.

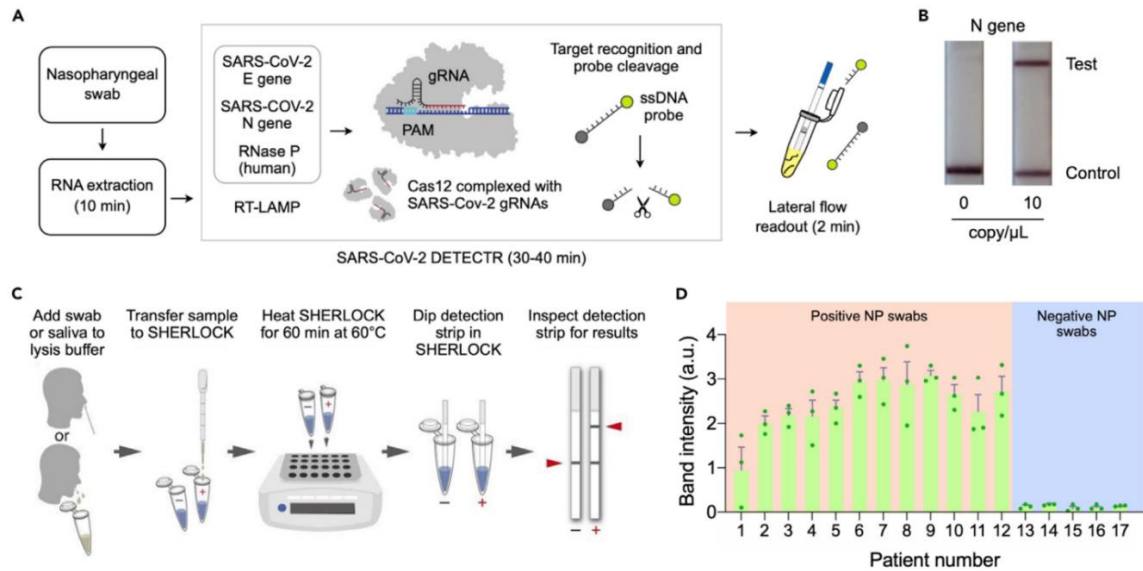


Figure 42. **An example of a CRISPR-based COVID-19 test.** An NPS sample is collected from a patient and RNA targets are extracted and amplified by RT-LAMP. Cas12 complexes, pre-incubated with SARS-CoV-2 guide RNAs (gRNAs) to recognize target DNA and cut the single-stranded DNA probes to generate a signal. (B) The intact and cleaved ddDNA reporters are captured on the control and test lines respectively on a lateral flow strip. (C) Workflow of SHERLOCK Testing in One Pot (STOP) in a schematic illustration. NPS or saliva sample is mixed with lysis buffer, followed by mixing the lysate with SHERLOCK master mix and heating the mixture at 60° for 60 min. The strips then are dipped into the SHERLOCK solution for signal generation. 12 positive and 5 negative NPS samples were tested via STOP and the assay made a correct diagnosis in all cases. The data were shown as mean \pm standard deviation from 3 independent experiments. (A - D) Ref.¹²⁹

5.2.5. Immunoassays

Immunoassays target virus-specific antigens or antibodies against the virus. While NAATs are suitable for viral load infections, immunoassays, in particular antibody tests, can provide information regarding current or past infections, thereby providing a better understanding of transmission dynamics¹²⁹. In this section, first, the fundamentals of immunoassays are explained. Then, the principles of assay development and design as well as the methods to describe an assay performance with the focus on the sandwich enzyme-linked immunosorbent assay (ELISA) are described. Next, existing immunoassays for COVID-19

diagnosis mainly including serologic tests, virus neutralization tests and rapid antigen tests are explained, and some selected examples from the literature are reported.

5.2.6. Fundamentals of immunoassays: Diffusion, convection, and reaction in surface-based biosensors

In this section, a paradigmatic model system for detecting a targeted molecule is presented, and the effects of diffusion, convection, and reactions are discussed (Fig. 43). It should be noted that here the main dimensionless parameters and their role in describing the behavior of a system are briefly presented. For more details, the reader is referred to read the paper by Squires et al¹⁵².

In the system shown in Fig. 29, the solution of interest with the volumetric flow rate of Q is introduced to a channel with the width of W_c and height of H , wherein one wall of the channel includes a sensor with the width of W_s and length of L . The sensor is functionalized with b_m receptors per unit area and the solution of interest includes the target molecule with the concentration of c_0 , the diffusivity of D , and binding constants of k_{on} and k_{off} .

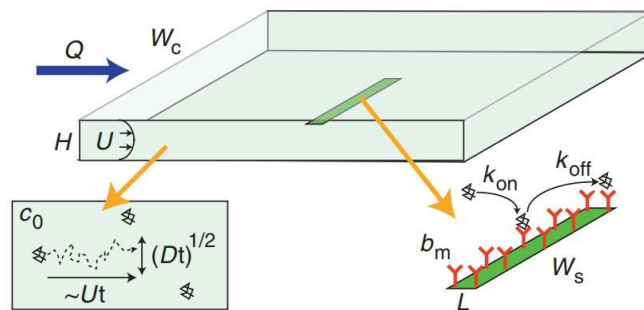


Figure 43. **A model system including an open-surface biosensor.** A solution of interest with the flow rate of Q , containing the target molecules with the concentration of c_0 and diffusivity coefficient of D , is introduced to a channel with the height of H and width of W_c . The sensor with the lengths of L and width of W_s is functionalized with b_m receptors per unit area. k_{on} and k_{off} are the first-order kinetic rate constants. Ref.¹⁵²

First, consider the abovementioned system in a condition that there exists only diffusion. In such a condition, as the target molecules are collected by the sensor, a depletion zone with the size of $\delta \sim \sqrt{Dt}$ is generated. However, convection halts this growth when the flow is introduced in such a system, and a steady depletion zone with the length of $\delta_s \sim \frac{DHW_c}{Q}$ is created. If the depletion zone $\delta(t)$ at some points is smaller than the steady value δ_s , the diffusive flux is stronger than the convective flux which renders the depletion zone to grow and be governed by diffusion. On the other hand, when the depletion zone $\delta(t)$ is greater than δ_s , the diffusion is outperformed by the convective delivery of target molecules and the depletion is thus compressed. A dimensionless number called the Peclet number can clearly describe the size of the depletion zone compared to the channel as well as the sensor. The channel Peclet number, Pe_H , and shear Peclet number, Pe_s , are given by the following equations¹⁵²:

$$Pe_H = \frac{Q}{W_c D} \quad (6)$$

$$Pe_s = 6 \left(\frac{L}{H} \right)^2 \frac{Q}{W_c D} \quad (7)$$

A relatively large Pe_H indicates that the depletion zone is thinner than the channel size and vice versa. With the same scenario, a relatively large Pe_s shows that the depletion zone is thinner than the sensor size and vice versa.

As discussed above, the Peclet number provides information regarding mass transport and the diffusion and convection limits. The dimensionless concentration, $\tilde{c} = \frac{c_0}{K_D}$, indicates which fraction of the molecules is bound to the sensor's binding sites at the equilibrium. A

relatively large \tilde{c} indicates that most of the available binding sites will be saturated at the equilibrium and vice versa.

Another important dimensionless parameter is the Damkohler number, D_a . D_a provided information regarding the how the system reaches equilibrium, i.e. through reaction or mass transport, and is formulated as follows¹⁵²:

$$D_a = \frac{k_{on}b_mL}{D\mathcal{F}} \quad (7)$$

Where \mathcal{F} is the dimensionless mass transport flux. A relatively large D_a indicates that the sensor's operation is limited by mass transport (and not by reaction) and vice versa.

5.2.7. ELISA: Development, optimization, and assay performance

ELISA is a laboratory-based immunological assay, typically performed on a multi-well plate coated with viral antigens, with high sensitivity and throughput. To perform an antibody test using ELISA, samples from a patient, e.g. blood, plasma, or serum, are added to the wells for antibody capture, followed by washing and introducing secondary antibodies labeled with enzymes for catalyzing signal generation. The signal can be generated in different formats, e.g. colorimetric, fluorescent, or electrochemical. ELISA can reach analytical sensitivity down to the picomolar range with a total assay time of 2-24 hr depending on the protocol^{153,154}.

For the design and development of an ELISA, first, the format of the assay needs to be selected. 4 basic formats of ELISA exist for the detection of the analyte of interest including direct ELISA, indirect ELISA, sandwich ELISA, and competitive ELISA (Fig. 44). Depending on the application, more complex formats can also be created by combining basic formats. The simplest format is direct ELISA, which requires antigen to be adsorbed to the plate before being bound by a labeled "detection" antibody. The first and only antibody that acts as both

an antigen recognition molecule and a signal delivery molecule is referred to as "direct." An "indirect" ELISA, on the other hand, divides the detection and signaling tasks between "primary" and "secondary" antibodies. In an indirect ELISA, an unlabeled antibody recognizes the plated antigen, which is subsequently recognized by a secondary antibody bearing the signaling mechanism. The adsorption of a "capture" antibody on the plate distinguishes a sandwich ELISA from others. The plating antibody binds or captures the antigen, which is then "sandwiched" between the capture and a detecting antibody that detects a unique epitope on the antigen. A sandwich ELISA has the advantage of being able to measure antigen from impure samples. The last basic format is the competitive ELISA. Similar to direct ELISA, the antigen can be directly adsorbed to the plate in competitive ELISA. Prior to application to the plate, the detecting antibodies are pre-incubated with samples containing unknown levels of antigen. Antigen-rich samples occupy binding sites on the primary antibody, preventing it from attaching to the plated antigen. Samples containing less antigen, on the other hand, will have more antibodies available to bind to the plated antigen, resulting in a larger signal^{155,156}. Once the format of the ELISA is selected, optimization procedures need to be performed to improve assay performance. Herein, we focus on the ELISA with the sandwich format. To this end, we will first describe the general protocol of a sandwich ELISA and next, explain the main factors involved in the optimization process.

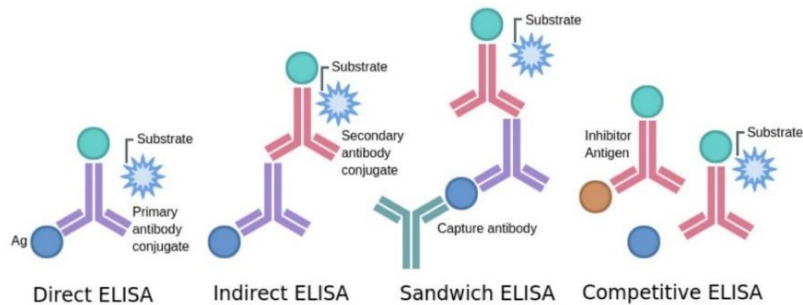


Figure 44. **Different formats of ELISA.** 4 basic formats exist for ELISA: Direct, indirect, sandwich, and competitive. Ref.¹⁵⁷

5.2.7.1. Sandwich ELISA protocol

Fig. 45 illustrates a general protocol of a microplate-based sandwich ELISA carried out in 96-well plates by Thermo Fisher Scientific Inc.¹⁵⁸ It should be noted that this is only a general protocol to familiarize the reader with the different steps of a microplate-based sandwich ELISA. Depending on the case and sensitivity requirement, the conditions of the test such as incubation time, the choice, and volume of reagents need to be optimized. In the first step, the capturing antibody is coated on the surface and incubated for 2 h to overnight. Next, the wells are washed 3 times and blocked by a blocking buffer for 1 h to overnight to reduce the likelihood of non-specific binding events. Next, the blocking solution is removed, and the wells are washed 3 times. Then, the sample is added to each well and incubated for 1 h to allow for the analyte to bind the capture antibody coated on the surface. The wells are then washed 3 times, followed by the addition of the biotinylated detection antibody to bind to the sample and therefore create a sandwich complex. After incubation for 1 hr, the wells are washed to discard the unbound molecules and the enzyme conjugate is then added to the wells to bind the to the detection antibody. The plates are then washed 6 times after incubation (~1 h) to rinse the unwanted molecules, followed by the addition of substrate

solution for signal generation. The reaction is then stopped after a certain duration (e.g. 30 min) and the signal intensity is measured via appropriate software. The data are then analyzed to generate the calibration curves¹⁵⁸ (Fig. 45). Sandwich ELISA offers high sensitivity and particularly is praised for high specificity as there exist two binding events for recognizing the sample (i.e., one for the capturing antibody and another one for the detection antibody). The microplate-based sandwich ELISA also offers high throughput thanks to the 96- and 384-well plate. However, laboratory (sandwich) ELISA is typically long, and depending on the protocol, it may take from hours to days, in the case of overnight incubation. Commercially available products with an optimized surface to capture the analyte of interest also exist (such as Pierce™ Protein A Coated Plates by Thermo Scientific™; catalog number: 15155) to cut down the number of ELISA steps, and therefore the total duration.

5.2.7.2. Plates

Differential antigen adsorption efficiency and non-specific binding may emerge from plate chemistry variations, influencing signal-to-noise ratios. The geometries of ELISA plates can also affect plating efficiency and, as a result, final signal strength. To identify the optimal plate condition, different plate chemistries and geometries side by side need to be compared side by side¹⁵⁵. It should be noted that ELISA can also be employed in point-of-care settings. In this case, microplate ELISA is no longer used and other formats, which are less labor-intensive, are of interest. As an example, ELISA can be performed on a nitrocellulose membrane¹². The study by Yafia et al. developed a COVID-19 antibody test on a nitrocellulose membrane connected to a capillary circuit for sequential delivery of the sample, reagents, and washes to the reaction chamber (i.e., nitrocellulose membrane)¹². In this case, the physical and

chemical properties of the nitrocellulose membrane (such as backed versus unbacked and capillary flow rate) need to be adjusted based on the sample type, assay background, assay time, and required analytical sensitivity¹⁵⁹.

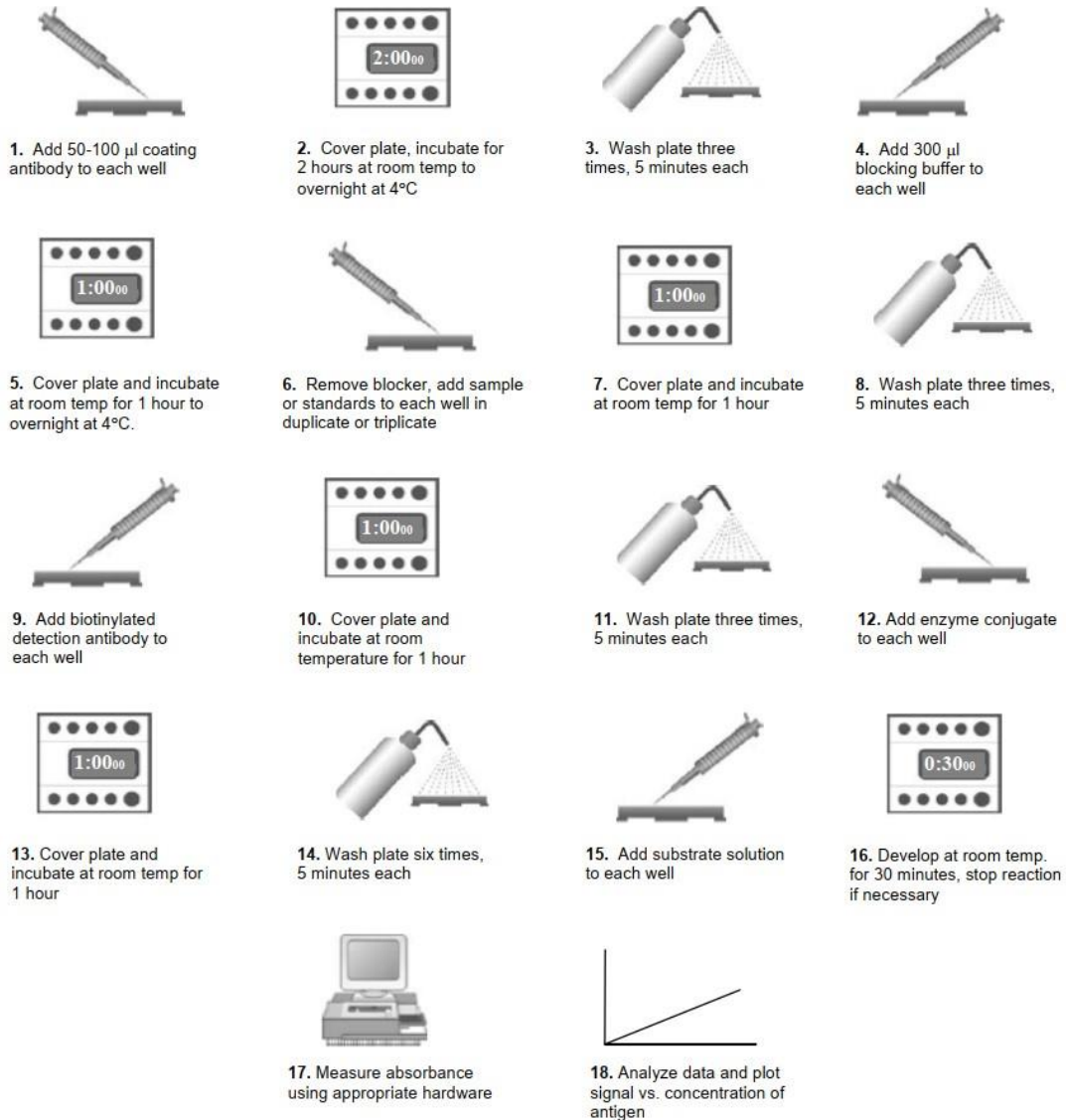


Figure 45. General sandwich ELISA protocol by Thermo Fisher Scientific Inc. that uses a biotinylated detection antibody and enzyme conjugate indirect detection system. Ref¹⁵⁸

5.2.7.3. Antibody Affinity

Antibody affinity has a significant impact on ELISA performance. At the same concentrations, different clones will perform better than others. While affinity cannot be easily handled other than by developing or discovering alternative antibodies, titrating concentrations will optimize the amount of antibody employed and, therefore, accommodate even low-affinity antibodies. Negative controls are essential elements in this step as increasing antibody concentrations increases the possibility of non-specific binding¹⁵⁵.

5.2.7.4. Antibody clonality

The type of the antibody, i.e., monoclonal or polyclonal, as capture or detection species affect the assay performance. There exist two opposing theories about antibody clonality. Monoclonal antibodies are more selective than polyclonal antibodies, although their signal is often lower due to epitope recognition limitations. Although polyclonal antibodies identify more epitopes per antigen, they nevertheless have the potential for undesired cross-reactivity, even when affinity-purified polyclonal antibodies are used. A monoclonal capture antibody will only recover particular targets from a sample, whereas a polyclonal capture antibody will recover the maximum amount of target, albeit with some non-specific binding. The detection reagent can be of either clonality of antibody, with the same specificity constraints. ELISA performance is inevitably influenced by sample quality. Monoclonal antibody capture would likely be beneficial in complex samples, but polyclonal antibody capture would be an appropriate choice in samples with a simple composition but low target concentration. In each case, empirical testing is required to disclose the best clonality use or combinations of clonality¹⁵⁵.

5.2.7.5. Reagent concentration

Testing different concentrations of reagents, e.g., sample, blocking buffer, capture antibody, detection antibody, enzyme conjugate, and substrate, is a major part of the optimization process. In general, different concentration of each reagent needs to be prepared to investigate assay performance in terms of good dynamic range and signal-to-noise ratio. It should be noted that in many cases, a checkerboard titration can be used to optimize two components simultaneously for obtaining the highest analytical performance¹⁶⁰.

5.2.7.6. Signal development

ELISA, as the name implies, benefits from enzymatic signal development. Different enzymes can be used for this purpose. Horseradish peroxidase (HRP) and alkaline phosphatase (ALP) are the most often utilized enzyme labels. Other enzymes, such as β -galactosidase, acetylcholinesterase, and catalase, have also been utilized. Selecting the appropriate substrate is the crucial step for a successful ELISA. In general, the substrate should be of high sensitivity and compatible with the developed ELISA system. Several commercially available substrates exist for conducting ELISA. Colorimetric, fluorescent, and chemiluminescent substrates are the most common types. Colorimetric substrates are cost-effective and need no equipment, thereby suitable for point of care settings, but typically offer low sensitivity. Fluorescence substrates render multiplexing straightforward, but they need equipment for signal measurement and typically do not offer high sensitivity. Chemiluminescent substrates are highly sensitive, but they need special equipment for signal measurement and multiplexing might be difficult to implement^{155,156,160}.

5.2.7.7. Assay performance and the calibration curve

A calibration curve (also called a standard curve or dose-response curve) is used in a quantitative immunoassay to quantify the analyte concentration of a sample indirectly from its response. The calibration curve is a graph that shows the relationship between two variables. A graph showing known concentrations vs their signal responses. On the concentration axis, these calibration curves typically cover two or more orders of magnitude and one or two orders of magnitude on the response axis. Immunoassay calibration curves generally create an S-shaped sigmoidal curve, which necessitates a logistic regression to match the curve beyond its linear range (Fig. 46). The logistic range is the name given to this new range, which is best defined by a 4-parametric logistic (4PL) curve^{156,161}. The equation for a 4PL is represented as follows:

$$y = d + \frac{a - d}{1 + \left(\frac{x}{c}\right)^b} \quad (8)$$

Where a and d are theoretical responses at zero and infinity, respectively, b is the slope factor (i.e., Hill slope) and c is the mid-point concentration (inflection point).

There are different terms to describe an assay performance including but not limited to the limit of the blank (LoB), the limit of detection (LoD), the limit of quantitation (LoQ), and analytical sensitivity. These terms have distinct definitions according to the published standards and their usage instead of each other should be avoided. Below, the most frequent terms will be briefly defined.

One way to investigate assay performance is to solve the equation 8 for x by substituting y with 3 times the standard deviation of the blank as follows^{156,161}:

$$X = c \left(\left(\frac{a - d}{3 * SD_{\text{blank}} - d} \right) - 1 \right)^{\frac{1}{b}} \quad (9)$$

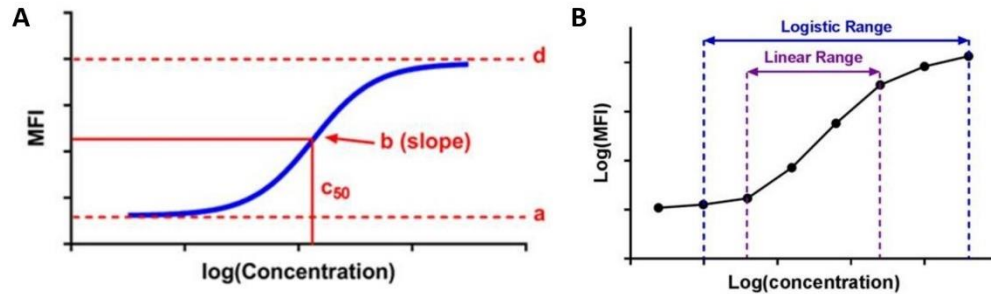


Figure 46. **4-parameter logistic regression and the assay dynamic range.** A. Panel A shows a typical ELISA standard curve and panel B depicts the same assay dynamic range. MFI stands for mean fluorescent intensity. Ref.¹⁶¹

The above method has some drawbacks. From a practical perspective, it is very difficult to obtain a true zero sample with a matrix that represents that of a patient sample. Another drawback is that because there is no analyte present in the negative sample, this simply measures the system background noise. To overcome this limitation, the imprecision of very low concentration samples, either within or between assays, is used to investigate assay performance.

According to the previous reports^{156,161}, the value determined from equation 8 is referred to as LoD. To provide a standard to describe assay performance, the Clinical and Laboratory Standards Institute (CLSI) has published a guideline EP17 for determining the limit of blank (LoB), the limit of detection (LoD), and the limit of quantitation (LoQ) which are defined as follows:¹⁵⁶

According to EP17, LOB is defined as the maximum apparent analyte concentration expected to be found when replicates of a blank sample with no analyte are tested. LOB is formulated as¹⁶²:

$$\text{LoB} = \text{mean}_{\text{blank}} + 1.654(\text{SD}_{\text{blank}}) \quad (10)$$

EP17 defines LOD as the lowest analyte concentration at which the LOB may be reliably differentiated, and detection is possible. The LOD is calculated using both the observed LOB and test duplicates of a sample with a low analyte concentration. LOD is formulated as¹⁶²:

$$\text{LoD} = \text{LoB} + 1.654(\text{SD}_{\text{low-concentration sample}}) \quad (11)$$

As stated by EP17, the LOQ is defined as the lowest concentration at which the analyte may be reliably detected while still meeting certain bias and imprecision requirements. LOQ may be the same as or significantly greater than LOD (the one describing functional sensitivity)¹⁶². The assay dynamic range (or linear range) is another frequently-used term to describe an assay performance. The dynamic range spans the lowest to the highest concentration of the target analyte that can be reliably detected. To obtain the dynamic range from the standard curve, there should be a strong correlation (i.e., linear relation) between the analyte concentration and signal intensity which replicates having low signal standard deviations. The slope of the calibration curve in the linear range is defined as the “analytical sensitivity”. Analytical sensitivity is sometimes used as a synonym for the LoD. But, this usage should be avoided as these 2 terms are different and have distinct definitions; the LoD may be found at a concentration below the linear range of an assay where the calibration curve is not valid. However, since these terms have been used interchangeably in the literature, the reader

needs to refer to the context to understand the method and the corresponding formulation by which the assay performance was described.

Another metric that is typically reported in representing assay performance is the coefficient of variation (CV). CV represents a statistical measure of the deviation within replicates and is calculated by dividing the standard deviation of the replicates by their mean. %CV values of less than 15 are typically acceptable, but the limit mainly depends on the application¹⁶³.

5.2.8. COVID-19 immunoassays

5.2.8.1. Serologic tests

Serologic tests aim to detect the presence of host-derived antibodies against a microorganism, typically from blood-based samples, which could provide an understanding of past infections (Fig. 47A). Serologic tests can be used as a wide screening tool. For instance, by random testing of the general public for antibodies against SARS-CoV-2, the true size of the infection and its mortality can be monitored¹²⁹. According to the previous SARS epidemics, the viral-specific immunoglobulin M (IgM) is mainly present at the initial stage of the infection, followed by the production of viral-specific immunoglobulin G (IgG) for long-term immunity (~2 years)¹⁶⁴. The immunological data for SARS-CoV-2 have yet to be investigated, but a recent study testing 214 patients reported the same pattern. It was observed that IgM positivity was greater than that of IgG within the initial days of infection, which then dropped after 1 month¹⁶⁵ (Fig. 47B).

To design a serologic test, it is critical to producing appropriate viral antigens or recombinant proteins to specifically capture host antibodies. N and S₁ proteins are likely to be the most appropriate immunogens for COVID-19 serologic test^{166,167}. A study on the analysis of N and

S protein among coronaviruses reported that the S₁ subunit of SARS-CoV-2 has the least overlap with the others (Fig. 47C). They further investigated the performance of N and S₁ proteins by performing ELISA in serum samples from healthy donors and patients infected with non-CoV, human (H) CoV, middle east respiratory syndrome (MERS)-CoV, SARS-CoV, or SARS-CoV-2. S₁ ELISA indicated higher specificity, while N ELISA offered more sensitivity¹⁶⁷ (Fig. 47D).

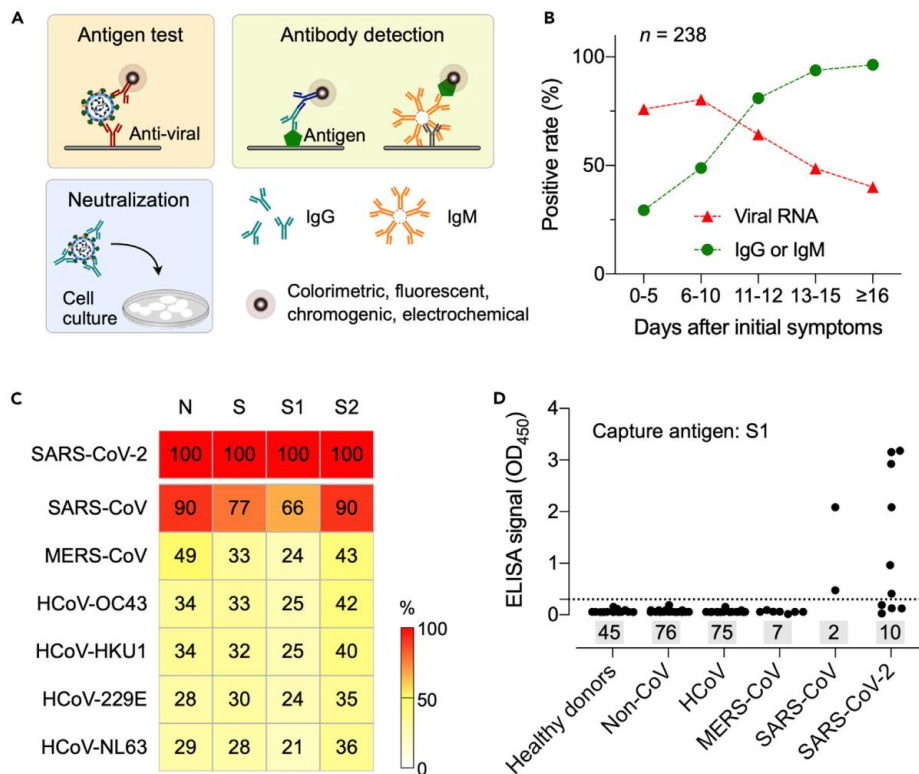


Figure 47. **Immunoassays for COVID-19 diagnosis.** (A) The antigen tests detect the presence of virus in a patient sample via a capture antibody and a detection antibody each binding to a specific region of the target. Antibody detection assay captures the viral antibodies (e.g. IgG or IgM) generated from host immune response via viral antigens or antihuman antibodies. Viral neutralization tests detect the effective antibodies capable of preventing viral infection of cells. (B) The positive rate of viral RNA and antibodies (IgG or IgM) for 238 COVID-19 patients. The positive rates of antibodies were low during the first 5 days of the initial onset of symptoms but increased rapidly by disease progression. (C) The similarity between N and S proteins as well as S₁ and S₂ subunits in different types of coronaviruses, compared to SARS-CoV-2 (100 indicates 100% concordance). Among all targets, the S₁ subunit indicates the least similarity. (D) Evaluation of S₁ ELISA (using S₁ subunit to capture antibodies) in capturing antibodies against SARS-CoV-2 among all different types of coronavirus infections. S₁ indicated no cross-reactivity for non-SARS coronavirus infections and a slight cross-reactivity for SARS-

CoV one. ELISA cut-off values are shown by the dotted horizontal line and the number of patients is shown in the gray squares. OD represents optical density. (A - D) ref.¹²⁹

It should be noted that the data regarding this are contradictory and more findings are in demand to shed light on the performance of each target antigen. For instance, Okba et al. examined the performance of N protein, S₁ subunit, and RBD as a viral antigen and reported higher analytical sensitivity for N ELISA and RBD ELISA¹⁶⁷. On the contrary, the study by Liu et al. on 214 COVID-19 patients reported higher sensitivity for S-based ELISA as compared to the N-based ELISA¹⁶⁵ (Fig. 48).

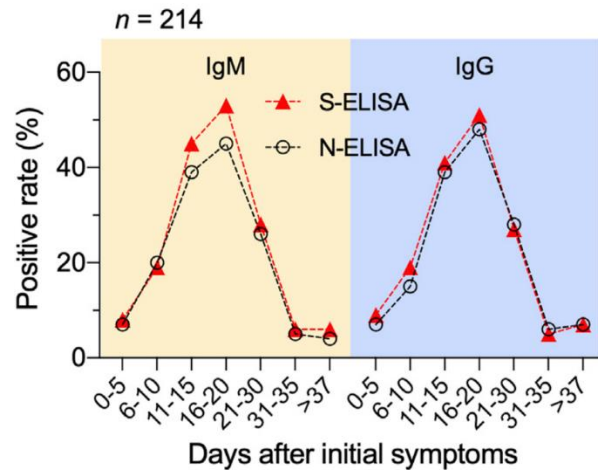


Figure 48. **Comparison of ELISA with S and N proteins to detect IgM and IgG.** In a serologic study on 214 patients, the S protein performed slightly better than the N protein as a capturing antibody for both IgM and IgG detection. Ref.¹²⁹

Novel formats have also been developed for the serologic tests. As an example, Ali et al developed a 3D-printed COVID-19 test chip implemented with a novel, graphene-based biosensor that was commutable with a smartphone-based user interface to detect antibodies against SARS-CoV-2 S₁ and RBD¹⁶⁸. The sensor was able to be regenerated in 1 min by treatment with a low-pH solution to remove the antibodies for the antigens, therefore allowing for sensing of multiple samples via one device. In phosphate buffer saline, the assay

indicated the LoD of 2.8×10^{-15} mol/L and 16.9×10^{15} mol/L for SARS-CoV-2 S₁ and RBD, respectively, within 10 s (Fig. 49)¹⁶⁸.

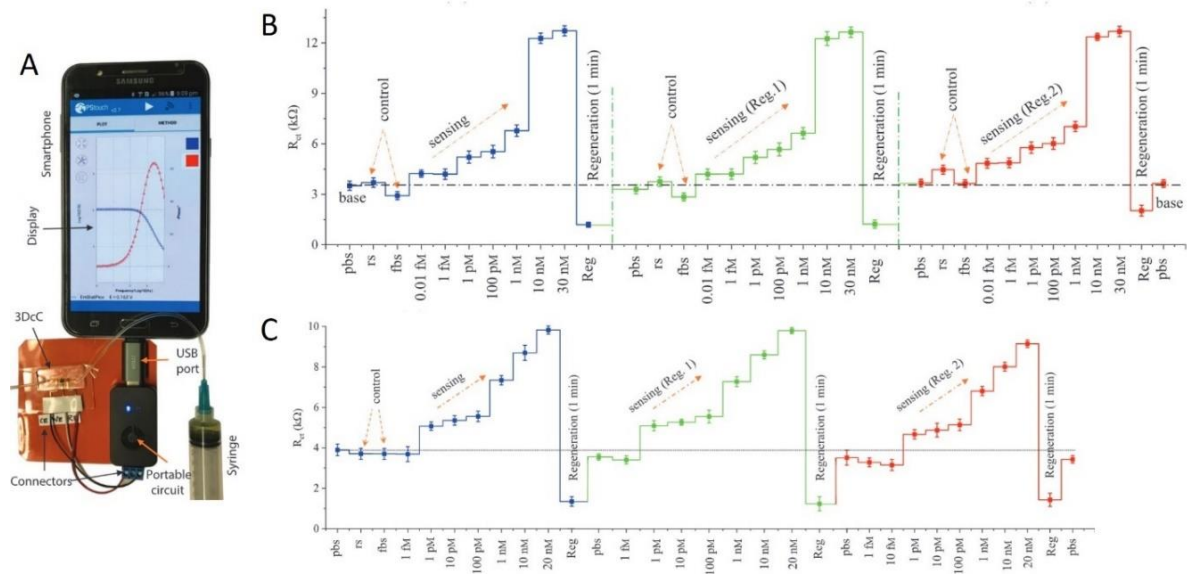


Figure 49. **3D-printed COVID-19 test chip developed by Ali et al.¹⁶⁸ and the corresponding dose-response curves.** (A) The 3D-printed COVID-19 test chip connected a portable potentiostat signal readout and a smartphone for communication with a user. (B, C) The charge transfer resistance (R_{ct}) for different concentrations of antibodies against SARS-CoV-2 (B) spike S₁ and (C) RBD antigens. Fetal bovine serum (fbs) and rabbit serum (rs) were used as control samples. 3 successive readings were obtained for all samples. Ref.¹⁶⁸

Another example is the instrument-free ELISA-on-chip platform developed by Yafia et al. for detecting SARS-CoV-2 N protein human antibody spiked in natural saliva samples. The developed platform was compatible with a cellphone reader system or a regular scanner for signal analysis, and the developed assay yielded a colorimetric brown precipitate which could serve as an immediate readout or be used for archival purposes¹² (Fig. 29).

5.2.8.2. Virus neutralization test

Virus neutralization test (VNT) is basically a serological test to determine the presence and magnitude of functional systematic antibodies in a patient's blood. 2 types of VNTs exist. The 1st type is a conventional VNT which aims for determining neutralizing antibodies in a

patient's blood, requiring live SARS-CoV-2 in a biosafety level 3 laboratory with a total assay time of 2-4 days. The 2nd type is the pseudovirus-based VNT which can be carried out in a biosafety level 2 laboratory, yet still requires the use of live cells and viruses¹⁶⁹. Other assays, such as ELISA and lateral flow assays, represent the latter one which detects the total binding antibodies without the ability to distinguish between total binding antibodies and neutralizing antibodies¹⁷⁰.

Tan et al. developed a surrogate VNT capable of detecting neutralizing antibodies that obviates the need for any live viruses or cells and can be performed in a biosafety level 2 laboratory with a total assay time of 1-2 hr. The test was designed to mimic virus-host interaction using the receptor-binding domain (RBD) of S protein and host receptor ACE2. In a clinical trial on COVID-19 patients, the test indicated 95-100% sensitivity and 99.93% specificity¹⁷¹.

In a preprint, Zhang et al. proposed a SARS-CoV neutralizing antibody test in a lateral flow format. The developed assay was able to detect interactions between RBD and ACE2, and as a positive reading reference, 2 additional test lines were also implemented to capture interactions between an anti-S₁ protein with anti-RBD IgG and anti-RBD IgM. Validation with plasma PCR results yielded 90% agreement among PCR negative samples. However, the results of IgG and IgM against S₁ protein showed very poor negative percentage agreement (53.3%). The contributing factor to this discordance was reported to be true false negative of PCR results and the possibility that the tested patients might have been infected with other types of coronaviruses rather than SARS-CoV-2¹⁷².

5.2.8.3. Antigen detection assay

Antigen detection assays detect the presence of viral proteins in a patient's sample through an immunocapture format (Fig. 29A). Antigen detection assays can be performed in different formats such as a laboratory diagnostic tool or a rapid point-of-care test. An example of the former case is the study by Thudium et al. in which they developed a laboratory ELISA for detecting the nucleocapsid (N) protein of SARS-CoV-2 from blood samples¹⁷³. The latter is the most frequently-utilized format of antigen detection assays in which they are presented as single-use, lateral flow, antigen-detection rapid diagnostic tests (Ag-RDTs) with a visual or portable device-based readout and an overall assay time of 15-30 min.

Ag-RDTs are fast, cheap, and offer a high level of specificity, but they are not typically as sensitive as NAATs. Ag-RDTs can be useful in the following instances: (i) In a case that demands for COVID-19 testing exceed the capacity of laboratory PCR testing, Ag-RDTs can be used to reduce the number of molecular tests, thereby reducing the waiting time for results as well as the costs. (ii) In special cases in which hospitals or clinics are overcrowded with patients having COVID-19 symptoms, and they need to wait for several hours for the results, or the samples need to be sent to central laboratories to be processed, Ag-RDTs can be used to triage patients within 15 min. As Ag-RDTs can effectively detect patients with a high viral load¹⁷³, who are more likely to be infectious, a smaller proportion of the patients require PCR testing. (iii) Ag-RDTs can be readily used at the point of care, particularly at home, to minimize the contact of suspected cases with the public or health care professionals, thereby reducing the spread of COVID-19 and assisting in the disease management ¹⁷⁴.

Several studies investigated the performance of commercially available Ag-RDTs^{174,175}. Table 2 illustrates the examples of 6 commercially available Ag-RDTs with FDA-EUA, with 2 of them having a world health organization (WHO) emergency use listing (EUL) as well.

Table 2. Examples of COVID-19 antigen-detection rapid diagnostic tests.¹⁷⁴

	Sample type	Time of sample collection *	Results reading	Sensitivity, specificity [#]	Comments
Abott BinaxNOW USA	Nasal swab	0-7 days	Visual, 15 min	97%, 99%	WHO EUL; US FDA EUA; app for results; influenza A and B test available
Abott panbio, USA	Nasal swab, nasopharyngeal swab	0-7 days	Visual, 15-20 min	93%, 99%	WHO EUL; US FDA EUA pending
Access Bio CareStart, USA	Nasal swab, nasopharyngeal swab	0-5 days	Visual, 15-20 min	88%, 100%	US FDA EUA
BD Veritor, USA	Nasal swab	0-5 days	Instrument, 30 min	84%, 100%	US FDA EUA
LumiraDx, UK	Nasal swab	0-12 days	Instrument, 12 min	98%, 97%	US FDA EUA
Quidel Sofia SARS Antigen Fluorescent Immunoassay, USA	Nasal swab, nasopharyngeal swab	0-5 days	Instrument, 20 min	97%, 100%	US FDA EUA; does not differentiate between SARS-CoV and SARS-CoV-2
Quidel Sofia Flu and SARS Antigen Fluorescent Immunoassay, USA	Nasal swab, nasopharyngeal swab	0-5 days	Instrument, 20 min	95%, 100%	US FDA EUA
SD Biosensor, South Korea	Nasal swab, nasopharyngeal swab	Not stated	Visual, 15-30 min	97%, 100%	WHO EUL

Data from the Foundation for Innovative New Diagnostics.² SARS-CoV= severe acute respiratory syndrome coronavirus. FDA= Food and Drug administration. WHO= World Health Organization. EUL= Emergency Use Listing. EUA= Emergency Use Authorization. *Days after symptom onset. #Data from manufacturer.

Selecting the pairs of capture and detection antibodies in an antigen test is a critical factor.

To this end, Cate et al. used an automated liquid handling system to perform LFAs with high throughput to test 1021 pairs of antibodies against SARS-CoV-2 N protein and to identify the

pairs with the highest affinity¹⁷⁶. In another study by the same group, Grant et al. developed an Ag-RDT for targeting SARS-CoV-2 N protein in a lateral format using commercially available antibodies and reagents. The assay achieved the LOD of 1.4×10^4 copies/mL for gamma-irradiated SARS-CoV-2 particles in pooled nasal matrix with a total assay time of ~ 30 min¹⁷⁷ (Fig. 50).

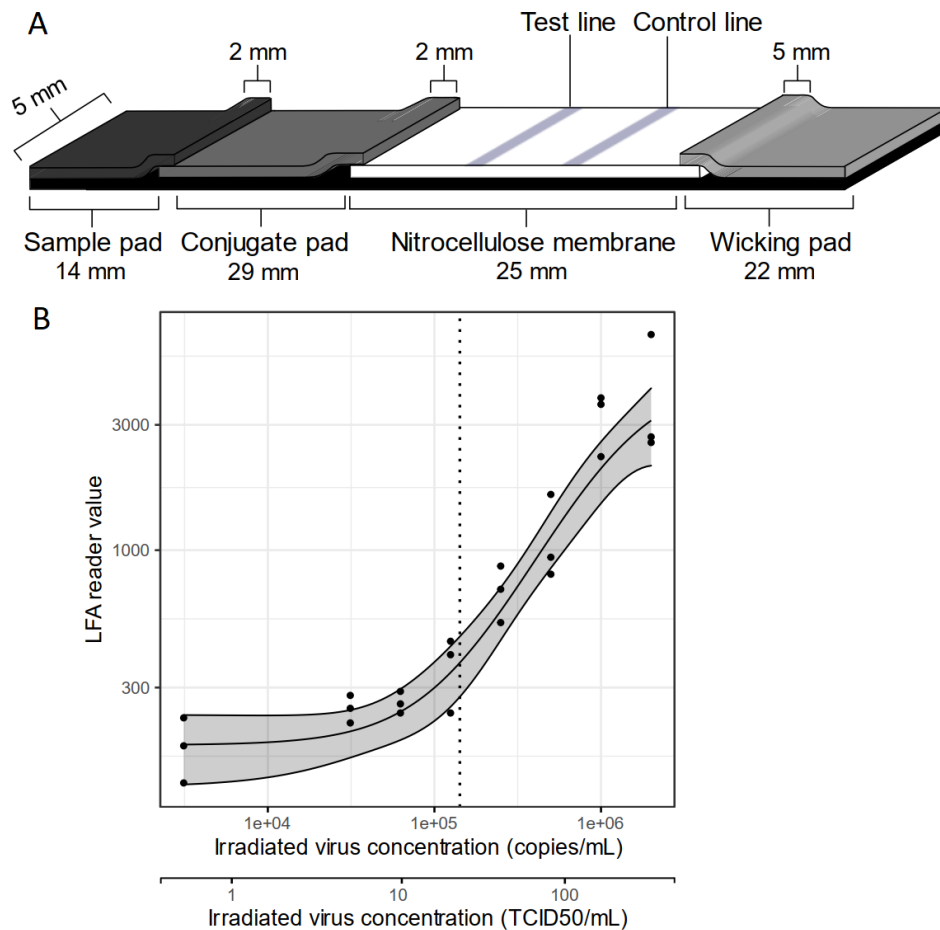


Figure 50. **Lateral flow immunoassay for SARS-CoV-2 N protein detection developed by Cate et al¹⁷⁷.** (A) The schematic illustration of the lateral flow device comprising a sample pad, conjugation pad, nitrocellulose membrane, and wicking pad. The sample from the nasal swab is mixed with lysis buffer and loaded onto the sample pad. Passing the conjugation pad, the mixture rehydrates the detection antibodies conjugated to (blue) latex beads lyophilized on the conjugation pad, and the N proteins if present in the sample bind to the antibodies. The mixture next passes the test line where capture antibodies are spotted, and the N protein-detection antibody complex can be captured. A control line is also included to confirm test reliability. A Wicking is implemented at the end to absorb the residual amount (B) The dose-response curve for gamma-irradiated viral particles in pooled nasal samples quantified by a lateral flow reader. LOD: 1.4×10^5 copy/mL. (A and B) ref.¹⁷⁷.

Antigen detection assays can also be performed in novel formats. As an example, Haghayegh et al. developed a point-of-care microfluidic device integrated with an electrochemical sensor for detecting the N protein of SARS-CoV-2 in 15 min. The layout of the microfluidic device is shown in Fig. 51. By spiking different concentrations of SARS-CoV-2 N protein in phosphate buffer saline, the assay indicated the dynamic range and LoD of 10 – 1000 pg/mL and 3.1 pg/mL, respectively¹¹².

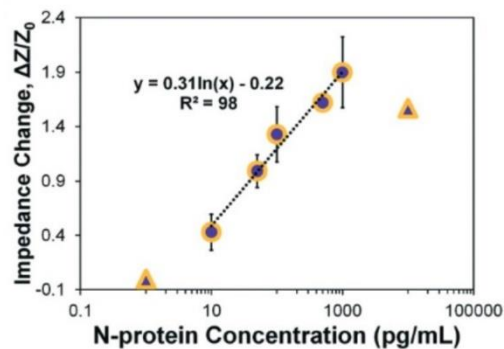


Figure 51. Dose-response curve of the electrochemical biosensor developed by Haghayegh et al.¹¹² across different concentrations of SARS-CoV-2 N protein. Ref.¹¹²

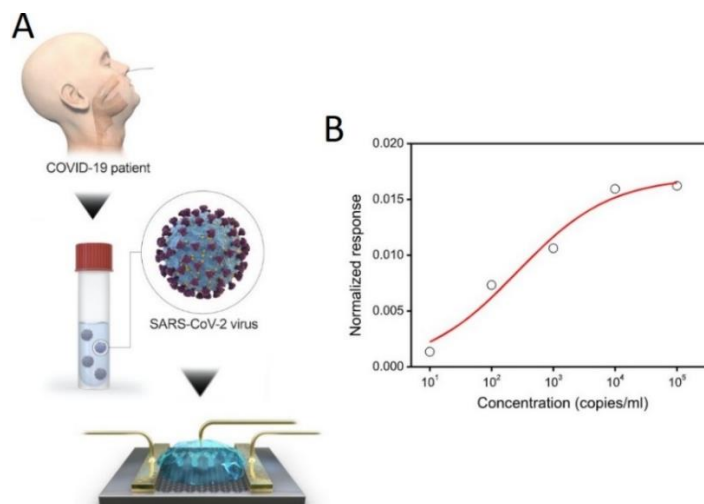


Figure 52. Field-effect transistor-based biosensor developed by Seo et al.¹⁷⁸ and the corresponding dose-response curve. (A) The schematic illustration of the biosensor for SARS-CoV-2 detection from NPS. (B) The dose-response curve across different concentrations of NPS acquired from patients. Ref.¹⁷⁸

Another example is the field-effect, transistor-based biosensor developed by Seo et al. for detecting the N protein of SARS-CoV-2 in clinical samples (Fig. 52). The assay indicated the LoD of 2.42×10^2 copy/mL for NPS specimens collected from COVID-19 patients¹⁷⁸.

As mentioned earlier immunoassays for detection of SARS-CoV-2 typically target a protein in the virus structure¹²⁹, with N protein being the most common candidate^{176,177,179}.

Nonetheless, immunoassays can be used to target the viral genome. In an interesting study, Wang et al. developed a rapid lateral flow immunoassay for the fluorescence detection of SARS-CoV-2 RNA from throat swabs or sputum samples in less than an hour (Fig. 53). The designed assay which was referred to as hybrid capture fluorescence immunoassay (HC-FIA) utilized a DNA probe to target 3 genomic regions of SARS-CoV-2 RNA (i.e., open reading frame, N protein, and E protein) and a fluorescent-nanoparticle-labeled monoclonal antibody that can bind to the DNA-RNA complex. In a clinical trial with 734 patient samples, the assay indicated the sensitivity and specificity of 100% and 99% respectively¹⁸⁰.

5.2.9. Different sample specimens for COVID-19 diagnosis

Various specimens such as NPS (nasopharyngeal swabs), oropharyngeal swabs (OPS), sputum, plasma, and saliva have been used for COVID-19 diagnosis, with NPS being the current standard sample specimen⁸. Several factors mainly including the amount of viral load, ease of accessibility, and non-invasiveness determine the suitability of a sample specimen for testing⁴. Sharma et al. investigated the sensitivity of NPS, oropharyngeal swabs (OPS), combined NPS and OPS, sputum, plasma, serum, and urine by RT-PCR. The combination of NPS and OPS yielded in greatest sensitivity (100%), followed by NPS (91.5 %), OPS (72.3%), and sputum (63%) whereas no virus was found in urine, plasma, and serum⁴.

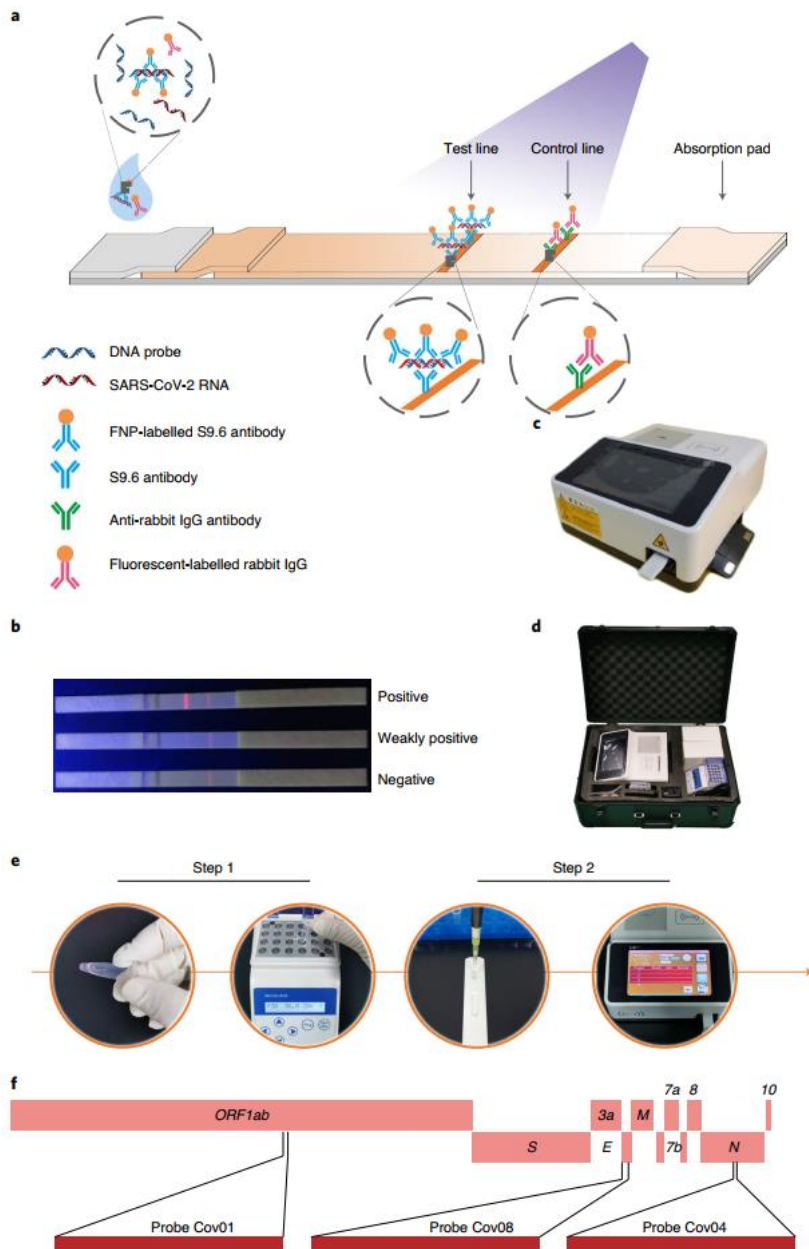


Figure 53. **HC-FIA developed by Want et al.¹⁸⁰ for SARS-CoV-2 detection.** (a) Schematic illustration of the assay principles. Throat or sputum samples are lysed, releasing the virus RNA to be hybridized with the specific SARS-CoV-2 DNA probe. The resulting RNA-DNA hybrid creates a complex with fluorescent nanoparticle (FNP)-labeled S9.6 antibodies, which then passes the nitrocellulose membrane to be captured by the S9.6 antibodies on the test line for gradual generation of fluorescent signal. (b) Representative results on the later flow strips. (c) Fluorescence analyzer device. (d) The portable suitcase laboratory with a dimension of $55.5 \times 37 \times 23 \text{ cm}^3$ and weight of 8.5 kg. (e) HC-FIA includes 2 steps: 1st, nucleic acid hybridization at a constant temperature, and 2nd, running the later flow device and data analysis via fluorescence analyzer. (f) DNA probe distribution on the SARS-CoV-2 genome. The probes target 3 regions of the virus genome. Ref.¹⁸⁰.

Recent studies also suggest saliva as a non-invasive, patient-friendly sample source for COVID-19 diagnosis^{5-7,181}. Teo et al. investigated the sensitivity of saliva, NPS, and self-collected nasal (SN) swabs by RT-PCR and found that the percentage of test-positive saliva (62%) was greater than NPS (44.5%) and SN (37.7%) samples⁶. In another study, Savela et al. monitored the viral load profiles and diagnostic sensitivity of saliva and anterior-nares nasal swabs for 7 individuals from the incidence of infection to 14 days post-infection. They reported that high-sensitivity saliva testing outperformed low- and high-sensitivity nasal swab testing by 5.5 and 4.5 days of positivity respectively, which suggests that high sensitivity saliva testing is more reliable for earliest detection¹⁰ (Fig. 54).

Butler-Laporte et al. conducted a systematic review and meta-analysis regarding the comparison of saliva and NPS NAAT for COVID-19 diagnosis. They reported significant variability in patient selection, study design, and stage of illness among the studies. But overall, it was concluded that saliva NAAT diagnostic accuracy is comparable to that of NPS NAAT, which suggests the use of saliva as an alternative sample specimen to NPS for NAATs⁷. It is important to note that the abovementioned studies compared the performance of different sample specimens by RT-PCR^{4-7,181}. However, the data regarding other types of tests, i.e., immunoassays, are missing and need to be investigated.

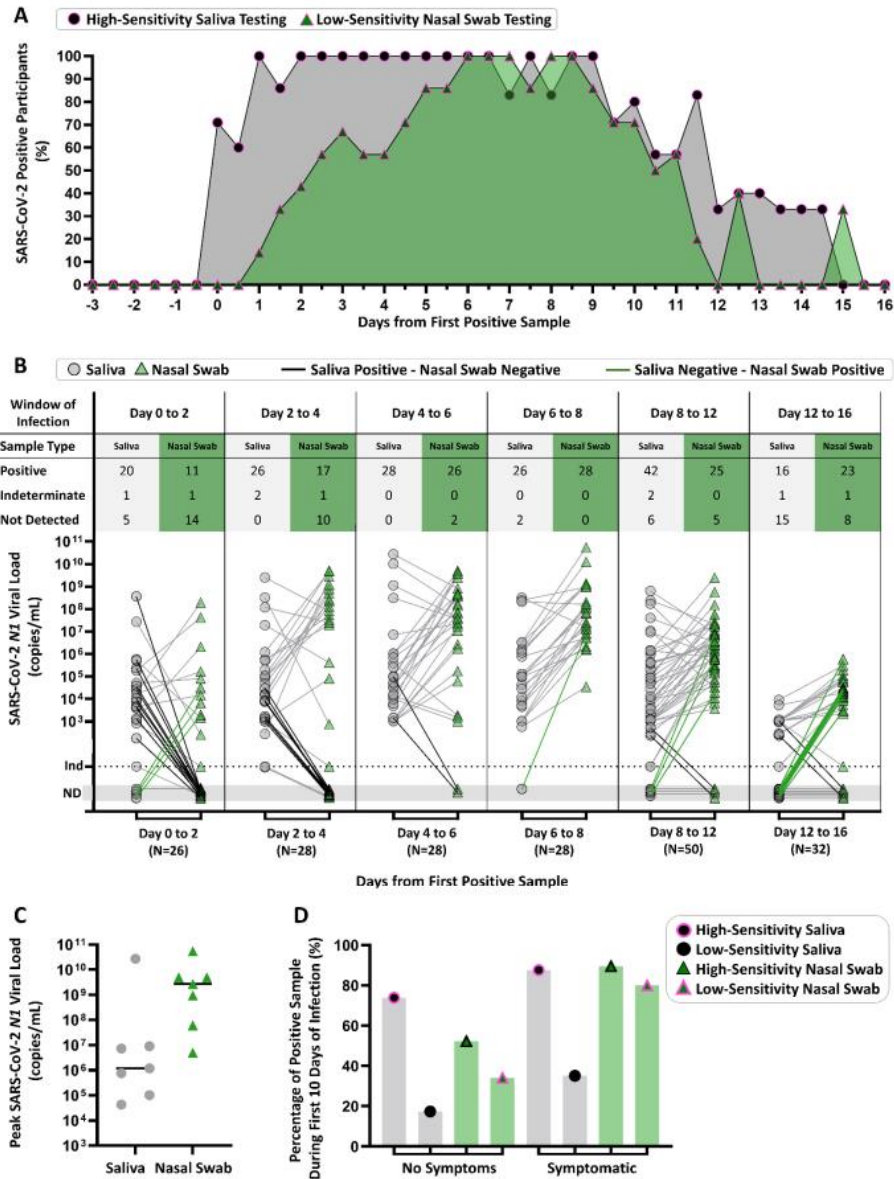


Figure 54. **Saliva versus nasal swabs performance for COVID-19 diagnosis.** (A) The performance of high-sensitivity saliva testing versus low sensitivity nasal swab testing for early diagnosis of COVID-19. (B) The viral loads of paired samples obtained at the different time courses of infection for saliva and nasal swab samples. Paired samples for a given time point are connected via a gray line. The black lines represent the situation where only saliva or nasal swab yielded a positive result. (C) The peak viral load of SARS-CoV-2 N1 measured in saliva and nasal swab samples for 7 patients. The horizontal black line is the median. (D) Percentage of positive samples during first 10 days of infection in high- and low- sensitivity saliva and high- and low- sensitivity nasal swab tests. The data indicate that high-sensitivity saliva testing outperforms the others. In all cases, day 0 represents the first positive test result in either saliva or nasal sample. In all cases, viral loads above the LOD threshold of 1.9×10^5 copy/mL was considered for low-sensitivity tests. Ref.¹⁰.

5.2.10. Conclusions and future outlook

Herein, we explained the working principles of major COVID-19 diagnostics tests, spanning from laboratory PCR testing to the rapid point of care testing, and reported their analytical and initial clinical performance. We further provided a comparison of the performance and suitability of different sample specimens for COVID-19 diagnosis. Significant works have been done so far, but future works are required to improve the performance of COVID-19 diagnostic tests and thereby assist mitigation of the pandemic. These works include: (i) Developing fast, cost-effective, and patient-friendly Ag-RDTs with high sensitivity. As mentioned previously, current Ag-RDTs are typically able to detect patients with a high viral load (i.e., > 10,000 copies/mL¹⁸²). Ag-RDTs with higher sensitivity capable of detecting patients with lower viral load (i.e., < 10,000 copies/mL¹⁸²) need to be developed and used in conjunction with (or in some cases instead of) NAATs to save time and cost as well as to reduce the need for accessing hospitals or clinics for testing¹⁷⁴. Furthermore, high-sensitivity Ag-RDTs compatible with saliva need to be developed as saliva offers patient comfort⁹, but requires a high sensitivity test for yielding true results¹⁸². Such saliva-based tests can potentially be used for children during a SARS-CoV-2 outbreak in schools⁹. One challenge is that saliva is a viscous solution and the viscosity can vary from person to person. Such a viscous solution may need preprocessing such as filtration and dilution for proper flow across the nitrocellulose membrane that is typically used in Ag-RDTs. Both filtration and dilution may compromise the test sensitivity. Hence, high sensitivity saliva-based tests can be a promising solution¹⁸². (ii) Developing efficient serologic tests. Serological tests can be used as a population-wide screening tool. The need for serological tests increases as we become closer

to the flattening phase of COVID-19. The issue with the current commercialized serological tests is that they do not possess high sensitivity and specificity. Developing highly specific antigens with high affinity is an essential step to improve the diagnostic accuracy of serologic tests¹²⁹. (iii) Developing advanced biosensors with fast response time and high sensitivity. Several interesting biosensors have been reported in the literature for COVID-19 diagnosis^{168,178}. The graphene-based biosensor developed by Ali et al. for detecting antibodies against SARS-CoV-2¹⁶⁸ and the field-effect, transistor-based biosensor developed by Seo et al. for detecting SARS-CoV-2 N protein¹⁷⁸ are two examples of such novel sensors. Pursuing these approaches can potentially assist it in progressing towards rapid, on-site COVID-19 diagnostics for past and ongoing infections.

6. BODY OF THE THESIS (METHODOLOGY AND RESEARCH FINDINGS)

6.1. Quantitative, sensitive ELISA enabled by a 3D-printed

microfluidic chain reaction capillaric circuit

Azim parandakh^{1,2}, Johan Renault^{1,2,#}, Will Jogia^{1,2,#}, Andy Ng^{1,2}, and David Juncker^{1,2,*}

¹Biomedical Engineering Department, McGill University, Montreal, QC, Canada

²McGill Genome Centre, McGill University, Montreal, QC, Canada

#Equal contribution. *Corresponding author

6.1.1. Abstract

Sandwich immunoassays such as enzyme-linked immunosorbent assay (ELISA) have been miniaturized and performed in a lab-on-a-chip format, but either depend on a computer or

complex peripherals to implement the multiple assays steps of conventional ELISA, or operate on simplified protocols without rinsing and with reduced performance as in the case of paper microfluidics and lateral flow assays. With the recent introduction of microfluidic chain reaction (MCR), complex fluidic operations can be structurally programmed in 3D printed capillarie circuits powered by capillary action. Here, we introduce the ELISA chip to pre-program the typical steps of an ELISA and execute them via an MCR. The ELISA chip was optimized and used for the quantification of the SARS-CoV-2 nucleocapsid protein in 4X-diluted saliva without the need for precise pipetting. Sample, reagents, and buffer were loaded into distinct inlets of the ELISA chip using disposable pipettes. Next, the ELISA chip generated 4 buffer aliquots (40, 60, 40, and 30 μL , respectively), and precisely metered the volumes of the sample (210 μL), detection antibody (70 μL), enzyme conjugate (50 μL), and substrate (80 μL), all stored in reservoirs. The user then click-connects a nitrocellulose strip integrated into a capillary-pump module to the reagent module, and the timed flow of the 9 solutions was executed step-by-step according to the progression of the MCR. A colored precipitate forming a line on a nitrocellulose strip served as an assay readout, and upon digitization, produced a calibration curve with a limit of detection of 54 and 91 pg/mL for buffer and diluted saliva, respectively. The ELISA chip is 3D-printed, modular, adaptable to other targets and assays, and could be used in the lab to automate ELISA, or at the point of care for diagnostic tests with both the performance of central laboratory ELISA and the convenience and form factor of rapid tests.

Keywords: ELISA; immunoassays; microfluidic chain reaction; capillarie circuits; capillary flow

6.1.2. Introduction

Enzyme-linked immunosorbent assay (ELISA) is utilized for the detection and quantification of proteins, antibodies, or antigens. Sandwich assays with both a capture antibody immobilized on the surface and a detection antibody applied in solution are used for assays requiring high sensitivity and specificity. Laboratory microplate ELISA is the gold standard and benefits from high sensitivity (down to sub-picomolar for the best antibody pairs) thanks to enzymatic signal amplification, quantitative results, standardized operations, consumables, and the use of 96-well plates, a comparably high throughput. Long incubation times and copious washing between different steps to reduce non-specific binding, thus assay background signal and achieve high sensitivity. However, ELISA suffers from several downsides, such as being laborious, lengthy (~2 -12 h depending on the protocol), requiring precise timing for each step, technical skills notably for adding and removing reagents (and thus susceptible to inter-operator variation), and a plate reader for signal readout¹.

The miniaturization and automation of ELISA have proceeded thanks to microfluidic lab-on-a-chip systems¹⁸³⁻¹⁸⁵. Such systems successfully reduced the consumption of reagents and the total assay time while preserving assay performance. However, whereas the chips are small, they rely on bulky peripherals such as syringe pumps¹⁸³ or control motors¹⁸⁴, and a computer or instrument¹⁸⁵ for operation. Passive microfluidic devices have been developed to address such limitations^{183,186}. For instance, a disk-like microfluidic platform (powered by centrifugal and capillary forces)¹⁸⁶ and a microfluidic siphon platform (powered by gravitational forces)¹⁸⁷ have been developed to carry out the common steps of a conventional

ELISA with reduced reagents consumption and assay time while preserving assay sensitivity. Yet, both require multiple precise pipetting steps and timed user interventions for operation. Sandwich assays can also be performed at point-of-care using so-called lateral flow assays (LFAs), also called rapid diagnostics, and are used globally for pregnancy tests and COVID-19 diagnosis. LFAs replace the enzyme amplification with colorimetric particles (either gold nanoparticles or polystyrene beads) that become visible to the naked eye upon accumulation. LFAs are simple to use as they only require the application of the sample, which flows thanks to capillarity without the need for peripherals, and produce a test result within a few minutes. However, LFAs offer only qualitative yes-no results, their sensitivity is typically lower compared to that of laboratory ELISA, and are not suitable for archival as the readout must be completed within a few minutes of the test because otherwise, the result can be compromised^{2,3}. Enzymatic amplification has been implemented in the LFAs, for instance by using a microfluidic interface, to improve sensitivity¹⁸⁸. Yet, they cannot implement various fluidic handling tasks of common ELISA such as timed incubation of reagents and multiple rinsing steps between each incubation interval.

Paper-based microfluidics has been developed to introduce more advanced fluidic functions such as sequential delivery, additional rinsing step, and as well as enzymatic amplification that collectively help improve assay sensitivity compared to LFAs¹⁸⁹. Sponge actuators that upon swelling connect or disconnect different parts of a paper-based microfluidic circuit, along with flow paths with different lengths and resistance, have been used to time the delivery of multiple reagents for completing a bona fide ELISA¹⁹⁰. However, these systems lacked the intermediate washing steps characteristic of classical ELISA, and undesired mixing

of consecutive reagents occur at their mutual interface. The potential for higher sensitivity assays may be limited by these shortcomings for instance enzyme-substrate mixing would be expected to contribute to non-specific signal amplification.

Capillarie circuits (CCs) are capillary microfluidics in microchannels designed and built using capillarie elements²⁸ which can automate liquid handling operations in a pre-programmed manner without the need for peripheral equipment. Multiple CCs have been designed to perform and automate ELISA, and while they often lack intermediate washing steps, they introduced flow reversal, timing and reagent lyophilization, and portable readers⁹⁸. In a CC, solutions are typically linked to one another through fluidic connections which increases the likelihood of reagents mixing due to diffusion and/or convection. Capillary burst valves have been implemented to reduce reagents premixing^{98,100}, but they cannot fully eliminate it. As mentioned earlier, any unwanted reagent crossover can increase assay background and reduce the signal-to-noise ratio.

Microfluidic chain reaction (MCR) can extend the number of capillary flow events that are being pre-programmed structurally within the CC¹². The MCR can execute an arbitrary number of sequential flow events thanks to local, conditional logic whereby event n is triggered after the preceding event $n-1$ has been completed, and completion of n , in turn, initiates event $n+1$. So-called capillary domino valves comprising an air link connecting two reservoirs encode the condition and provide a robust means of propagating sequential flow events¹². However, MCR and most CCs are susceptible to surfactants that reduce surface tension and contact angles. Yet surfactants are essential ingredients to assays, and often 0.05% Tween 20 is used to prevent non-specific binding¹³. In our previous MCR

demonstrations, we could only accommodate 0.0125% because higher concentrations led to corner flow and trapping of air bubbles¹⁷ and failure of stop valves.

User-friendliness is one of the critical features for a device to be used at the point of need, and precise aliquoting and metering are essential to reliable immunoassays. Whereas in the lab they can be met using precision pipettes operated by technicians, they are difficult to achieve in a point-of-care setting. Both ELISA and our MCR-CC introduced previously are dependent on precision pipetting. In particular, the MCR-CC required precise metering as an excess or a deficit in reagents could impair the functionality of the CC or lead to unwanted mixing. The recent COVID-19 rapid tests address the metering issue to a certain degree by requiring the user to deposit a precise number of droplets using a dropper which, although possible, necessitates detailed attention and is prone to occasional failure.

Here, we introduce the ELISA chip that automates ELISA protocol on a chip using an MCR CC while preserving the washing steps used in classical ELISA. The ELISA chip circumvents the need for precise pipetting thanks to automated aliquoting and metering of solutions and can accommodate high surfactant concentrations commonly used in immunoassays. We describe the circuitry and capillary elements for reagent aliquoting and metering, and further characterize the timing accuracy of MCR-controlled delivery of the reagents. As practical validation of the ELISA chip, we presented a COVID-19 antigen test to quantify the concentrations of SARS-CoV-2 nucleocapsid protein spiked in buffer and 4X-diluted human saliva using a scanner, and determined the limit of detection (LOD) for both sample types.

6.1.3. Results and discussion

6.1.3.1. ELISA chip fabrication and preparation

The detailed fabrication procedure of the ELISA chip and post-printing processes are explained in the “Experimental” section. In brief, the ELISA chip is rapid-prototyped using a transparent resin and stereolithography 3D printer with a printing duration of ~30 min. The post-printing preparations mainly included cleaning with isopropanol, curing with ultraviolet radiation, surface treating with oxygen plasma, and sealing the chip via a microfluidic diagnostic tape, with the total duration of ~30 min. The ~1 h duration from the printing procedure to the actual use of the chip renders our fabrication technique suitable for design iteration purposes which enabled us to print ~1200 chips for this work. Furthermore, in the developed ELISA chip, all capillary elements are implemented on the surface without any embedded features, thereby rendering the design potentially compatible with injection molding and mass production purposes.

6.1.3.2. ELISA chip design, operational mechanism, and workflow

Fig. 55 shows the overall workflow of the developed ELISA-on-chip platform. Upon addition of reagents, washing buffer, and sample (saliva in this case) at imprecise volumes using disposable pipettes to the ELISA chip, a sandwich ELISA is performed to generate a time-insensitive brown precipitate. The signal is then captured by a regular scanner for quantification purposes.

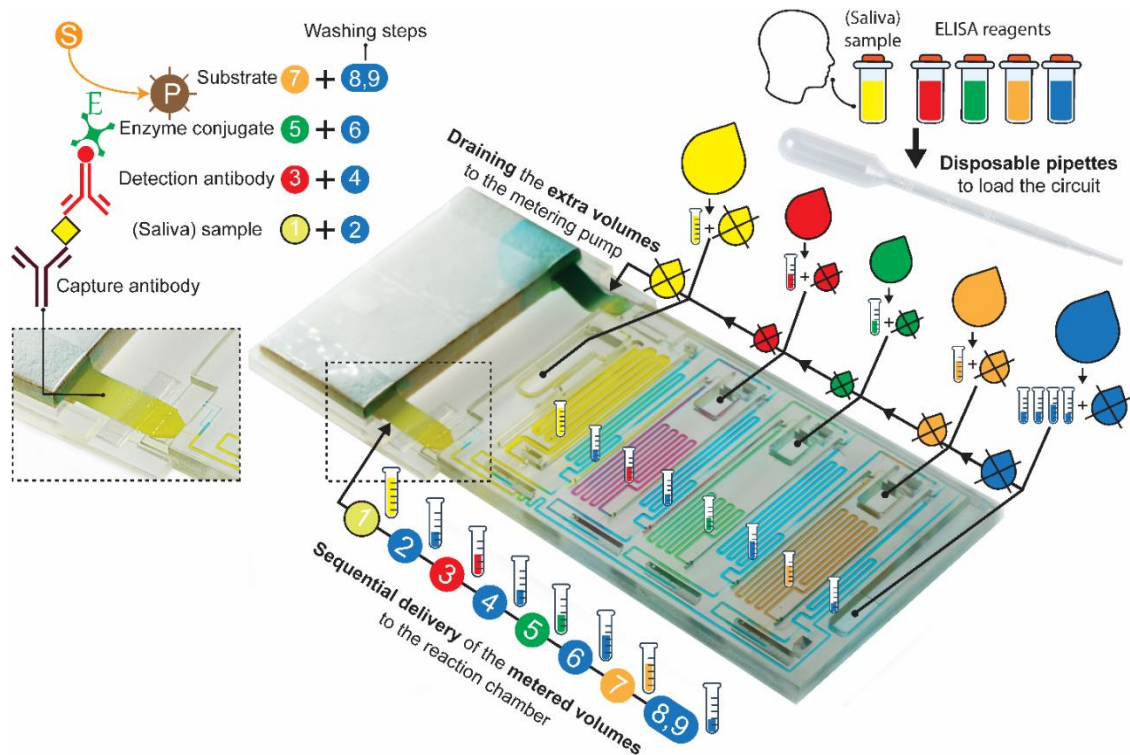


Figure 55. **The 3D-printed ELISA chip for SARS-CoV-2 nucleocapsid protein assay in saliva using an MCR-CC with superposed schematics of the various functions.** Reagents, washing buffer, and saliva sample are added to the chip using disposable, low-precision pipettes with visual feedback. The buffer is aliquoted into 4 reservoirs, and buffer and reagents are metered (schematized by graded graduated tubes), while excess reagents (crossed-out droplets) are drained into the capillary pump. Next, the sample, reagents, and buffer are sequentially flushed through the reaction chamber (a nitrocellulose strip within the dashed rectangle) step-by-step following the propagation of the MCR and completing the ELISA assay protocol. Enzymes bound to the strip following the assay, convert the substrate into a brown precipitate forming a permanent line that can be read out by eye, quantified following digitization, and serve as a record for archival.

The detailed fabrication procedure of the ELISA chip and post-printing processes are explained in the “Experimental” section. In brief, the ELISA chip is rapid-prototyped using a stereolithography 3D printer with a printing duration of ~30 min, followed by post-printing preparations mainly including cleaning with isopropanol, curing with ultraviolet radiation, surface treating with oxygen plasma, and sealing the chip via a microfluidic diagnostic tape, with the total duration of ~30 min. The ~1 h duration from the printing procedure to the actual use of the chip renders our fabrication technique suitable for design iteration purposes

which enabled us to print ~1200 chips for this work. Furthermore, in the developed ELISA chip, all capillarie elements are implemented on the surface without any embedded features, thereby rendering the design potentially compatible with injection molding and mass production purposes.

The schematic illustration of the developed ELISA chip is shown in Fig. 56. The ELISA chip mainly performs 3 liquid handling tasks: Aliquoting, metering, and sequential delivery. In what follows, the chip main compartments and step-by-step fluidic workflow are explained.

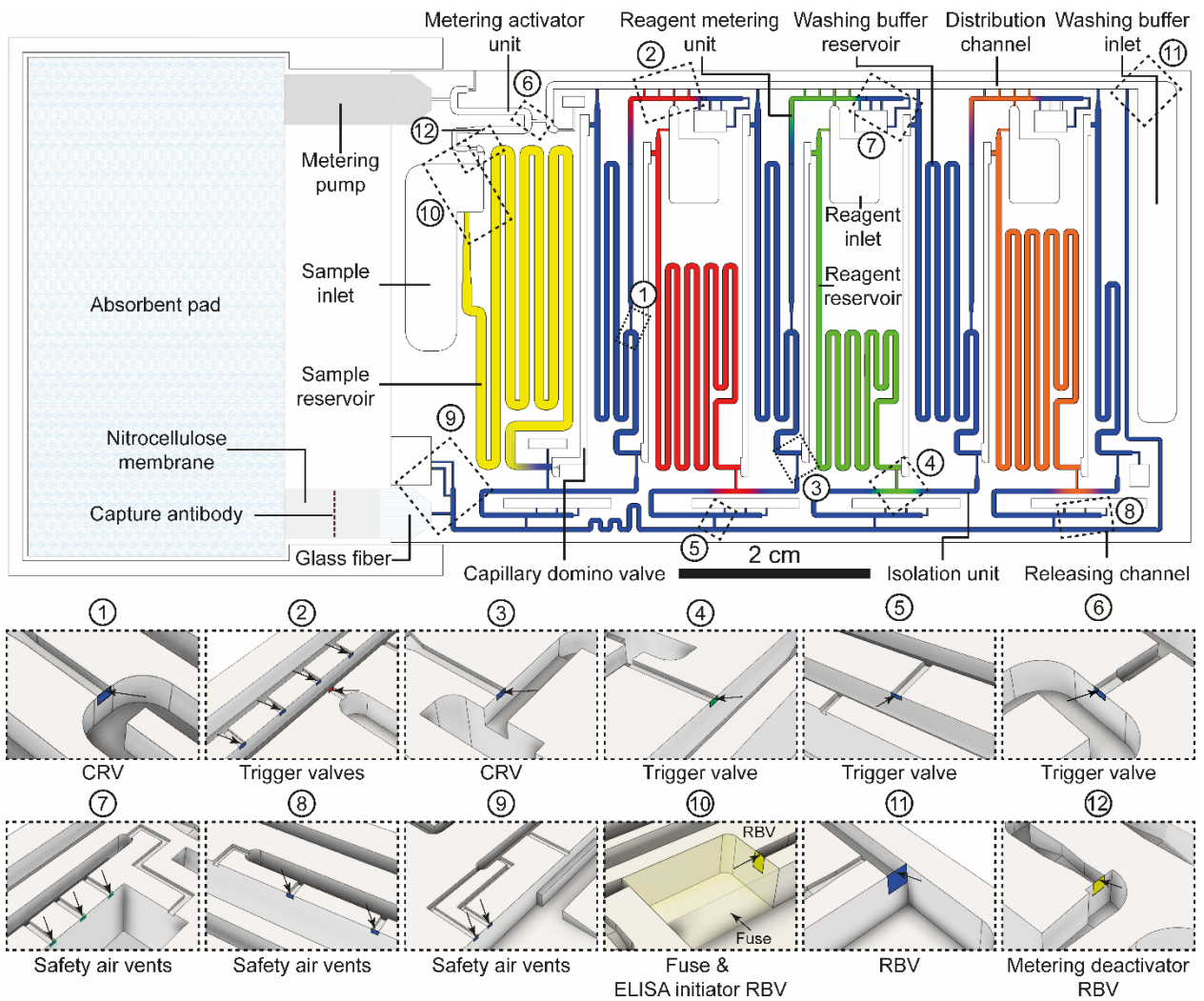


Figure 56. Schematic illustration of the developed ELISA chip. The ELISA chip enables instrument-free ELISA-on-chip and automates 3 main liquid handling tasks: Aliquoting, metering, and sequential delivery. The chip includes 8 MCRs (= 1 sample reservoir, 3 reagent reservoirs, and 4 washing buffer

reservoirs) connected via 7 capillary domino valves. A metering pump is implemented into the chip to drain the excess volumes of sample, reagents, and washing buffer, and thereby leave metered volumes of each solution for the sequential delivery session. The chip includes 3 reagent metering units that guide the excess volumes to drain to the metering pump without any unwanted mixing of solutions. The ELISA chip is further equipped with 4 isolation units to avoid unwanted premixing of solutions during aliquoting, metering, and sequential delivery sessions. The reaction chamber includes a nitrocellulose membrane inkjet spotted with the capture antibody. The nitrocellulose membrane is connected to an absorbent pad from the back end to wick the extra volumes of solutions after passing the reaction chamber, and to a glass fiber conjugation pad from the front end to facilitate connection to the chip.

6.1.3.2.1. ELISA chip workflow: Aliquoting session

The ELISA chip allowed for the implementation of enzymatic amplification (i.e. streptavidin-polyHRP followed by DAB) in the assay platform as different reagents can be loaded onto the chip in separate reservoirs and sequentially delivered to the reaction chamber once needed.

The ELISA chip consists of 3 reagent reservoirs and inlets allocated for the detection antibody, enzyme (i.e. streptavidin-polyHRP), and substrate (i.e. DAB) (Fig. 56). The encoded aliquoting and metering features on the chip relax the loading process by obviating the need for a laboratory micropipette and allowing for the use of a disposable pipette to load the reagents, washing buffer, and sample to the chip.

In the first step, reagents need to be loaded into the chip. Upon adding an imprecise volume of the reagents, using disposable pipettes, at an arbitrary order to the reagent inlets, a pre-programmed volume (70, 50, and 80 μL for the detection antibody, streptavidin-polyHRP, and DAB respectively) occupies the designated reservoirs and the rest is kept in the reagent inlets to be drained subsequently by the metering pump (Fig. 57A). The filling time of each reagent reservoir is depicted in Fig. 58.

Secondly, the washing buffer needs to be loaded into the chip. The chip includes 1 washing buffer inlet, 1 distribution channel ($\sim 37.5 \mu\text{L}$), 1 releasing channel ($\sim 29.0 \mu\text{L}$), 4 washing buffer

reservoirs (20.0, 60.0, 40.0, and 40.0 μL), 3 “reagent metering units” (RMUs) (~ 10.0 μL each), and 4 isolation units (~ 8.0 - 9.5 μL each) (Fig. 56). As illustrated in Fig. 56, the RMUs extend from the washing buffer serpentine via a capillary retention valve (CRV) (Fig. 55, close up #1) and connect the reagent inlets to the distribution channel to create a fluidic path from the reagent inlets to the metering pump. This connection is realized by 1 trigger valve between the RMU and the corresponding reagent inlet and 4 trigger valves between the RMU and the distribution channel (Fig. 56, close up #2). The isolation units extend from the end of washing buffer serpentine via one CRV (Fig. 56, close up #3) and are connected to the reagent (or sample) reservoirs via one trigger valve (Fig. 56, close up #4) and to the releasing channel via another trigger valve (Fig. 56, close up #5). The isolation channels create a space for the reagents (or the sample) to mix with the washing buffer, thereby preventing the unwanted mixing of reagents or the sample with one another.

Introducing an imprecise volume of the washing buffer to the washing buffer inlet fills the distribution channel and aliquots the washing buffer into the washing buffer reservoirs, RMUs, isolation units, and releasing channel (Fig. 57B) (filling time: 1.47 ± 0.10 min; Fig. 58). At the end of the distribution channel, a trigger valve is implemented which connects the distribution channel to the metering activator unit (MAU) (Fig. 56, close up #6). The MAU is connected to the metering pump and carries out the task of activating/deactivating the metering pump once filled/emptied. This trigger valve avoids filling the MAU at this step to remain the metering pump deactivated. Hence aliquoting of the washing buffer is realized first whereas metering of the excess volumes is realized at the next step once the MAU is filled and therefore the metering pump is activated (Fig. 57C).

Tween 20 is an essential constituent of the ELISA wash buffer. It primarily functions to reduce background staining and improve the signal-to-noise ratio. The typical concentration of Tween 20 in the ELISA buffer is 0.05%¹³. But, a solution with this level of Tween 20 has low surface tension posing a strong edge flow effect in a capillary-driven microfluidic chip and increasing the likelihood of bubble formation. To avoid bubble formation, air vents can be used¹⁷. Air vents are typically located at the end of a microchannel to ensure proper filling of the entire channel without any bubble formation. But, when the effect of edge flow is strong, the liquid tends to progress rapidly through the walls of a microchannel and accumulate at the end, which may subsequently fill the air vent located at the end of the channel. To tackle this issue, we implemented additional air vents – which we call “safety” air vents - in several locations of the developed ELISA chip. As an example, each RMU and isolation unit is equipped with 3 and 2 safety air vents respectively to ensure proper filling. These safety air vents are located far from the end of the microchannel to hamper the edge flow to fill them precedent to the bulk flow (Fig. 56, close up #7,8).

In another design configuration, safety air vents can be implemented at the end of a microchannel to ensure proper filling of a crossing microchannel located far from the end. For instance, 2 safety air vents are implemented at the end of the releasing channel to ensure proper filling of the outlet located far from the end of the channel (Fig. 56, close up #9). In the developed MCR CC, 22 safety air vents (both types combined) were implemented to ensure proper fluidic functionality of the chip in the case of bubble formation. Fig. 62 illustrates the safety air vents at the RMUs, isolation units, and releasing channel when the ELISA buffer or Mili-Q water (both colored with food dye for visualization purposes) was used

to fill the circuit. In the case of ELISA buffer, the strong effect of edge flow may lead to bubble formation at the channel end, but the circuit fluidic functionality is rendered secure due to the presence of safety air vents. In the case of Mili-Q water, the effect of edge flow is not significant and the presence of safety air vents is not essential. As shown in Fig. 62, the entire channel is filled completely without any bubble formation.

Thirdly, the saliva sample needs to be loaded to the chip. The chip consists of 1 sample inlet that branches into the sample reservoir (~210 μL) and the MAU (~11.7 μL). The collected saliva specimen first needs to be filtered and then loaded to the chip. Introducing an imprecise volume of the sample to the sample inlet aliquots the sample into the MAU (Fig. 57C) and the sample reservoir (Fig. 57D) (filling time: 1.09 ± 0.13 min; Fig. 58). Once the MAU is filled, the metering pump becomes activated, and the metering process therefore starts.

6.1.3.2.2. ELISA chip workflow: Metering session

The metering pump wicks only the excess volumes of the sample, reagents, and washing buffer (Fig. 57E), and to accomplish this, various design features are implemented into the developed ELISA chip.

A CRV is implemented at the beginning of each reagent and washing buffer reservoir, and a retention burst valve (RBV) called “ELISA initiator RBV” (Fig. 56, close up #10) is implemented at the beginning of the sample reservoir to hold the liquid during the whole metering session.

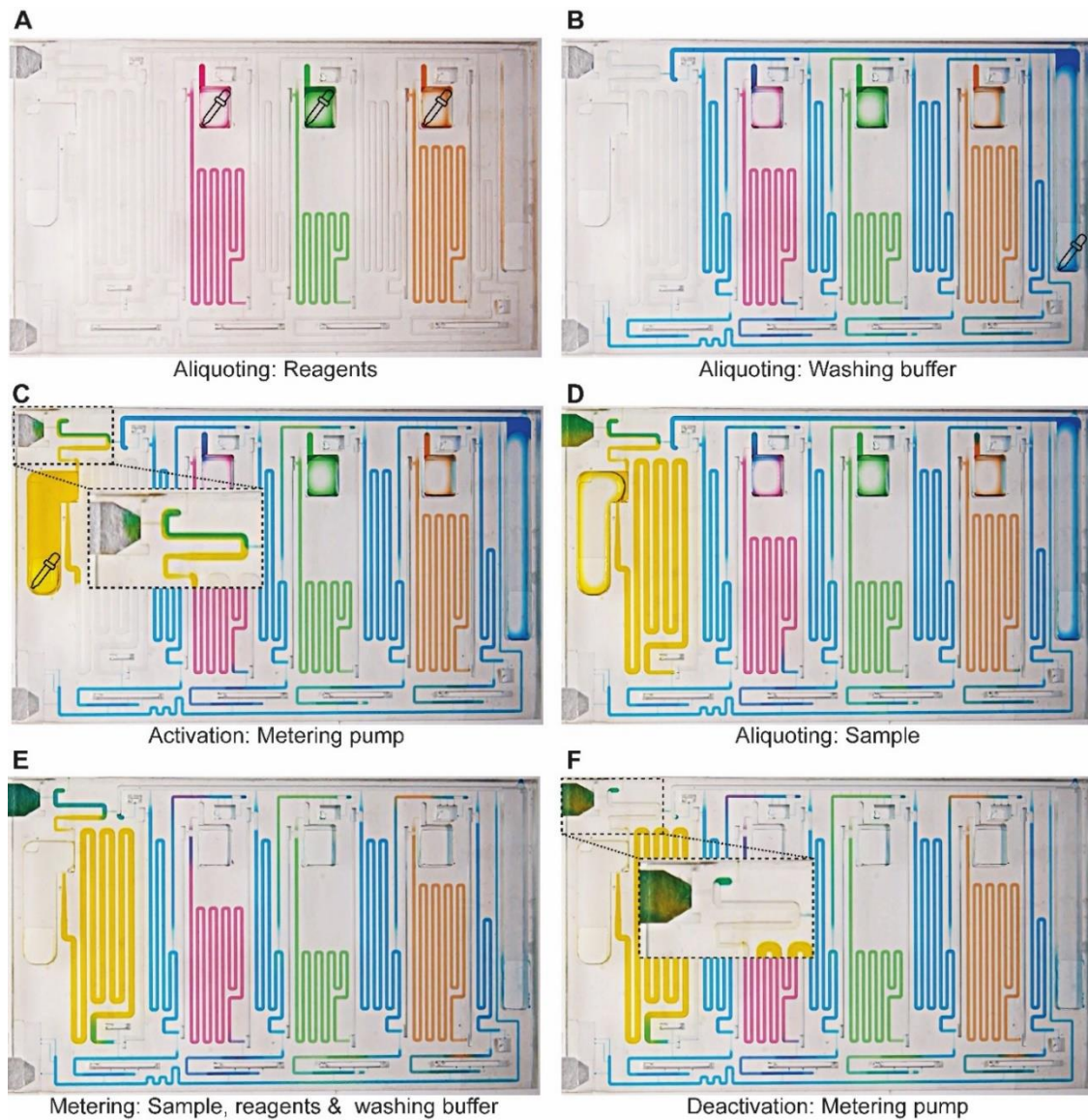


Figure 57. **Step-by-step fluidic workflow of the developed ELISA chip for aliquoting and metering sessions.** (A) Adding the reagents at imprecise volumes, using disposable pipettes, and arbitrary order fills the reagent reservoirs with a preprogrammed volume while the excess is kept in the reagent inlets to be drained subsequently. (B) Adding the washing buffer at an imprecise volume, using a disposable pipette, fills the washing buffer reservoirs, reagent metering units (RMU), isolation units, and the releasing channel while the excess is kept in the distribution channel and the washing buffer inlet to be drained subsequently. (C) Adding (saliva) sample to chip, using a disposable pipette, fills the metering activator unit (MAU) to activate the metering pump, and (D) the sample reservoir while the excess is kept in the sample inlet to be drained subsequently. (E) The excess volumes of sample, reagents, and washing buffer are drained via the metering pump, leaving a preprogrammed volume for each solution. (F) The deactivator RBV then bursts to empty the MAU and therefore deactivate the metering pump.

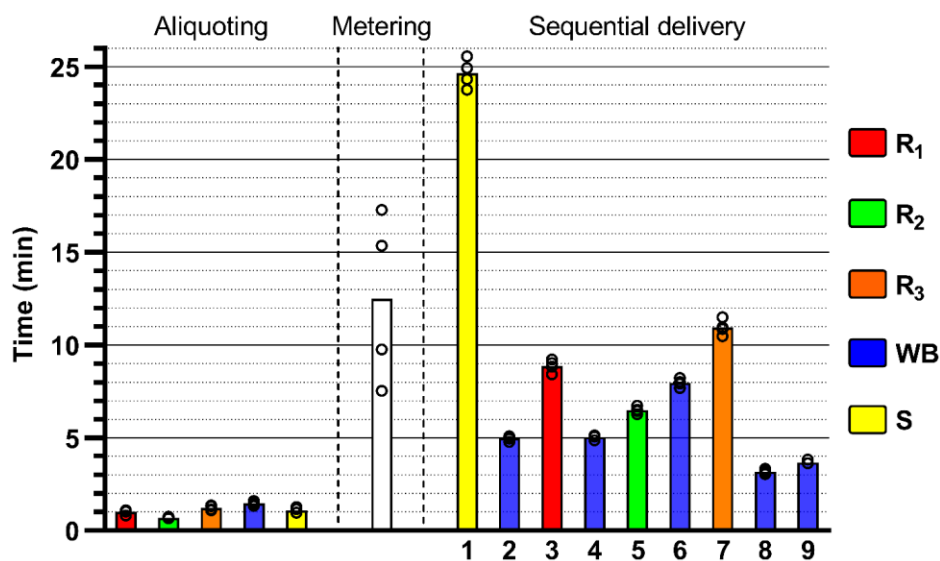


Figure 58. **Duration of the fluidic operation of the developed ELISA chip in aliquoting, metering, and sequential delivery sessions.** In the sequential delivery session, the numbers (1, 2, ..., 9) indicate the sequence of delivery to the reaction chamber. The circles represent replicates (n=4) of each data point. R1, R2, R3, WB, and S stand for 1st reagent, 2nd reagent, 3rd reagent, washing buffer, and sample, respectively.

One metering path for draining the excess volumes to the metering pump is the one from the releasing channel to the sample reservoir and then to the MAU (path “i”: releasing channel → sample reservoir → MAU → metering pump) (Fig. 63). The draining path “i” is not desirable as it would result in the draining (and subsequently unwanted mixing) of the reagents into the releasing channel as well as the arbitrary loss of sample in the sample reservoir. To disable the metering path “i” from the circuit, the end section of the sample inlet that is connected to the MAU and the ELISA initiator RBV acts as a “fuse” element to entirely cut the fluidic path from the sample reservoir to the MAU (sample reservoir → MAU) (Fig. 56, close up #10). During the metering session, this fuse element is among the first elements to drain as it is designed to have a very low capillary pressure. When drained completely, the fuse disconnects the fluidic path from the sample reservoir to the MAU (sample reservoir → MAU),

thereby disabling the fluidic path “i” from the circuit. It should also be noted that draining this fuse element yields in the metering of the sample.

The desired path for the draining of the excess volumes of the reagents to the metering pump is reagent inlet → RMU → distribution channel → MAU → metering pump (path “ii”) (Fig. 63).

Two other paths (although undesirable) exist for this purpose: reagent inlet → RMU → washing buffer reservoir → distribution channel → MAU → metering pump (path “iii”) and reagent inlet → reagent reservoir → isolation unit → washing buffer reservoir → distribution channel → MAU → metering pump (path “iv”) (Fig. 63). To disable the draining path “iii”, the resistance of this path was maximized by increasing the resistance of the CRV connecting each RMU and the respective washing buffer reservoir (Fig. 56, close up #1). To disable the draining path “iv”, the resistance of this path was maximized by increasing the resistance of the CRV connecting each isolation unit and the respective washing buffer reservoir (Fig. 56, close up #3). To maximize the draining process through the draining path “ii”, the resistance of this path was minimized by implementing 4 trigger valves between each RMU and the distribution channel and minimizing the resistance of the trigger valve between each reagent inlet and RMU (Fig. 56, close up #2).

The excess volume of the washing buffer drains to the metering pump through path “v” which is washing buffer inlet → distribution channel → MAU → metering pump (Fig. 63). An RBV is implemented at the beginning of the distribution channel (Fig. 56, close up #11) to hold the liquid during the reagents’ metering session. When the extra volumes of the reagents and washing buffer in the washing buffer inlet are drained to the metering pump, the distribution

channel drains. The distribution channel at this step acts as a fuse element and by draining leaves a metered volume of washing buffer in the washing buffer reservoirs. Once the sample, reagents, and washing buffer are metered, the MAU is required to drain to disconnect the metering pump and therefore end the metering process. To this end, a “deactivator RBV” is implemented at the beginning of the MAU which carries out the task of emptying the MAU and thus deactivating the metering pump (Fig. 56 close up #12 & Fig. 57E,F). The duration of the metering session depends on the initial volumes that are loaded to the chip. The larger the extra volumes are, the longer the metering session is. Fig. 58 illustrates the metering duration for 4 ELISA chips loaded with imprecise volumes of sample, reagents, and washing buffer (metering duration: 12.48 ± 3.97 min).

We further characterized the metering functionality of the developed ELISA chip. We investigated the range that the ELISA chip can operate to precisely meter sample, reagents, and washing buffer without any fluidic malfunctions (Fig. 59). As an example, in the case of the detection antibody (i.e., R_1), 70 μL (indicated as the metered volume) is required to be delivered to the reaction chamber for the ELISA, and the metering range that the chip can function intactly is 71 – 110 μL . If less than 71 μL is loaded to the detection antibody inlet, the corresponding reservoir may not fill completely. If more than 110 μL is loaded, part of the extra volume may enter the washing buffer reservoir precedent or next to the detection antibody reservoir, thereby imposing variations in delivering the pre-programmed volumes to the reaction chamber for ELISA-on-chip. Fig. 64 illustrates a case in which 140 μL of the detection antibody (=70 μL of extra) is loaded onto the detection antibody inlet. As shown, an extra volume of the detection antibody entered the precedent washing buffer reservoir.

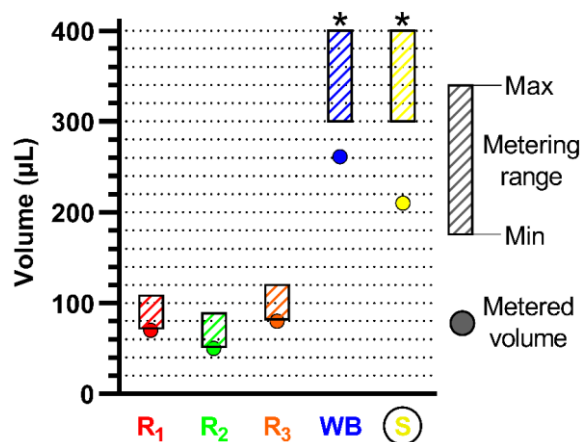


Figure 59. **Metering characterization of the developed ELISA chip.** Metered volumes and the corresponding metering range are indicated by dots and dashed rectangles, respectively. The metered volume indicates the volume that is required to be used for the ELISA-on-chip. The metering range indicates the minimum and maximum volumes of the sample, reagents, and washing buffer that can be loaded to the chip to precisely achieve the metered volume. R₁, R₂, R₃, WB, and S stand for 1st reagent, 2nd reagent, 3rd reagent, washing buffer, and sample, respectively. * indicates the maximum volume tested.

6.1.3.2.3. ELISA chip workflow: Sequential delivery session

The last step includes connecting the main pump to the chip. The main pump which also serves as the reaction chamber includes a strip of nitrocellulose membrane inkjet spotted with capture antibody (i.e. mouse monoclonal antibodies with affinity to the nucleocapsid protein of SARS-CoV-2). The membrane is connected to an absorbent pad from the back end and to a glass fiber conjugation pad from the front end to ease the connection to the chip (Fig. 56). Once the main pump is click-connected to the chip (Fig. 59A), the ELISA initiator RBV starts to burst to trigger timed, step-by-step sequential delivery of the sample, reagents, and the corresponding washes to the reaction chamber (Fig. 60B-F) (movie S1). The duration of each draining step is illustrated in Fig. 58.

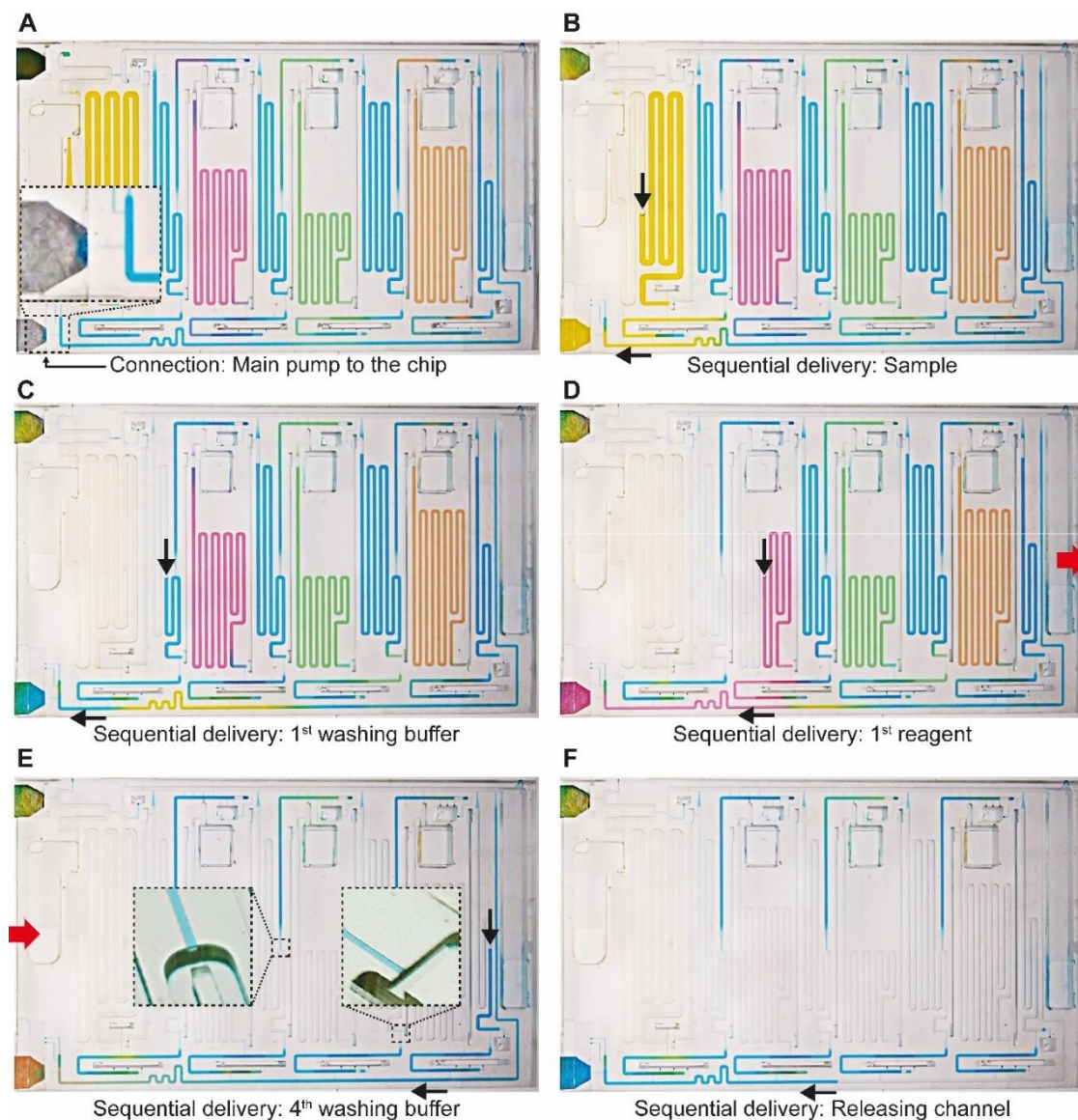


Figure 60. **Step-by-step fluidic workflow of the developed ELISA chip for the sequential delivery session.** (A) Connecting the main pump to the circuit triggers (B-F) sequential delivery of the sample, reagents, and corresponding washes to the reaction chamber. Black arrows indicate the direction of flow. As illustrated in panel E, the capillary retention valve implemented at the intersection of the RMUs/isolation units and the corresponding washing buffer serpentine avoids their drainage during the sequential draining session.

In the developed ELISA chip, sequential delivery is powered by the concept of MCR and realized by a capillary element called the capillary domino valve. The sample, reagent, and washing buffer reservoirs are serially chained to one another through 7 capillary domino

valves to realize 8 sequential deliveries. Draining of the releasing channel at the last step is executed via a regular RBV, and not by MCR, due to space limitations on the chip. A detailed explanation of the operational mechanism of MCR and capillary domino valve is provided in our previous publication. Briefly, complete drainage of the sample solution opens the air link and exposes the next reservoir, i.e. 1st washing buffer reservoir, to the atmospheric pressure to trigger its drainage. Likewise, complete drainage of the 1st washing buffer reservoir triggers drainage of detection antibody solution and so on¹². During the sequential delivery session, the RMUs and isolation units do not drain. This is realized by implementing a CRV at the intersection of each RMU/isolation unit and the corresponding washing buffer reservoir (Fig. 56, close up #1,3). The CRVs are encoded to hold the liquid during the entire sequential delivery session and therefore to avoid draining of RMUs/isolation units to the reaction chamber (Fig. 60E,F).

6.1.3.3. COVID-19 antigen assay

Saliva, as a minimally invasive and patient-friendly sample specimen, contains SARS-CoV-2 viral particles and is a promising sampling site for COVID-19 diagnosis⁸. To yield the most reliable result, however, saliva-based tests should possess a high sensitivity¹⁰. To this end, as a demonstration of the application, here we developed and optimized a highly-sensitive, saliva-based COVID-19 antigen assay via the ELISA chip. The major optimization factors are included in Table 3. To investigate the performance of the COVID-19 antigen test-on-ELISA chip, we spiked different concentrations of nucleocapsid protein of SARS-CoV-2 (0, 1, ..., 10⁶ pg/mL) in 4X-diluted pooled human saliva and ELISA buffer. The developed ELISA was colorimetric yielding a time-insensitive brown precipitate, formed by DAB oxidization in the

presence of HRP, and the signal quantitation for the calibration curve generation was simply achievable using a regular scanner. Fitting the experimental data using a 4-parameter logistic regression, the assay indicated the LOD of 91 pg/mL and 54 pg/mL for the nucleocapsid protein spiked in ELISA buffer and 4X-diluted pooled saliva, respectively (Fig. 61). The small dilution of human saliva together with the high sensitivity of the assay, both enabled by the ELISA chip, is a practical advantage of the developed platform given the high-sensitivity requirement of saliva-based tests.

Table 3. Major optimization factors for the developed COVID-19 antigen assay.

Optimization	Range tested	Final condition
Capturing antibody	0.07 - 0.28 μ g	0.28 per membrane
Detection antibody	5 - 20 μ g/mL	7.5 μ g/mL
Streptavidin-pHRP	5 - 20 μ g/mL	7.5 μ g/mL
Signal development	Streptavidin-pHRP & DAB vs. gold nanoparticles (or nanoshells)	Streptavidin-pHRP
Saliva dilution	1X, 2X, 4X, 10X	4X

The LOD obtained by the ELISA chip falls in the range of microplate ELISA. The serum-based SARS-CoV-2 nucleocapsid detection ELISA kits by SinoBiological, Inc. (catalog number: KIT40588) and RayBiotch Life, Inc. (catalog number: ELV-COVID19N) with a microplate-based format and operational time of ~5 hr have been reported to have the LOD of 34.61 pg/mL and 0.07 ng/mL (= 70 pg/mL), respectively. Our saliva-based COVID-19 antigen assay enabled by the ELISA chip indicates a comparable level of assay sensitivity while (i) being significantly faster, (ii) consuming less reagents, (iii) utilizing minimal laboratory tools and equipment, and (iv) requiring remarkably fewer user interventions. It should also be noted that our experimental design imposed a more conservative LOD determination protocol as the blank sample was designed to be 4X-diluted human saliva with zero antigen concentration. Such a

blank sample is a better representative of the patient matrix sample compared to that of commercially available ELISA kits which is typically the dilutant buffer.

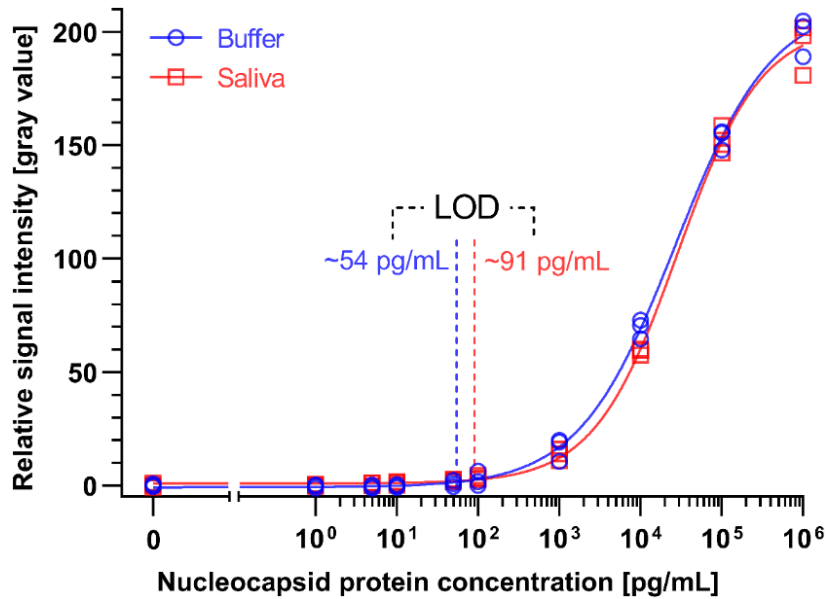


Figure 61. **Calibration curves of the COVID-19 antigen assay-on-ELISA chip.** Different concentrations of SARS-CoV-2 nucleocapsid protein were spiked in ELISA buffer or 4X-diluted pooled saliva. The resultant time-insensitive colorimetric signals were then captured by a regular scanner and analyzed to obtain the calibration curves via 4-parameter logistic regression. The number of replicates for each concentration is 3 for both calibration curves. R-squared for buffer and saliva respectively are 0.998 and 0.997.

The study by Corman et al. investigated the detection performance of seven rapid antigen point of care tests: (i) the Abbott Panbio COVID-19 Ag Rapid Test, (ii) the RapiGEN BIOCREDIT COVID-19 Ag, (iii) the Healgen Coronavirus Ag Rapid Test Cassette (Swab), (iv) the Coris BioConcept COVID-19 Ag Respi-Strip, (v) the R-Biopharm RIDA QUICK SARS-CoV-2 Antigen, (vi) the nal von Minden NADAL COVID-19 Ag Test, and (vii) the Roche-SD Biosensor SARS-CoV Rapid Antigen Test. The best performance was attributed to the R-Biopharm antigen test with the detection level of 2.5 ng/mL (= 2,500 pg/mL) for nucleocapsid protein spiked in phosphate buffer saline¹⁷⁵. In ELISA buffer and 4X-diluted pooled saliva, our COVID-19 antigen assay

enabled by the ELISA chip outperforms these detection levels by ~50 and ~25 times, respectively.

6.1.4. Conclusions and future works

In this study, we developed an instrument-free ELISA chip powered by MCR for sensitive, quantitative immunoassays. The developed ELISA chip is 3D printed with all features on the surface (i.e., no embedded features) to render the design potentially compatible with injection molding and mass production purposes. The aliquoting and metering features encoded on the ELISA chip allow for the use of disposable pipettes to load the circuit, thereby minimizing the use of laboratory equipment such as precision micropipettes and rendering the device more user-friendly. The ELISA chip further allows for the use of solutions with low surface tension, as is the case for the laboratory ELISA's buffer, without any fluidic malfunctions. As a demonstration of the application, a quantitative, saliva-based COVID-19 antigen assay is presented for the detection of nucleocapsid protein of SARS-CoV-2. The assay generates a time-insensitive brown precipitate which obviates the need for signal readout at an accurate time frame, thereby rendering the assay applicable for archival purposes. In the case of analytical performance, the assay indicates a LOD of 54 and 91 pg/mL for ELISA buffer and 4X-diluted saliva, respectively. This level of analytical performance is comparable to that of laboratory microplate ELISA and outperforms the commercially lateral flow antigen tests by ~25 and ~50 times for saliva and ELISA buffer, respectively. The small dilution of saliva in conjunction with the high sensitivity of the assay, both enabled by the ELISA chip, render the developed microfluidic platform a practical and high-performance diagnostic tool outside sophisticated laboratory equipment in resource-limited settings.

Future works can include reducing the number of user interventions. For this purpose, reagents need to be dried on the circuit, followed by implementing respective reconstitution modules for effective rehydration of the predried reagents^{98,107}. Sample can be loaded to the chip and one-step loading of washing buffer can then fill washing buffer reservoirs while simultaneously reconstituting the reagents. The manual connection of the main pump to the circuit can be removed by implementing appropriate capillarie elements, e.g. flow resistance, fuse, etc. onto the circuit to reduce the number of manual steps from 6 to 2.

Another point of improvement is to reduce the operational time of the device. The presented ELISA chip possesses a total operational time of ~1.5 hr which is a significant improvement to laboratory ELISA with a typical assay time of 2 -24 h (depending on the protocol), but yet could be further improved particularly for point of care applications. Implementing dried reagents and reconstitution modules to the ELISA chip would reduce the duration of the metering session as there will be no excess volume of the reagents to be drained by the metering pump. The duration of the sequential delivery session can also be reduced by changing the sensor type. In the presented assay platform, the speed of the sequential delivery session is mainly limited to the wicking rate of the nitrocellulose membrane. The assay analytical performance is another limiting factor as a faster flow rate is inversely proportional to the assay sensitivity. New types of sensors such as chemiluminescence⁹⁸ or electrochemical¹⁶⁸ with a faster response time can potentially be implemented (and if possible, fully integrated) into the ELISA chip to reduce assay time without sacrificing analytical performance.

6.1.5. Experimental

6.1.5.1. ELISA chip fabrication and preparation

The chips were designed in AutoCAD (Autodesk), exported as “STL” files, and printed with a stereolithography 3D printer (Prime 110, Creative CADworks, Toronto, Canada) using a monocure 3D rapid clear resin (Monocure 3D, NSW, Australia) with the following printing parameters: exposure time per layer: 1.2 sec (12 sec for base layer); transitions buffer layers: 2; layer thickness: 20 µm; printing delay: 1 min; and gap adjustment: 0.1 mm. Once printed, the chips were cleaned with isopropanol (Fisher Scientific, Saint-Laurent, Quebec, Canada), dried with high pressurized nitrogen gas, ultraviolet cured for 1 min, oxygen plasma treated for 10 sec at 100% power (PE50 plasma chamber, Plasma Etch, Carson City, USA), and sealed with a microfluidic diagnostic tape (catalog number: 9795R; 3M Science. Applied to Life™, Ontario, Canada).

To construct the metering pump, a strip of Whatman CF4 paper (Cytiva, Marlborough, Massachusetts, United States) was clamped between 2 absorbent pads from the back end (Electrophoresis and Blotting Paper, Grade 238, Ahlstrom-Munksjo Chromatography, Helsinki, Finland) to serve as a capillary pump. For the reaction chamber, a strip of Vivid™ 120 lateral flow nitrocellulose membrane (Catalog number: VIV1202503R; Pall Corporation, Port Washington, USA) was clamped between the same absorbent pads from the back end and to a G041 glass fiber conjugate pad (Millipore Sigma, Oakville, Ontario, Canada) from the front end to facilitate connection to the chip.

6.1.5.2. COVID-19 antigen assay

Vivid™ 120 lateral flow nitrocellulose membranes were designed in Autocad and cut into 5.2 mm wide strips using the Silhouette Portrait paper cutter (Silhouette, Lindon, USA). Membranes were stripped with a 5 mm-wide test line of SARS-CoV-2 nucleocapsid protein mouse antibody (catalog number: 40143-MM08; Sino Biological, Inc., Beijing, China) at the concentration of 1 mg/mL and a 5 mm-wide control line of BSA-biotin solution at the concentration of 50 µg/mL delivered using a programmable inkjet spotter (sciFLEXARRAYER SX, Scienion, Berlin, Germany). Next, the membranes were dried for 1 h at 37 °C, and blocked by dipping into a blocking buffer solution (1% BSA and 0.1% Tween20 in PBS) until completely wet, and shaking on a rocker for 60 min at 75 rpm. The membranes were then retrieved, incubated for 1 h at 37 °C to be dried, and stored with a desiccant at 4 °C until use on the next day.

The sample solutions were prepared by spiking SARS-CoV-2 nucleocapsid protein (catalog number: 40588-V08B; Sino Biological, Inc., Beijing, China) at the concentration of 0 - 10⁶ pg/mL in either the ELISA buffer solution (0.1% BSA and 0.05% Tween20 in PBS) or 4X-diluted pooled saliva solution. To prepare the 4X-diluted pooled saliva solution, fresh saliva specimens were first obtained from 2 individuals via oral cotton swabs (Salivette, Sarstedt, Numbrecht, Germany). They were then pooled, diluted by a factor of 4 in the ELISA buffer solution, filtered through a 0.22-micron filter, kept in the cold room (~4 °C) until use the same day. The biotinylated SARS-CoV-2 nucleocapsid protein rabbit antibody (catalog number: 40143-R004-B; Sino Biological, Inc., Beijing, China) and Pierce™ streptavidin-polyHRP (catalog number: 21140; ThermoFisher, Ottawa, Canada) solutions were prepared in an ELISA buffer

solution (both with the concentration of 7.5 µg/mL). The substrate solution was prepared by dissolving SIGMAFAST™ DAB tablets (catalog number: D4293-50SET; Sigma-Aldrich, Oakville, Canada) in Mili-Q water. The washing buffer solution was the same as the ELISA buffer solution.

6.1.5.3. Nitrocellulose membrane image analysis and LOD calculation

The nitrocellulose strips were removed from the ELISA chip, left to dry at room temperature, and scanned at 1200 dpi (Epson Perfection V600). The scanned images were then analyzed in Fiji to measure the gray value of the test line as well as the local backgrounds located 30 pixels above and below the test lines. The local signal intensity of the test line was calculated by subtracting the gray value of the test line from the average of the gray value of the top and bottom local backgrounds. The relative signal intensity for each case was then calculated by subtracting the local signal intensity of the test line from the average of the local signal intensity of the negative controls.

The experimental data were fitted using a 4-parameter logistic regression with the following equation¹⁹¹:

$$y = d + \frac{a - d}{1 + \left(\frac{x}{c}\right)^b} \quad (12)$$

Where a and d are theoretical responses at zero and infinity, respectively, b denotes the slope factor (i.e., Hill slope), and c represents the mid-point concentration (inflection point)¹⁹¹.

The LOD was then determined by substituting y with 3 times of standard deviation of the blank (i.e., sample with zero antigen concentration) and solving the above equation for x as follows:

$$\text{LOD} = c \left(\left(\frac{a - d}{3 * \text{SD}_{\text{blank}} - d} \right) - 1 \right)^{\frac{1}{b}} \quad (13)$$

6.1.5.4. ELISA chip video recording and image capturing

To represent the fluidic workflow, unless otherwise stated, the MCR CCs were loaded with the ELISA buffer solution in the reagents and washing buffer reservoirs and with the 4X-diluted pooled saliva solution in the sample reservoir. Both solutions were colored with food dye for visualization purposes.

The videos were recorded via a Panasonic Lumix DMC-GH3K camera and edited in Adobe Premiere Pro in terms of brightness, contrast, sharpness, and speed. The images were captured using a Sony α 7R III camera and edited in Adobe Photoshop to improve brightness, contrast, and sharpness.

6.1.6. Acknowledgments

We thank Geunyoung Kim for his assistance in the COVID-19 antigen assay optimization. This work was supported by NSERC Alliance Grant and a McGill MI4 grant. D.J. acknowledges support from a Canada Research Chair in Bioengineering.

6.1.7. Supplementary figures

Fig. 62 (= Fig. S1)

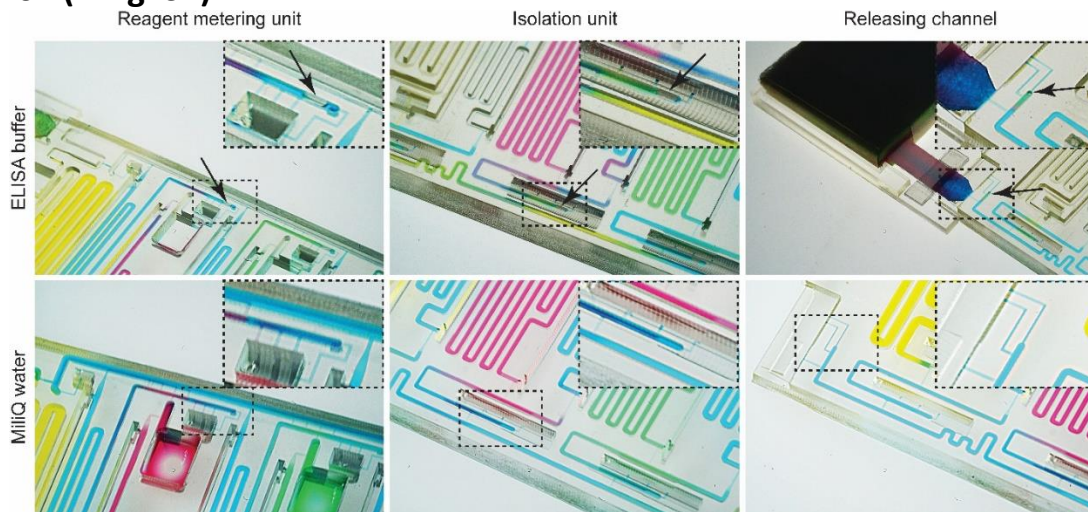


Figure 62 (Fig. S1). **Safety air vents when the circuit is working with ELISA buffer (top panel) and MiliQ water (low panels).** In the case of a low surface tension solution (i.e. ELISA buffer), bubble formation might occur, but the chip fluidic functionality is rendered secure due to the presence of safety air vents. The arrows point to the bubbles formed at the end of the channels. When the circuit is operating with MiliQ water, no bubbles are formed. The solutions were colored with food dye for visualization purposes.

Fig. 63 (Fig. S2)

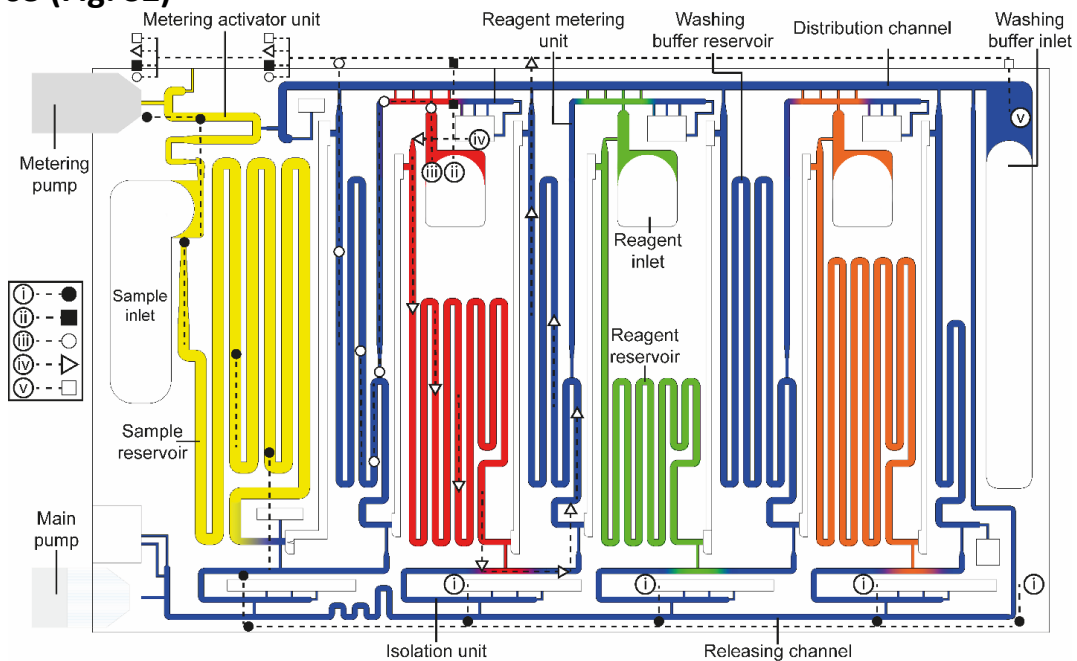


Figure 63 (Fig. S2). **The draining paths to the metering pump during the draining session.** The draining paths ii, iii, and iv exist for green and orange reagents as well but are not shown here for the clarity of the representation.

Fig. 64 (Fig. S3)

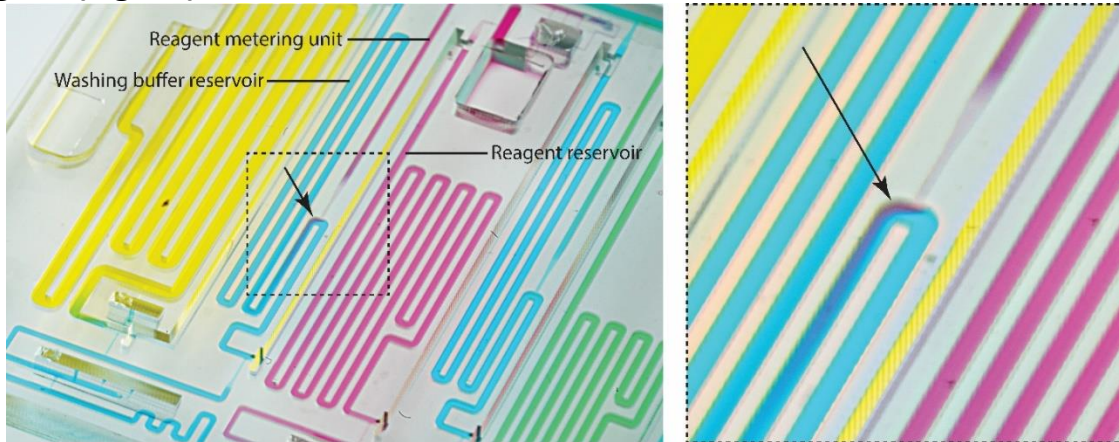


Figure 64 (Fig. S3). **Reagent metering characterization.** The circuit when operating with 140 μL of red reagent (= 70 μL of extra). 70 μL of extra is beyond the ability of the circuit to perform the metering process intactly. As shown in the figure, in this case, a part of the reagent enters the preceding washing buffer serpentine.

7. COMPREHENSIVE SCHOLARLY DISCUSSION OF ALL THE

FINDINGS

ELISA has been extensively utilized to investigate the presence (and, if feasible, quantify the concentration) of an analyte of interest in biological samples¹. capillary-driven microfluidic devices have shown promising potential to automate laboratory enzyme-linked immunosorbent assay (ELISA) as they offer robustness, cost-efficiency, and autonomous operation^{12,98}. Such devices that enable full implementation of ELISA's liquid handling operations under low surface tension solutions, as is the case for ELISA's buffer, while requiring minimal laboratory equipment and user intervention without sacrificing analytical performance have yet to be developed. To this end, herein, we developed an instrument-free, 3D-printed MCR CC for sensitive, quantitative immunoassays.

The fabrication method is among the most important criteria of a microfluidic chip that is intended to be used in resource-limited or point-of-care settings. Ideally, the fabrication method should allow for producing great numbers of chips at a low cost.

Our developed ELISA chip is 3D printed with the printing duration of 30 min, followed by the post-printing preparations mainly including cleaning with isopropanol, curing with ultraviolet radiation, surface treating with oxygen plasma, and sealing the chip via a microfluidic diagnostic tape, with the total duration of ~30 min. Besides, the resin we used was commercially available resin at a very low cost compared to other conventional. Our resin costed only ~ 60 USD per liter which is significantly cheaper than the typical microfluidic resins with the price of ~ 500 USD per liter. The ~1 h duration from the printing procedure to the actual use of the chip together with the cost-effectiveness of the used resin renders our fabrication technique suitable for design iteration purposes, thereby enabling us to print ~1200 chips for this work. Furthermore, in the developed ELISA chip, all capillary elements are implemented on the surface without any embedded features which made the design potentially compatible with injection molding and mass production purposes.

Our developed MCR CC is equipped with aliquoting and metering features to obviate the need for precision micropipettes and therefore allow for the use of transfer pipettes to load the chip. These features would add to the user-friendliness of the device and render it more suitable for resource-limited settings.

Tween20 is one of the essential constituents of ELISA wash buffer. It primarily aids in reducing non-specific binding and assay background¹³. Tween20 is typically used at the concentration of 0.05 in ELISA wash buffer, however, this amount of Tween20 imposes a significant level of

edge flow in a capillary-driven microfluidic chip. The edge flow may consequently lead to bubble formation and chip fluidic failure¹⁷. Owing to this limitation, the capillary-driven microfluidic devices to date either operate with an acceptable concentration of Tween 20 but with limited liquid handling tasks or are able to perform more advanced liquid handling operations but with a limited concentration of Tween 20. Our developed MCR CC allows for the fully-implementation of ELISA's liquid handling task under low-surface tension solutions without any fluidic malfunctions.

As a demonstration of the application, a quantitative, saliva-based COVID-19 antigen assay is presented for the detection of nucleocapsid protein of SARS-CoV-2. The sensor implemented in our developed MCR CC is colorimetric that generates a light-insensitive brown precipitate to obviate the need for signal readout at an accurate time frame, thereby rendering the assay applicable for archival purposes.

The use of saliva could render our device more applicable for, but not limited to, (i) staff-limited and/or resource-limited settings as saliva can be self-collected while reducing the need for personal protective equipment, (ii) patients who have limitations in utilizing NPS (the primary sample specimen for COVID-19 diagnostics) or nasal swabs such as toddlers, babies, and young children^{7,8}. However, one important performance requirement for the saliva-based test is that they need to have high sensitivity to yield reliable results¹⁷. Satisfying this performance requirement, here, our ELISA-on-MCR CC indicates a LOD of 91 pg/mL for 4X-diluted pooled saliva. This level of analytical performance is comparable to that of microplate ELISA and outperforms the commercially lateral flow antigen tests by ~25 times. The small dilution of saliva in conjunction with the high sensitivity of the assay, both enabled

by MCR CC, render the developed ELISA-on-MCR CC a practical and high-performance diagnostic tool outside sophisticated laboratory equipment in resource-limited settings.

The presented work possessed a number of limitations. Even though the device is intended to be used at the resource limited settings, still an oxygen plasma device is needed to for redering the chip hydrophilic. Another limitation is the number of manual steps; the presented ELISA chip comprises 6 manual steps which is a significant improvement to microplate ELISA, but yet requires further improvements for a ready-to-use point of device. In the current study, we used fresh reagents in a solution form and did not explore the longevity of the reagents. In following pargraphs, we suggested future works to overcome the mentioned limitations.

In future works, the device can be tailored for point of care testing. To this end, reconstitution modules need to be designed and implemented on the chip for effective drying and rehydration of the reagents^{98,107}. Sample can be loaded to the chip and one-step loading of washing buffer can then fill washing buffer reservoirs as well as the reconstitution modules for rehydration of reagents. The manual connection of the main pump to the circuit can also be removed by implementing appropriate capillaric elements, such as flow resistance and fuse, on the circuit to reduce the number of manual steps from 6 to 2.

Another point of improvement is to reduce the operational time of the device. The presented MCR CC operates within ~1.5 h which is a significant improvement over laboratory ELISA with a typical assay time of 2-12 h, but still requires further improvement for point of care testing. Implementing dried reagents and reconstitution modules to the MCR CC would reduce the duration of the metering session as there will be no excess volume of the reagents to be

drained by the metering pump. The duration of the sequential delivery session can also be reduced by changing the type of the implemented sensor. In the presented assay platform, the speed of the sequential delivery session is mainly limited to the wicking rate of the nitrocellulose membrane. The assay analytical performance is another factor as a faster flow rate is inversely proportional to the assay sensitivity. Novel sensors such as chemiluminescence⁹⁸ or electrochemical¹⁶⁸ with a faster response time can potentially be implemented (and if possible, fully integrated) into the circuit to reduce assay time without scarifying analytical performance.

Another point of improvement is attributed to reducing the level of post-printing procedures. The developed ELISA chip is 3D-printed with a standardized “STL” file format which allows for sharing of files and designs through online databases. However, several post-printing processes are yet required before the actual use of the chip. Oxygen plasma treatment is one example of such post-printing processes. Even though this method is fast and suitable for rapid prototyping purposes, it is not well-suited for the point-of-care settings. Other surface treatment methods such as plasma-enhanced chemical vapor deposition¹¹ could be potentially used for obtaining longer hydrophilicity.

8. FINAL CONCLUSION AND SUMMARY

In this study, we developed an MCR CC – which we called the ELISA chip – to fully implement the common tasks of laboratory microplate ELISA, e.g. intermediate washing steps, reagents incubation, and removal while preserving assay performance and reducing the total assay operation time. The ELISA chip is equipped with metering and aliquoting features to obviate

the need for precise pipetting and render the chip compatible with disposable pipettes. The sequential delivery is powered by MCR which is a robust method for reliable delivery of the reagents to the reaction chamber. As a demonstration of the application, a sensitive, saliva-based COVID-19 antigen assay was presented which, upon quantification, yielded the LOD of 94 pg/mL for SARS-CoV-2 N protein spiked in 4X-diluted human saliva samples. This level of analytical performance is comparable to that of microplate ELISA and outperforms those of the rapid antigen tests. The presented ELISA chip, therefore, could provide a high-performance diagnostic tool outside sophisticated laboratory equipment in resource-limited settings.

9. REFERENCES

1. Hosseini, S. et al. Advantages, Disadvantages and modifications of conventional ELISA. *SpringerBriefs Appl. Sci. Technol.* 67–115 (2018)
2. Posthuma-Trumpie, G. A., Korf, J. & Van Amerongen, A. Lateral flow (immuno)assay: Its strengths, weaknesses, opportunities and threats. A literature survey. *Anal. Bioanal. Chem.* **393**, 569–582 (2009).
3. Liu, Y. et al. Ultrasensitive and Highly Specific Lateral Flow Assays for Point-of-Care Diagnosis. *ACS Nano* **15**, 3593–3611 (2021).
4. K, S. et al. Comparative analysis of various clinical specimens in detection of SARS-CoV-2 using rRT-PCR in new and follow up cases of COVID-19 infection: Quest for the best choice. *PLoS One* **16**, (2021).
5. Teo, A. K. J. et al. Validation of Saliva and Self-Administered Nasal Swabs for COVID-19 Testing. *medRxiv* 2020.08.13.20173807 (2020) doi:10.1101/2020.08.13.20173807.
6. Teo, A. K. J. et al. Saliva is more sensitive than nasopharyngeal or nasal swabs for diagnosis of asymptomatic and mild COVID-19 infection. *Sci. Reports* 2021 111 **11**, 1–8 (2021).
7. Butler-Laporte, G. et al. Comparison of Saliva and Nasopharyngeal Swab Nucleic Acid Amplification Testing for Detection of SARS-CoV-2: A Systematic Review and Meta-analysis. *JAMA Intern. Med.* **181**, 353–360 (2021).
8. Wyllie, A. L. et al. Saliva or Nasopharyngeal Swab Specimens for Detection of SARS-CoV-2. *N. Engl. J. Med.* **383**, 1283–1286 (2020).

9. Mestdagh, P. et al. Evaluating Diagnostic Accuracy of Saliva Sampling Methods for Severe Acute Respiratory Syndrome Coronavirus 2 Reveals Differential Sensitivity and Association with Viral Load. *J. Mol. Diagn.* 23,1249-1258 (2021).
10. Savela, E. S. et al. Quantitative SARS-CoV-2 Viral-Load Curves in Paired Saliva Samples and Nasal Swabs Inform Appropriate Respiratory Sampling Site and Analytical Test Sensitivity Required for Earliest Viral Detection. *J. Clin. Microbiol.* **60**, e0178521 (2022).
11. Lee, D. & Yang, S. Surface modification of PDMS by atmospheric-pressure plasma-enhanced chemical vapor deposition and analysis of long-lasting surface hydrophilicity. *Sensors Actuators B Chem.* **162**, 425–434 (2012).
12. Yafia, M. et al. Microfluidic Chain Reaction of Structurally Programmed Capillary Flow Events. (2022) doi:10.26434/CHEMRXIV-2021-3W6N8-V3.
13. Steinitz, M. Quantitation of the Blocking Effect of Tween 20 and Bovine Serum Albumin in ELISA Microwells. *Anal. Biochem.* **282**, 232–238 (2000).
14. Whitesides, G. M. The origins and the future of microfluidics. *Nat.* 2006 4427101 **442**, 368–373 (2006).
15. Weigl, B. Towards non- and minimally instrumented, microfluidics-based diagnostic devices. *Lab Chip* **8**, 1999–2014 (2008).
16. Ejikel, J. & van den Berg. Young 4ever--the use of capillarity for passive flow handling in lab on a chip devices. *Lab Chip* **6**, 1405–1408 (2006).
17. Olanrewaju, A., Beaugrand, M., Yafia, M. & Juncker, D. Capillary microfluidics in microchannels: From microfluidic networks to capillary circuits. *Lab on a Chip* vol. 18 2323–2347 (2018).
18. Walker, G. M. & Beebe, D. J. A passive pumping method for microfluidic devices. *Lab Chip* **2**, 131–134 (2002).
19. Berthier, E. & Beebe, D. J. Flow rate analysis of a surface tension driven passive micropump. *Lab Chip* **7**, 1475–1478 (2007).
20. Ejikel, J. & van den Berg. Water in micro- and nanofluidics systems described using the water potential. *Lab Chip* **5**, 1202–1209 (2005).
21. Gallardo, B. S. et al. Electrochemical principles of active control of liquids on submillimeter scales. *Science (80-.)*. **283**, 57–60 (1999).
22. Prins, M. W. J. et al. Fluid control in multichannel structures by electrocapillary pressure. *Science (80-.)*. **291**, 277–280 (2001).
23. He, F. & Nugen, S. R. Automating fluid delivery in a capillary microfluidic device using low-voltage electrowetting valves. *Microfluid. Nanofluidics* 2014 165 **16**, 879–886 (2014).
24. Kazemzadeh, A. et al. The Effect of Contact Angles and Capillary Dimensions on the Burst Frequency of Super Hydrophilic and Hydrophilic Centrifugal Microfluidic Platforms, a CFD Study. *PLoS One* **8**, e73002 (2013).
25. McNeely, M. R., et al. Sample Processing with Hydrophobic Microfluidics. *SLAS Tech.* **4**,

- 30–33 (2016).
26. Cho, H. et al. How the capillary burst microvalve works. *J. Colloid Interface Sci.* **306**, 379–385 (2007).
 27. Choi, J. et al. A Thin, Soft, Skin-Mounted Microfluidic Networks with Capillary Bursting Valves for Chrono-Sampling of Sweat. *Adv. Healthc. Mater.* **6**, 1601355 (2017).
 28. Safavieh, R. & Juncker, D. Capillarics: pre-programmed, self-powered microfluidic circuits built from capillary elements. *Lab Chip* **13**, 4180–4189 (2013).
 29. Liquid transport device, method of transporting a liquid, method of analyzing a liquid and test element for use in analysis of a liquid. (1979).
 30. Capillary stop-flow junction having improved stability against accidental fluid flow. (1991).
 31. Capillary transport device having connected transport zones. (1980).
 32. Capillary transport device having speed and meniscus control means, and method of using. (1985).
 33. Apparatus and method for dilution and mixing of liquid samples. (1987).
 34. Buechler, K. F. Diagnostic Devices and Apparatus for the Controlled Movement of Reagents without membranes. (1993).
 35. Pouletty P. J. & Thomas I. Matrix controlled method of delayed fluid delivery for assays - Dimensions. <https://app.dimensions.ai/details/patent/US-5135872-A>.
 36. Manz, A. et al. Miniaturized total chemical analysis systems: A novel concept for chemical sensing. *Sensors Actuators B Chem.* **1**, 244–248 (1990).
 37. Delamarche, E. et al. Patterned delivery of immunoglobulins to surfaces using microfluidic networks. *Science* (80-.). **276**, 779–781 (1997).
 38. Bernard, A. et al. Micromosaic Immunoassays. *Anal. Chem.* **73**, 8–12 (2000).
 39. Juncker, D. et al. Autonomous Microfluidic Capillary System. *Anal. Chem.* **74**, 6139–6144 (2002).
 40. Novo, P. et al. Integrated optical detection of autonomous capillary microfluidic immunoassays: a hand-held point-of-care prototype. *Biosens. Bioelectron.* **57**, 284–291 (2014).
 41. Wang, J. et al. A self-powered, one-step chip for rapid, quantitative and multiplexed detection of proteins from pinpricks of whole blood. *Lab Chip* **10**, 3157–3162 (2010).
 42. Novo, P. et al. Control of sequential fluid delivery in a fully autonomous capillary microfluidic device. *Lab Chip* **13**, 641–645 (2013).
 43. Gervais, L. & Delamarche, E. Toward one-step point-of-care immunodiagnostics using capillary-driven microfluidics and PDMS substrates. *Lab Chip* **9**, 3330–3337 (2009).
 44. Zimmermann, M. et al. Capillary pumps for autonomous capillary systems. *Lab Chip* **7**, 119–125 (2006).
 45. Hitzbleck, M. et al. Controlled release of reagents in capillary-driven microfluidics using reagent integrators. *Lab Chip* **11**, 2680–2685 (2011).

46. Jun Wang et al. A self-powered, one-step chip for rapid, quantitative and multiplexed detection of proteins from pinpricks of whole blood. *Lab Chip* **10**, 3157–3162 (2010).
47. Jönsson, C. et al. Silane–dextran chemistry on lateral flow polymer chips for immunoassays. *Lab Chip* **8**, 1191–1197 (2008).
48. Mohammed, M. I. & Desmulliez, M P Y. The manufacturing of packaged capillary action microfluidic systems by means of CO₂ laser processing. doi:10.1007/s00542-013-1792-1.
49. Olanrewaju, O. et al. Autonomous microfluidic capillary circuits replicated from 3D-printed molds. *Lab Chip* **16**, 3804–3814 (2016).
50. Mohammed, M. I. & Desmulliez, M. P. Y. Characterization and theoretical analysis of rapidly prototyped capillary action autonomous microfluidic systems. *J. Microelectromechanical Syst.* **23**, 1408–1416 (2014).
51. Olanrewaju, A. O. et al. Microfluidic Capillary Circuit for Rapid and Facile Bacteria Detection. *Anal. Chem.* **89**, 6846–6853 (2017).
52. Wu, W. & Manz, A. Rapid manufacture of modifiable 2.5-dimensional (2.5D) microstructures for capillary force-driven fluidic velocity control. *RSC Adv.* **5**, 70737–70742 (2015).
53. Mohammed, M. I. & Desmulliez, M. P. Y. The manufacturing of packaged capillary action microfluidic systems by means of CO₂ laser processing. *Microsyst. Technol.* **19**, 809–818 (2013).
54. Beauchamp, M. J. Moving from millifluidic to truly microfluidic sub-100- μ m cross-section 3D printed devices. *Anal. Bioanal. Chem.* **409**, 4311–4319 (2017).
55. Wang, J. B. et al. Research on the Prediction of Static Contact Angle in Circular Capillary Tubes. *Appl. Mech. Mater.* **161**, 21–25 (2012).
56. Spika, F. X. An essay on retention. *Int. J. Orthod.* **25**, 15–16 (1987).
57. Zimmermann, M. et al. Valves for autonomous capillary systems. doi:10.1007/s10404-007-0256-2.
58. Concus, P. & Finn, R. On the Behavior of a Capillary Surface in a Wedge. *Proc. Natl. Acad. Sci. U. S. A.* **63**, 292 (1969).
59. Bruus, H. *Theoretical microfluidics*. Oxford Univ. Press. ISBN: 978-0-19-923509-4 (2008).
60. Xia, Y. & Whitesides, G. M. Soft Lithography. *Ann. Rev. of Mater. Sci.* **28**, 153–184 (2003).
61. Carlborg, F. C. et al. Beyond PDMS: off-stoichiometry thiol–ene (OSTE) based soft lithography for rapid prototyping of microfluidic devices. *Lab Chip* **11**, 3136–3147 (2011).
62. Ziegler, J et al. High-Performance Immunoassays Based on Through-Stencil Patterned Antibodies and Capillary Systems. *Anal. Chem.* **80**, 1763–1769 (2008).
63. Bodas, D. & Khan-Malek, C. Hydrophilization and hydrophobic recovery of PDMS by oxygen plasma and chemical treatment—An SEM investigation. *Sensors Actuators B Chem.* **123**, 368–373 (2007).
64. Clark, T. J. et al. The Triage Cardiac Panel: Cardiac Markers for the Triage System. *Point*

- Care J. *N-Pat. Test. & Tech.* **1**:42-46 (2002)
65. Wolf, M. et al. Simultaneous detection of C-reactive protein and other cardiac markers in human plasma using micromosaic immunoassays and self-regulating microfluidic networks. *Biosens. Bioelectron.* **19**, 1193–1202 (2004).
 66. Lillehoj, B. et al. A self-pumping lab-on-a-chip for rapid detection of botulinum toxin. *Lab Chip* **10**, 2265–2270 (2010).
 67. Berthier, J. et al. Capillary Flow Resistors: Local and Global Resistors. *Langmuir* **32**, 915–921 (2016).
 68. Gervais, L. et al. Capillary-driven multiparametric microfluidic chips for one-step immunoassays. *Biosens. Bioelectron.* **27**, 64–70 (2011).
 69. Pla-Roca, M. & Juncker. PDMS microfluidic capillary systems for patterning proteins on surfaces and performing miniaturized immunoassays. *Methods Mol. Biol.* **671**, 177–194 (2011).
 70. Safavieh, R. et al. Serpentine and leading-edge capillary pumps for microfluidic capillary systems. *Microfluid. Nanofluidics* 2014 **18**, 357–366 (2014).
 71. Goedecke, N. et al. Evaporation driven pumping for chromatography application. *Lab Chip* **2**, 219–223 (2002).
 72. Wang, X. et al. Paper pump for passive and programmable transport. *Biomicrofluidics* **7**, (2013).
 73. Hansson, J. et al. Synthetic microfluidic paper: high surface area and high porosity polymer micropillar arrays. *Lab Chip* **16**, 298–304 (2016).
 74. Bae, Y. et al. Hydrogel-based capillary flow pumping in a hydrophobic microfluidic channel. *Jpn. J. Appl. Phys.* **53**, 067201 (2014).
 75. Lee, Y. C. & Hsieh, W. H. Absorbent-force-driven microflow cytometer. *Sensors Actuators B Chem.* **202**, 1078–1087 (2014).
 76. Zhao, B. et al. Surface-directed liquid flow inside microchannels. *Science (80-.)*. **291**, 1023–1026 (2001).
 77. Juncker, D. et al. Soft and rigid two-level microfluidic networks for patterning surfaces. *J. Micromechanics Microengineering* **11**, 532 (2001).
 78. Zimmermann, M. et al. Valves for autonomous capillary systems. *Microfluid. Nanofluidics* 2007 **5**, 395–402 (2008).
 79. Paul Vulto et al. Phaseguides: a paradigm shift in microfluidic priming and emptying. *Lab Chip* **11**, 1596–1602 (2011).
 80. Man, P. F. et al. Microfabricated capillarity-driven stop valve and sample injector. *Proc. IEEE Micro Electro Mech. Syst.* 45–50 (1998) doi:10.1109/MEMSYS.1998.659727.
 81. Glière, A. & Delattre, C. Modeling and fabrication of capillary stop valves for planar microfluidic systems. *Sensors Actuators A Phys.* **130–131**, 601–608 (2006).
 82. Papadimitriou, V. A. et al. 3D capillary stop valves for versatile patterning inside

- microfluidic chips. *Anal. Chim. Acta* **1000**, 232–238 (2018).
83. Melin, J. et al. A liquid-triggered liquid microvalve for on-chip flow control. *Sensors Actuators B Chem.* **100**, 463–468 (2004).
 84. Li, L. et al. Autonomous capillary microfluidic devices with constant flow rate and temperature-controlled valving. *Soft Matter* **17**, 7781–7791 (2021).
 85. Hitzbleck, M. & Delamarche, E. Advanced Capillary Soft Valves for Flow Control in Self-Driven Microfluidics. *Micromachines* 2013, Vol. 4, Pages 1-8 **4**, 1–8 (2013).
 86. Hitzbleck, M. et al. Capillary soft valves for microfluidics. *Lab Chip* **12**, 1972–1978 (2012).
 87. Cesaro-Tadic, S et al. High-sensitivity miniaturized immunoassays for tumor necrosis factor alpha using microfluidic systems. *Lab Chip* **4**, 563–569 (2004).
 88. Wolf, M. et al. Simultaneous detection of C-reactive protein and other cardiac markers in human plasma using micromosaic immunoassays and self-regulating microfluidic networks. *Biosens. Bioelectron.* **19**, 1193–1202 (2004).
 89. Lutz, B. et al. Dissolvable fluidic time delays for programming multi-step assays in instrument-free paper diagnostics. *Lab Chip* **13**, 2840–2847 (2013).
 90. Lenk, G. et al. Delay valving in capillary driven devices based on dissolvable thin films. *μTas2014* (2014).
 91. Meffan, C. et al. Transistor off-Valve Based Feedback, Metering and Logic Operations in Capillary Microfluidics. *Proc. IEEE Int. Conf. Micro Electro Mech. Syst.* **2021-January**, 218–221 (2021).
 92. Pla-Roca, M. & Juncker, D. PDMS Microfluidic Capillary Systems for Patterning Proteins on Surfaces and Performing Miniaturized Immunoassays. *Methods Mol. Biol.* **671**, 177–194 (2011).
 93. Cesaro-Tadic, S. et al. High-sensitivity miniaturized immunoassays for tumor necrosis factor α using microfluidic systems. *Lab Chip* **4**, 563–569 (2004).
 94. Buechler, K. F. et al. Microarray Immunoassays in the Microfluidic Triage[®] Protein Chip. *Micro Total Anal. Syst.* 2001 42–44 (2001) doi:10.1007/978-94-010-1015-3_15.
 95. Gervais, L. & Delamarche, E. Toward one-step point-of-care immunodiagnostics using capillary-driven microfluidics and PDMS substrates. *Lab Chip* **9**, 3330–3337 (2009).
 96. Fu, E. et al. Enhanced sensitivity of lateral flow tests using a two-dimensional paper network format. *Anal. Chem.* **83**, 7941–7946 (2011).
 97. Chin, C. D. et al. Microfluidics-based diagnostics of infectious diseases in the developing world. *Nat. Med.* **17**, 1015–1019 (2011).
 98. Ghosh, S. et al. A new microchannel capillary flow assay (MCFA) platform with lyophilized chemiluminescence reagents for a smartphone-based POCT detecting malaria. *Microsystems Nanoeng.* 2020 61 **6**, 1–18 (2020).
 99. Vinitha, T. U. et al. A new polymer lab-on-a-chip (LOC) based on a microfluidic capillary flow assay (MCFA) for detecting unbound cortisol in saliva. *Lab Chip* **20**, 1961–1974 (2020).

100. Dogan, Ü. et al. Multiplex enumeration of *Escherichia coli* and *Salmonella enteritidis* in a passive capillary microfluidic chip. *Anal. Methods* **12**, 3788–3796 (2020).
101. Ahi, E. E. et al. A capillary driven microfluidic chip for SERS based hCG detection. *Biosens. Bioelectron.* **195**, (2022).
102. Rocca, M. et al. Rapid quantitative assays for glucose-6-phosphate dehydrogenase (G6PD) and hemoglobin combined on a capillary-driven microfluidic chip. *Lab Chip* **21**, 3573–3582 (2021).
103. Ramalingam, N. et al. Real-time PCR array chip with capillary-driven sample loading and reactor sealing for point-of-care applications. *Biomed. Microdevices* **11**, 1007–1020 (2009).
104. Tachibana, H. et al. Self-propelled continuous-flow PCR in capillary-driven microfluidic device: Microfluidic behavior and DNA amplification. *Sensors Actuators B Chem.* **206**, 303–310 (2015).
106. Tachibana, H. et al. On-chip quantitative detection of pathogen genes by autonomous microfluidic PCR platform. *Biosens. Bioelectron.* **74**, 725–730 (2015).
107. Ramalingam, N. et al. Numerical and experimental study of capillary-driven flow of PCR solution in hybrid hydrophobic microfluidic networks. *Biomed. Microdevices* **18**, (2016).
108. Gökçe, O. et al. Self-coalescing flows in microfluidics for pulse-shaped delivery of reagents. *Nat.* 2019 5747777 **574**, 228–232 (2019).
109. Brown, M. T. & Bussell, J. K. Medication Adherence: WHO Cares? *Mayo Clin. Proc.* **86**, 304 (2011).
110. Chaudri, N. A. Adherence to Long-term Therapies Evidence for Action. *Ann. Saudi Med.* **24**, 221 (2004).
111. Delamarche, E. et al. Capillary Microfluidics for Monitoring Medication Adherence. *Angew. Chemie Int. Ed.* **60**, 17784–17796 (2021).
112. Staal, S. et al. A versatile electrophoresis-based self-test platform. *Electrophoresis* **36**, 712–721 (2015).
113. Haghayegh, F. et al. A. Immuno-biosensor on a chip: a self-powered microfluidic-based electrochemical biosensing platform for point-of-care quantification of proteins. *Lab Chip* **22**, 108–120 (2021).
114. Arango, Y. et al. Electro-actuated valves and self-vented channels enable programmable flow control and monitoring in capillary-driven microfluidics. *Sci. Adv.* **6**, (2020).
115. artinez-Lopez, J et al. Xurography as a Rapid Fabrication Alternative for Point-of-Care Devices: Assessment of Passive Micromixers. *Sensors (Basel).* **16**, (2016).
116. Mohammed, M. I. & Desmulliez, M. P. Y. Characterization and theoretical analysis of rapidly prototyped capillary action autonomous microfluidic systems. *J. Microelectromechanical Syst.* **23**, 1408–1416 (2014).
117. Mohammed, M. I. et al. Rapid laser prototyping of valves for microfluidic autonomous

- systems. *J. Micromechanics Microengineering* **23**, (2013).
118. Gattass, R. R. & Mazur, E. Femtosecond laser micromachining in transparent materials. *Nat. Photonics* 2008 24 **2**, 219–225 (2008).
 119. Nielsen, A. V., Beauchamp, M. J., Nordin, G. P. & Woolley, A. T. 3D Printed Microfluidics. *Annu. Rev. Anal. Chem.* **13**, 45–65 (2020).
 120. Waheed, S. et al. 3D printed microfluidic devices: enablers and barriers. *Lab Chip* **16**, 1993–2013 (2016).
 121. Gross, B. et al. Recent Advances in Analytical Chemistry by 3D Printing. *Anal. Chem.* **89**, 57–70 (2016).
 122. Robert K. L. et al. Dynamics of Capillary-Driven Flow in 3D Printed Open Microchannels. *Langmuir* **33**, 2949–2964 (2017).
 123. Macdonald, N. P. et al. Comparing Microfluidic Performance of Three-Dimensional (3D) Printing Platforms. *Anal. Chem.* **89**, 3858–3866 (2017).
 124. Lee, D. & Lee, J. Testing on the move: South Korea’s rapid response to the COVID-19 pandemic. *Transp. Res. Interdiscip. Perspect.* **5**, 100111 (2020).
 125. Lee, D. & Lee, J. Testing on the move: South Korea’s rapid response to the COVID-19 pandemic. *Transp. Res. Interdiscip. Perspect.* **5**, 100111 (2020).
 126. Stephanie, B. et al. Geographic Differences in COVID-19 Cases, Deaths, and Incidence - United States, February 12-April 7, 2020. *MMWR. Morb. Mortal. Wkly. Rep.* **69**, 465–471 (2020).
 127. Emergency Use Authorization | FDA. <https://www.fda.gov/emergency-preparedness-and-response/mcm-legal-regulatory-and-policy-framework/emergency-use-authorization#covidinvitrodev>.
 128. Maxmen, A. The researchers taking a gamble with antibody tests for coronavirus. *Nature* (2020) doi:10.1038/D41586-020-01163-5.
 129. Mittal, A. et al. COVID-19 pandemic: Insights into structure, function, and hACE2 receptor recognition by SARS-CoV-2. *PLOS Pathog.* **16**, e1008762 (2020).
 130. Kilic, T. et al. Molecular and Immunological Diagnostic Tests of COVID-19: Current Status and Challenges. *iScience* **23**, 101406 (2020).
 131. Ke, Z. et al. Structures and distributions of SARS-CoV-2 spike proteins on intact virions. *Nat.* 2020 5887838 **588**, 498–502 (2020).
 132. Suo, T. et al. ddPCR: a more accurate tool for SARS-CoV-2 detection in low viral load specimens. <https://doi.org/10.1080/22221751.2020.1772678> **9**, 1259–1268 (2020).
 133. Tahamtan, A. & Ardebili, A. Real-time RT-PCR in COVID-19 detection: issues affecting the results. *Expert. Rev. Mol. Diagn.* **20**, 453–454 (2020).
 134. Han, H. et al. SARS-CoV-2 RNA more readily detected in induced sputum than in throat swabs of convalescent COVID-19 patients. *Lancet Infect. Dis.* **20**, 655–656 (2020).
 135. Xie, X. et al. Chest CT for Typical Coronavirus Disease 2019 (COVID-19) Pneumonia:

- Relationship to Negative RT-PCR Testing. <https://doi.org/10.1148/radiol.2020200343> **296**, E41–E45 (2020).
136. Ai, T. et al. Correlation of Chest CT and RT-PCR Testing for Coronavirus Disease 2019 (COVID-19) in China: A Report of 1014 Cases. *Eur. J. Med. Sci.* **296**, E32–E40 (2020).
 137. Gibani, M. M. et al. Assessing a novel, lab-free, point-of-care test for SARS-CoV-2 (CovidNudge): a diagnostic accuracy study. *The Lancet Microbe* **1**, e300–e307 (2020).
 138. Baker, M. Digital PCR hits its stride. *Nat. Methods* 2012 96 **9**, 541–544 (2012).
 139. Hindson, C. M. et al. Absolute quantification by droplet digital PCR versus analog real-time PCR. *Nat. Methods* 2013 1010 **10**, 1003–1005 (2013).
 140. Foo, P. C. et al. Loop-mediated isothermal amplification (LAMP) reaction as viable PCR substitute for diagnostic applications: a comparative analysis study of LAMP, conventional PCR, nested PCR (nPCR) and real-time PCR (qPCR) based on *Entamoeba histolytica* DNA derived from faecal sample. *BMC Biotechnol.* 2020 201 **20**, 1–15 (2020).
 141. Yan, C. et al. Rapid and visual detection of 2019 novel coronavirus (SARS-CoV-2) by a reverse transcription loop-mediated isothermal amplification assay. *Clin. Microbiol. Infect.* **26**, 773–779 (2020).
 142. Notomi, T. et al. Loop-mediated isothermal amplification (LAMP): principle, features, and future prospects. *J. Microbiol.* 2015 531 **53**, 1–5 (2015).
 143. Notomi, T. et al. Loop-mediated isothermal amplification of DNA. *Nucleic Acids Res.* **28**, e63 (2000).
 144. Baek, Y. H. et al. Development of a reverse transcription-loop-mediated isothermal amplification as a rapid early-detection method for novel SARS-CoV-2. *Emerg Microbes Infect.* **9**, 998–1007 (2020).
 145. Wang, L. et al. Technical aspects of nicking enzyme assisted amplification. *Analyst* **143**, 1444–1453 (2018).
 146. Ménová, P. et al. Scope and Limitations of the Nicking Enzyme Amplification Reaction for the Synthesis of Base-Modified Oligonucleotides and Primers for PCR. *Bioconjug. Chem.* **24**, 1081–1093 (2013).
 147. Li, J et al. Review: a comprehensive summary of a decade development of the recombinase polymerase amplification. *Analyst* **144**, 31–67 (2018).
 148. Xia, S. & Chen, X. Single-copy sensitive, field-deployable, and simultaneous dual-gene detection of SARS-CoV-2 RNA via modified RT-RPA. *Cell Discov.* **6**, (2020).
 149. Gootenberg, J. S. et al. Nucleic acid detection with CRISPR-Cas13a/C2c2. *Science* **356**, 438–442 (2017).
 150. Kaminski, M. M. et al. CRISPR-based diagnostics. *Nat. Biomed. Eng.* 2021 57 **5**, 643–656 (2021).
 151. Broughton, J. P. et al. CRISPR-Cas12-based detection of SARS-CoV-2. *Nat. Biotechnol.* 2020 387 **38**, 870–874 (2020).

152. Joung, J. et al. Point-of-care testing for COVID-19 using SHERLOCK diagnostics. medRxiv (2020) doi:10.1101/2020.05.04.20091231.
153. Squires, T. M. et al. Making it stick: convection, reaction and diffusion in surface-based biosensors. *Nat. Biotechnol.* 2008 264 **26**, 417–426 (2008).
154. R, W., H, L., J, K. & MJ, P. COVID-19 diagnostics in context. *Sci. Transl. Med.* **12**, (2020).
155. N, Y. et al. Challenges in Laboratory Diagnosis of the Novel Coronavirus SARS-CoV-2. *Viruses* **12**, (2020).
156. Sandwich ELISA Principles, Formats, and Optimization. <https://www.genscript.com/ELISA-Principles-Formats-and-Optimization.html>.
157. Wild, D. & Kodak, E. *The Immunoassay Handbook*. The Immunoassay Handbook (Elsevier Ltd, 2013). doi:10.1016/C2010-0-66244-4.
158. Types of ELISA - Labster Theory. <https://theory.labster.com/types-elisa/>.
159. ELISA Technical Guide and Protocol by ThermoFisher Scientific. (Tech Tip #65). <http://tools.thermofisher.com/content/sfs/brochures/TR0065-ELISA-guide.pdf>
160. Nitrocellulose membrane selection | Cytiva. <https://www.cytivalifesciences.com/en/us/solutions/lab-filtration/knowledge-center/membrane-selection>.
160. ELISA Development and Optimization | Thermo Fisher Scientific - CA. <https://www.thermofisher.com/ca/en/home/life-science/protein-biology/protein-biology-learning-center/protein-biology-resource-library/pierce-protein-methods/overview-elisa/elisa-development-optimization.html>.
161. Blog - Curve Fitting for Immunoassays: ELISA and Multiplex Bead Based Assays (LEGENDplex™). <https://www.biolegend.com/en-us/blog/curve-fitting-for-immunoassays-legendplex>.
162. Armbruster, D. A. & Pry, T. Limit of Blank, Limit of Detection and Limit of Quantitation. *Clin. Biochem. Rev.* **29**, S49 (2008).
163. Four Parameter Logistic Curve Report Contents - MyAssays. <https://www.myassays.com/four-parameter-logistic-curve-report-contents.html>.
164. Wu, L. P. et al. Duration of Antibody Responses after Severe Acute Respiratory Syndrome. *Emerg. Infect. Dis.* **13**, 1562 (2007).
165. Liu, L. et al. A preliminary study on serological assay for severe acute respiratory syndrome coronavirus 2 (SARS-CoV-2) in 238 admitted hospital patients. *Microbes Infect.* **22**, 206–211 (2020).
166. Meyer, B. et al. Serological assays for emerging coronaviruses: challenges and pitfalls. *Virus Res.* **194**, 175–183 (2014).
167. Okba, N. M. A. et al. Severe Acute Respiratory Syndrome Coronavirus 2-Specific Antibody Responses in Coronavirus Disease Patients. *Emerg. Infect. Dis.* **26**, 1478–1488 (2020).
168. Ali, M. A. et al. Sensing of COVID-19 Antibodies in Seconds via Aerosol Jet Nanoprinted

- Reduced-Graphene-Oxide-Coated 3D Electrodes. *Adv. Mater.* **33**, 2006647 (2021).
169. Establishment and validation of a pseudovirus neutralization assay for SARS-CoV-2. *Emerg. Microbes & Infect.* **9**, 680–686 (2020).
 170. Petherick, A. Developing antibody tests for SARS-CoV-2. *Lancet* **395**, 1101–1102 (2020).
 171. Tan, C. W. et al. A SARS-CoV-2 surrogate virus neutralization test based on antibody-mediated blockage of ACE2–spike protein–protein interaction. *Nat. Biotechnol.* 2020 389 **38**, 1073–1078 (2020).
 172. Zhang, N. et al. A lateral flow test detecting SARS-CoV-2 neutralizing antibodies. *medRxiv* 2020.11.05.20222596 (2020) doi:10.1101/2020.11.05.20222596.
 173. Thudium, R. F. et al. Early laboratory diagnosis of COVID-19 by antigen detection in blood samples of the SARS-CoV-2 nucleocapsid protein. *J. Clin. Microbiol.* **59**, (2021).
 174. Peeling, R. W. et al. Scaling up COVID-19 rapid antigen tests: promises and challenges. *Lancet Infect. Dis.* **21**, e290–e295 (2021).
 175. Corman, V. M. et al. Comparison of seven commercial SARS-CoV-2 rapid point-of-care antigen tests: a single-centre laboratory evaluation study. *The Lancet Microbe* **2**, e311–e319 (2021).
 176. Cate, D. M. et al. Antibody Screening Results for Anti-Nucleocapsid Antibodies Toward the Development of a Lateral Flow Assay to Detect SARS-CoV-2 Nucleocapsid Protein. *ACS Omega* *acsomega.1c01253* (2021) doi:10.1021/ACSOMEGA.1C01253.
 177. Grant, B. D. et al. A SARS-CoV-2 Coronavirus Nucleocapsid Protein Antigen-Detecting Lateral Flow Assay. (2020) doi:10.26434/CHEMRXIV.12794825.V1.
 178. Seo, G. et al. Rapid Detection of COVID-19 Causative Virus (SARS-CoV-2) in Human Nasopharyngeal Swab Specimens Using Field-Effect Transistor-Based Biosensor. *ACS Nano* **14**, 5135–5142 (2020).
 179. Grant, B. D. et al. SARS-CoV-2 Coronavirus Nucleocapsid Antigen-Detecting Half-Strip Lateral Flow Assay Toward the Development of Point of Care Tests Using Commercially Available Reagents. *Anal. Chem.* **92**, 11305–11309 (2020).
 180. Wang, D. et al. Rapid lateral flow immunoassay for the fluorescence detection of SARS-CoV-2 RNA. *Nat. Biomed. Eng.* 2020 412 **4**, 1150–1158 (2020).
 181. Savelle, E. S. et al. Quantitative SARS-CoV-2 viral-load curves in paired saliva and nasal swabs inform appropriate respiratory sampling site and analytical test sensitivity required for earliest viral detection. *medRxiv* 2021.04.02.21254771 (2021) doi:10.1101/2021.04.02.21254771.
 182. Case, J. B., Bailey, A. L., Kim, A. S., Chen, R. E. & Diamond, M. S. Growth, detection, quantification, and inactivation of SARS-CoV-2. *Virology* **548**, 39–48 (2020).
 183. Costantini, F. et al. Lab-on-chip system combining a microfluidic-ELISA with an array of amorphous silicon photosensors for the detection of celiac disease epitopes. *Sens. Bio-Sensing Res.* **6**, 51–58 (2015).

184. Uddin, M. J. et al. Fully integrated rapid microfluidic device translated from conventional 96-well ELISA kit. *Sci. Reports* 2021 111 **11**, 1–9 (2021).
185. Ng, A. H. C. et al. A digital microfluidic system for serological immunoassays in remote settings. *Sci. Transl. Med.* **10**, (2018).
186. Lai, S. et al. Design of a Compact Disk-like Microfluidic Platform for Enzyme-Linked Immunosorbent Assay. *Anal. Chem.* **76**, 1832–1837 (2004).
187. Reis, N. M. et al. Gravity-Driven Microfluidic Siphons: Fluidic Characterization and Application to Quantitative Immunoassays. *ACS Sensors* **6**, 4338–4348 (2021).
188. Panraksa, Y. et al. Simple manipulation of enzyme-linked immunosorbent assay (ELISA) using an automated microfluidic interface. *Anal. Methods* **14**, 1774-1781 (2022).
189. Gong, M. M. & Sinton, D. Turning the Page: Advancing Paper-Based Microfluidics for Broad Diagnostic Application. *Chem. Rev.* **117**, 8447–8480 (2017).
190. Toley, B. J. et al. A versatile valving toolkit for automating fluidic operations in paper microfluidic devices. *Lab Chip* **15**, 1432–1444 (2015).
191. De Lean, A. et al. Simultaneous analysis of families of sigmoidal curves: application to bioassay, radioligand assay, and physiological dose-response curves. *Am. J. Physiol.* **4**, (1978).